Miniaturization of Microwave Radiometers for Internal Body Thermometry

by

Jooeun Lee

B.S., Pusan National University, 2019

M.S., Korea Advanced Institute of Science and Technology, 2021

A thesis submitted to the

Faculty of the Graduate School of the

University of Colorado in partial fulfillment

of the requirements for the degree of

Doctor of Philosophy

Department of Electrical and Computer Engineering

2025

Committee Members:

Zoya Popović, Chair

Dejan Filipović

Taylor Barton

Rob Scheeler

Gabriel Santamaria Botello

Lee, Jooeun (Ph.D., Electrical Engineering)

Miniaturization of Microwave Radiometers for Internal Body Thermometry

Thesis directed by Prof. Zoya Popović

This thesis presents the development and characterization of microwave radiometer sensors for non-invasive internal body temperature measurement, addressing a need for accurate, real-time, and non-invasive thermometry. The work spans the design, implementation, and validation of advanced radiometer architectures and near-field antennas, integrating them into compact sensors capable of deep tissue temperature sensing.

The theoretical foundations of radiometry are presented, highlighting key parameters such as sensitivity and calibration methods. Various radiometer architectures, including Dicke, correlation, and hybrid correlation-Dicke designs, are analyzed. This is followed by the design and characterization of GaAs MMIC radiometer front-ends, including low-noise amplifiers (LNAs), switches, and hybrid couplers. These MMICs achieve low noise figures and power efficiency, enabling high sensitivity in compact form factors.

Near-field antennas are developed to optimize power absorption from targeted tissue layers, including single and dual-feed architectures. Electromagnetic simulations validate their performance in layered dielectric environments, ensuring effective thermal power retrieval from human tissues. Two-layer tissue phantoms are used to experimentally validate the system, providing controlled testing environments with known temperature distributions. The results demonstrate the radiometer ability to resolve internal temperature variations with average errors as low as 0.1 °C.

In-vivo measurements are conducted using human cheek tissue, demonstrating the sensor capability to monitor the temperature of liquid held in the mouth. Repeatability and sensitivity analyses confirm the robustness of the system under realistic application conditions, accounting for variations in tissue properties and environmental factors.

This thesis establishes a framework for non-invasive internal body thermometry using mi-

crowave radiometers. The combination of MMIC technology, advanced antenna design, and experimental validation forms a foundation for future integration into wearable medical devices, offering significant potential for applications in continuous health monitoring and diagnostics.

Dedication

To my family.

Acknowledgements

First, I would like to thank my family for their love and encouragement throughout my graduate studies, especially my parents, who supported my decision to go overseas and helped me pursue my dreams.

Thank you to all the current and former students in the RF group for their collaborative spirit and insightful discussions.

Finally, I would like to thank my advisor, Prof. Zoya Popovic, for her guidance, encouragement, and the countless hours she invested in helping my research. Her mentorship extended beyond academics, shaping me into a better researcher and individual. Also, I would like to thank my committee members for their constructive feedback and the time they dedicated to supporting my work.

Contents

Chapter

1 Introduction **1**

1.1 Motivation 1

1.2 Existing Methods 3

1.3 Microwave Thermometry 4

1.4 Previous Research 9

1.5 Radiometer Miniaturization 11

1.6 Thesis Goal and Outline 12

2 Nearfield Antenna **14**

2.1 Introduction 14

2.2 Weighting Factor Analysis 15

2.3 Rectangular Patch Antenna 18

2.4 Slotted Circular Antenna 21

2.5 Two-feed Antenna 23

2.6 Conclusion 29

3 MMIC Dicke Radiometer Design **30**

3.1 Radiometer Theory 30

3.2 SPDT Switch Design 34

3.3 LNA Design 37

3.4 Radiometer Measurements . . . 41
3.5 InGaAs Dicke Radiometer . . . 47
3.6 Conclusion . . . 49

4 Hybrid Correlation-Dicke Radiometer **51**
4.1 Hybrid Radiometer Architecture . . . 51
4.2 PCB Design . . . 53
4.3 MMIC Design . . . 58
4.3.1 Lumped-Element Hybrid Coupler . . . 60
4.3.2 LNA and SPDT Switch . . . 62
4.3.3 Radiometer Implementation . . . 63
4.4 Conclusion . . . 66

5 Phantom Temperature Measurements **67**
5.1 Tissue Phantom Background . . . 67
5.2 Two-layer Phantom Temperature Measurements with GaAs Dicke MMIC . . . 68
5.3 Two-layer Phantom Temperature Measurements with Hybrid Radiometer MMIC . . . 75
5.4 Two-layer Phantom Temperature Measurements with InGaAs MMIC Dicke . . . 78
5.5 Conclusion . . . 80

6 In-vivo Measurements **81**
6.1 *In-vivo* measurement with Dicke MMIC . . . 82
6.2 *In-vivo* measurement with Hybrid Radiometer PCB . . . 85
6.3 *In-vivo* measurement with Hybrid Radiometer MMIC . . . 88
6.4 Repeatability . . . 90
6.5 Sensitivity Study . . . 92
6.6 Conclusion . . . 94

7 Conclusion and Future Work **96**

7.1 Summary and Contributions 96

7.2 Future Work 97

7.2.1 Antenna with Spatial Pattern Diversity 97

7.2.2 Heterodyne Receivers 98

7.2.3 Phantom Manufacture and Characterization 99

7.2.4 Miniaturization of Hardware 100

7.2.5 Interference Mitigation 100

7.2.6 Neural Network for Tissue layer Characterization 101

Bibliography **103**

Tables

Table

1.1 Microwave radiometers for internal body thermometry 11

2.1 Previous works on near-field antenna for microwave thermometry 15

2.2 Phantom and tissue electromagnetic properties at 1.4 GHz. [1] 18

3.1 Comparison of radiometer architectures 32

3.2 Performance Comparison of GaAs L-band LNAs 41

4.1 Components in the designed radiometer. 54

6.1 Weighting factors of tissue layers with skin property variation 93

Figures

Figure

1.1 Accurately assessing internal body temperature has significant implications for various medical applications, including: (a) Measurement of brain temperature during cardiac surgery to about 15°C [2], (b) precise temperature measurement of the tumor tissue during hyperthermia treatment [3], and (c) tracking core body temperature for monitoring sleep disorder [4]. 2

1.2 Illustration of the relationship between core temperature, likelihood of sleep, and melatonin. The figure is provided by [4]. 3

1.3 Existing methods for internal body thermometry. (a) Thermometer pills, (b) MRI, and (c) heat-flux device. 4

1.4 Illustration of non-invasive internal body thermometry using a microwave radiometer placed below the sternum [5]. A near-field antenna is placed on the skin to detect thermal power from a stack of tissue layers. This signal is transferred to a low-noise receiver, depicted as a Dicke radiometer in this example, and processed through a temperature estimation algorithm. A thermocouple on the skin provides additional data to enhance the accuracy of the temperature estimation algorithm. 5

1.5 Black-body intensity curve of spectral radiance. Curves are shown for the temperature of the Cosmic Background Radiation (CMB), a healthy human, and the sun. 7

1.6 An antenna transmitting and receiving in a closed system in thermal equilibrium. . 8

1.7 Previous works on microwave radiometers for internal body temperature measurement. (a) Multi-frequency Dicke radiometer at at 1.5, 2.5, and 3.5 GHz [6]. (b) Dicke radiometer at 3.4–4.2,GHz with a circulator at the input [7]. (c) Dual-band Dicke radiometer operating at 1.35 and 2.75 GHz implemented on CMOS [8]. 9

1.8 Previous works on microwave radiometers for internal body temperature measurement from University of Colorado Boulder. (a) Dicke radiometer (b) modular correlation radiometer. 10

1.9 Illustration of a few different radiometers describe for this work. From left to right, the form factor of the radiometer is reduced for wearability. A radiometer MMIC is placed on top of a penny. 11

2.1 A near-field probe positioned on the stack of 4-layer tissue stack. Thermal power is received by the antenna and transferred to a radiometer to detect T_{total}, which is the weighted sum of the temperatures in different layers. 16

2.2 Cross-section of the near-field antenna designed for thermal power retrieval, featuring a high sensing coefficient from the muscle phantom layer (left), along with top view of the near-field antenna with detailed parameters (right). 18

2.3 Simulated and measured reflection coefficient magnitude when the near-field antenna is placed onto the phantom tissue stack. The measured reflection coefficient is also shown for the antenna in free-space for comparison. 20

2.4 Full-wave simulations of volume Joule loss density (W/m^3) of the near-field antenna on a skin-muscle phantom with 1 W at the feed. The weighting factors (percentages of total power) are also stated, with 3% of the total power radiation into free space outside the tissue and unaccounted for here. 20

2.5 Top view and cross-section of the near-field antenna designed for thermal power retrieval. The sides of the antenna are covered by metal shielding. 21

2.6 (a) Measured reflection coefficient of the near-field antenna when placed on the cheek and phantom stack. (b) Total E-field magnitude on the conductor surface of the near-field antenna at 1.4 GHz when placed on the cheek. This indicates the normal E field of the surface. 22

2.7 Simulated Joule loss density of antenna on (a) skin-muscle phantom stack and (b) tissue stack of the cheek with 1 W of power at the feed. The weights of each layer are shown. The weights are used to estimate the temperature of the internal layer. . 23

2.8 Concept diagram of dual-feed near-field antenna. Two antenna is implemented on one hardware, separately receiving black body radiation from a skin-muscle tissue stack. (T: temperature, W: weighting factor) 24

2.9 Block diagram of internal body thermometry with dual-feed near-field antenna. This allows more information on multi-stack tissue layers. 24

2.10 (a) Cross section of the two-feed near field antenna. (b) Reflection coefficient of near-field antenna when placed on the skin-muscle phantom. Measurement shown in solid line and simulation shown dashed line. 26

2.11 Simulated E-field magnitude at the boundary of the near-field antenna and skin phantom with 1 W on (a) Feed1 and (b) Feed2. 28

2.12 Simulated weighting factors as a function of distance from the superstrate-skin interface. The volume joule loss (W/m^3) is also shown when Feed1 and Feed2 is transmitting 1 W. 29

3.1 Concept figure 31

3.2 Block diagram of a Dicke radiometer connected to a phantom tissue stack of skin and muscle. The Dicke switch and LNA are implemented on a GaAs MMIC and followed by off-chip band-pass filter, detector, and dc amplifier. The output is digitized and processed for temperature retrieval. A thermocouple logger monitors skin temperature. 34

3.3 Circuit schematic (left) and layout (right) of the SPDT switch. Parameter values and the main metal, via, pad, capacitor, and resistor layers are shown. Several process layers are removed for clarity. 34

3.4 Measured (solid line) and simulated (dashed line) performance of the MMIC SPDT switch. 36

3.5 (a) Circuit schematic and component values for the 3-stage LNA integrated into a GaAs MMIC. The element values and bias points are shown in the table. Five distributed filters are used as matching and stability networks. (b) Layout of the chip, where the various layers are shown with different colors. 37

3.6 Simulated K factor comparison w/ and w/o filters. K> 1 for frequencies up to 80 GHz when filters are included. 38

3.7 Chip photograph of the fabricated two LNAs, 3 mm × 3 mm in size. 39

3.8 Measured and simulated (a) S-parameters and (b) NF. 40

3.9 Photograph of the GaAs MMIC SPDT switch and a 3-stage LNA. The total chip dimensions are 3.75 mm × 1.7 mm. 42

3.10 Measured (solid line) and simulated (dashed line) S-parameter magnitudes of the packaged SPDT switch and LNA MMIC portion of the Dicke radiometer. A coaxial calibration is performed to the connector reference planes. 43

3.11 Measured and simulated stability K factor of the MMIC (LNA with switch), as well as simulated LNA K factor. The measured K factor of the LNA alone is not calculated since the reverse isolation was below the noise floor in the S-parameter measurement. 43

3.12 Measured and simulated noise figure of the packaged SPDT switch and LNA MMIC front end of the Dicke radiometer. 44

3.13 Measured (solid line) and simulated (dashed line) gain from the input of the *on* switch of the packaged MMIC to the output of the off-the-shelf bandpass filters. The gain has a 3-dB bandwidth of 64 MHz from 1.38 to 1.44 GHz. 44

3.14 Measured voltage responsivity of the radiometer from the through port to the output of the dc amplifier. The responsivity is 213 GV/W at 1.4 GHz. 45

3.15 Measured frequency response of the entire Dicke radiometer responsivity when the input switch is *on*. 45

3.16 The Allan deviation of the Dicke radiometer to 100 sec integration time, obtained from measured data. A minimum in the Allan deviation is observed at an integration time of approximately 10 seconds, with a value on the order of $1.06 \cdot 10^{-4}$. In this work, an integration time of $\tau = 2\,\mathrm{s}$ is used, with a corresponding Allan deviation of $1.7 \cdot 10^{-4}$. 46

3.17 Circuit schematic for the Dicke radiometer with a SP3T switch and a 3-stage LNA. Transistor sizes, biasing voltages, and dc currents are shown in the figure. Stability is ensured through RC feedback in each stage, as well as low-pass and high-pass filters at the gates, and verified through Nyquist simulations. 48

3.18 Photograph of SP3T switch and LNA for a Dicke radiometer. The size of the MMIC is $3\,\mathrm{mm} \times 1.1\,\mathrm{mm}$. 49

3.19 Measured and simulated S-parameter magnitudes and noise figure of the SP3T switch and LNA MMIC for a Dicke radiometer. 49

4.1 Block diagrams of correlation and hybrid radiometers, showing noise sources $n_i(t)$. . 52

4.2 Photograph of the hybrid radiometer prototype. Off-the-shelf components are used on a 10 cm× 7.6 cm PCB. 54

4.3 Simulated (dashed) and measured (solid) S-parameters of the radiometer prototype using components from Table 4.1. The shaded area indicates the design frequency band. 55

4.4 Measured voltage responsivity of the detector at 1.415 GHz. 55

4.5 Measurement setup for temperature load testing. The design of the temperature controlled load using Peltier cell is shown. Two of these loads at temperature T_1 and T_2 are connected to the input of the radiometer and the dc output voltage of V_1 and V_2 are measured with an oscilloscope. 56

4.6 Measured temperature estimated from two calibration methods, measured on two different days, with and integration time of 5 seconds. 58

4.7 Block diagram of the correlation-Dicke hybrid radiometer for internal tissue thermometry. 59

4.8 (a) Schematic and (b) layout of MMIC with two hybrid couplers, one-stage LNA in each path, and an SPDT switch. 60

4.9 (a) Schematic of lumped-element on-chip hybrid coupler (b) Layout of hybrid coupler. 61

4.10 (a) S-parameter magnitude and (b) phase difference of S21 and S31 of the hybrid coupler. The coupler performance with PDK components is shown in dashed lines, and the performance with EM simulation is shown in solid lines. 62

4.11 Measured (solid line) and simulated (dashed line) S-parameter magnitude and noise figure of the MMIC hybrid radiometer. 63

4.12 Photograph of hybrid correlation-Dicke radiometer mounted on a PCB. An on-chip hybrid radiometer MMIC, BPF, and on-chip three stage LNA are placed in order. The size of the PCB is 42.7 mm x 30 mm. 64

4.13 (a) Measurement of RF gain of the radiometer from the inputs to the node before the detector. (b) Measured responsivity (V_{dc}/P_{RF}) of the radiometer. 65

5.1 Cross-section of the near-field antenna designed for thermal power retrieval, featuring a high sensing coefficient from the muscle phantom layer (left), along with top view of the near-field antenna with detailed parameters (right). Details about the design is given in chapter 2.3. 69

5.2 Photograph of test setup for temperature measurement. 69

5.3 Illustration of the two-layer measurement setup. Two bags of saline muscle phantom ($\epsilon_r = 77.7, \sigma = 1.26$) are used. One is a hot phantom at 60°C, and the other is a cold phantom kept at room temperature, 25°C. These two phantoms are placed alternately one at a time under the skin phantom ($\epsilon_r = 28, \sigma = 0.84$) . The output voltage is then data processed and the estimated temperature is compared to the real "ground truth" temperature. 70

5.4 Measured calibrated output of the detector when a hot (60 °C) and cold (25 °C) muscle phantom is placed under the skin phantom approximately at 20 s intervals. The output voltage increases with the hot muscle phantom, as expected. The spikes around 20, 40 s, etc., shaded in gray, are periods when the muscle phantom is alternated and the antenna is thus not behaving as designed. 71

5.5 Full-wave simulations of volume Joule loss density (W/m^3) of the near-field antenna on a skin-muscle phantom with 1 W at the feed. The weighting factors (percentages of total power) are also stated, with approximately 3% of the total power being in the surrounding air and unaccounted for here. The thickness of the skin is 2 mm and the thickness of the muscle is 15 mm. 72

5.6 Measured temperature of the muscle tissue phantom, using T_{skin} (green line) measured by a thermocouple and subtracted in post-processing. The red and blue dotted lines show the temperatures of the water bath used to set the known phantom temperature, 60°C and 25°C. 72

5.7 Full-wave simulations of volume Joule loss density (W/m^3) with 1 W at the feed. Play-Doh is used as a muscle phantom instead of saline. A thermal insulator is placed between the skin and muscle layer to delay the time of thermal equilibrium. The weighting factors (percentages of total power) are also stated. The thickness of the skin and muscle is 2 mm and 15 mm. 73

5.8 Temperature measurement (with thermocouple) and estimation (from radiometer output) when Play-Doh muscle phantom is placed under the skin phantom. Both hot Play-Doh (top) and cold Play-Doh (bottom) tests are conducted for validation across temperatures. 74

5.9 Top view and cross-section of the near-field antenna designed for thermal power retrieval. The sides of the antenna are covered by metal shielding. 75

5.10 (a) Measurement setup of temperature measurement on a 2-layer phantom. (b) Measured temperature of 2 layer phantom. Skin temperature is subtracted from the total temperature to derive T_{muscle}. (c) plot compares T_{muscle} from the thermocouple measurement. T_{m1} and T_{m2} is the temperature measured from the thermocouple at the top and bottom of the muscle phantom. $T_{m\prime}$ is the average of T_{m1} and T_{m2} and $T_{m\prime\prime}$ is the combination of T_{m1} and T_{m2} in 6:4 ratio. 76

5.11 (a) Cross section of the two-feed near field antenna. (b) Reflection coefficient of near-field antenna when placed on the skin-muscle phantom. Measurement shown in solid line and simulation shown dashed line. 78

5.12 Temperature measurement of the system using 2-layer tissue phantom stack up, showing thermocouple "ground truth" measurements in dashed line. T_{total1} and T_{total2} are measured when the switch connects the radiometer input to Feed1 and Feed2, respectively. 79

6.1 Cross-section of the near-field antenna designed for thermal power retrieval, featuring a high sensing coefficient from the muscle phantom layer (left), along with top view of the near-field antenna with detailed parameters (right). Details about the design is given in chapter 2.3. 82

6.2 Photograph of test setup for temperature measurement. Hot and cold muscle phantoms are alternated and placed on top of the skin phantom, with the near-field antenna underneath and not visible in the photo. 82

6.3 *In-vivo* measurement conducted on a human cheek. The near-field antenna is placed on the cheek to measure the temperature of hot or cold water inside the mouth. A thermocouple is placed inside the mouth to independently measure water temperature. (Courtesy Sofia Mvokany, University of Colorado, Boulder.) 83

6.4 *In-vivo* temperature measurements on the cheek with hot water (top) and cold water (bottom) in the mouth. The temperature of the skin and the water inside the mouth is measured independently with thermocouples. 84

6.5 Photograph of the hybrid radiometer prototype. 85

6.6 Measured reflection coefficient magnitude of the near-field antenna when placed on the cheek, comparing the match in air, on the cheek and simulations on the cheek. The shaded area is the design frequency band. 86

6.7 Full-wave simulations of volume Joule loss density (W/m^3) of the near-field antenna on a cheek tissue stack. The weights (percentage of total power) of cheek tissue layers are also stated. 86

6.8 Top: Measured voltage at output of the radiometer as cold water in the mouth warms up. The temperature is measured with a thermocouple in the mouth. Bottom: Measured ΔV versus time for the same data set, with a linear fit and error of ΔV compared to the measured temperature. 87

6.9 Top view and cross-section of the near-field antenna designed for thermal power retrieval. The sides of the antenna are covered by metal shielding. Details in Chapter 2.4. 88

6.10 Photograph of hybrid correlation-Dicke radiometer mounted on a PCB. Details in chapter 4.2. 88

6.11 *In-vivo* temperature measurement on the cheek with liquid in the mouth. The temperature of the liquid, skin, and antenna is measured independently with thermocouples. 89

6.12 Measured temperature of liquid using radiometer output. The temperature is compared with the real-time temperature measured with a thermocouple inside the mouth. 90

6.13 Radiometer *in-vivo* measurements repeated on multiple days for three subjects. The near-field antenna is placed on and off the cheek of the subjects. The transition period when the antenna is not on the cheek is shown in grey. 91

6.14 Side-by-side comparison of simulated volume loss density when skin properties are varied. Left: skin phantom properties: thickness, h=1.84 mm, ϵ=30.8, and σ=0.756 S/m. The resulting skin weighting factor is 22.7%. Right: skin phantom properties: h=2.16 mm, ϵ=25.2, and σ=0.924 S/m. The resulting skin weighting factor is 33.5%. 93

7.1 (left) Sideview of a GCPW measuring the permittivity of material ϵ_{r3}. ϵ_{r2} is the PET layer and ϵ_{r1} is a known substrate. (right) Extracted permittivity of Rogers 6010. Measurement shows error within 10% 99

7.2 A shielded metal box is used to reduce RFI, covering the radiometer circuit to improve measurement accuracy. The right figure shows the time transient of the radiometer's output voltage. When the box is open, RFI introduces instant spikes in the output voltage, leading to temperature measurement errors. With the metal box closed, the spikes are significantly reduced, resulting in more stable output voltage and improved measurement reliability. 101

7.3 Previous work has demonstrated the use of a neural network model to estimate the thickness of tissue layers [9]. Tissue-dependent weighting factors are then applied to estimate the temperatures of individual layers. In this approach, a wideband antenna collects reflectometry data from a VNA operating in the 2 to 13.5 GHz range. The collected data is processed using a long short-term memory (LSTM) algorithm to determine the layer properties. 102

Chapter 1

Introduction

Contents

1.1 Motivation **1**

1.2 Existing Methods **3**

1.3 Microwave Thermometry **4**

1.4 Previous Research **9**

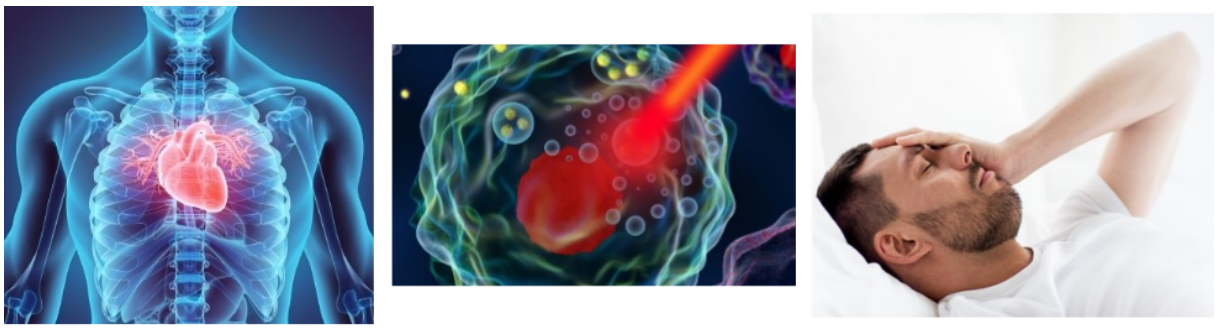
1.5 Radiometer Miniaturization **11**

1.6 Thesis Goal and Outline **12**

1.1 Motivation

Knowledge of internal tissue temperature has numerous medical applications, ranging from surgical and therapeutic to wellness. Several examples are illustrated in Fig. 1.1, with key applications where precise temperature knowledge is essential, each of which is described in detail below.

Artificial hypothermia in cardiac surgery: In emergency cardiac repair surgeries, artificially induced hypothermia is a critical step, as it allows clinicians to safely halt the blood supply to the brain temporarily while minimizing the risk of tissue damage [2]. However, to prevent brain injury, a smooth return to normothermia is required within only 30 minutes. Throughout this procedure, brain temperature monitoring is typically conducted via a proximal nasal catheter [10], which provides indirect measurement. However, this measurement often has a delayed response and does not provide an accurate real-time measurement of the brain temperature.



(a) (b) (c)

Figure 1.1: Accurately assessing internal body temperature has significant implications for various medical applications, including: (a) Measurement of brain temperature during cardiac surgery to about 15°C [2], (b) precise temperature measurement of the tumor tissue during hyperthermia treatment [3], and (c) tracking core body temperature for monitoring sleep disorder [4].

Hyperthermia treatment: During hyperthermia treatment, tumor tissues are carefully heated to approximately 40 °C. This approach reduces the amount of chemotherapy required, thereby minimizing side effects and improving the patient's quality of life [11][12][3]. However, despite the therapeutic potential, challenges remain. There is currently no reliable method to accurately measure the temperature of the tumor and its surrounding tissues in real-time. Accurate temperature monitoring is essential to ensure optimal heating of the targeted area without affecting nearby healthy tissue.

Monitoring sleep disorder: Measuring core body temperature is an important tool in the monitoring and management of sleep disorders. Approximately 60 million adults in the U.S. experience frequent sleep difficulties. Sleep disorder impacts individual well-being as well as significant cost, with an estimated annual indirect cost of $60 billion due to reduced productivity [4]. The internal body temperature is synchronized with melatonin levels and sleep propensity. This relationship is depicted in the plot in Fig. 1.2 [4], showing internal body temperature changes in synchrony with melatonin. Thereby, tracking temperature fluctuations can provide insights into sleep disorders.

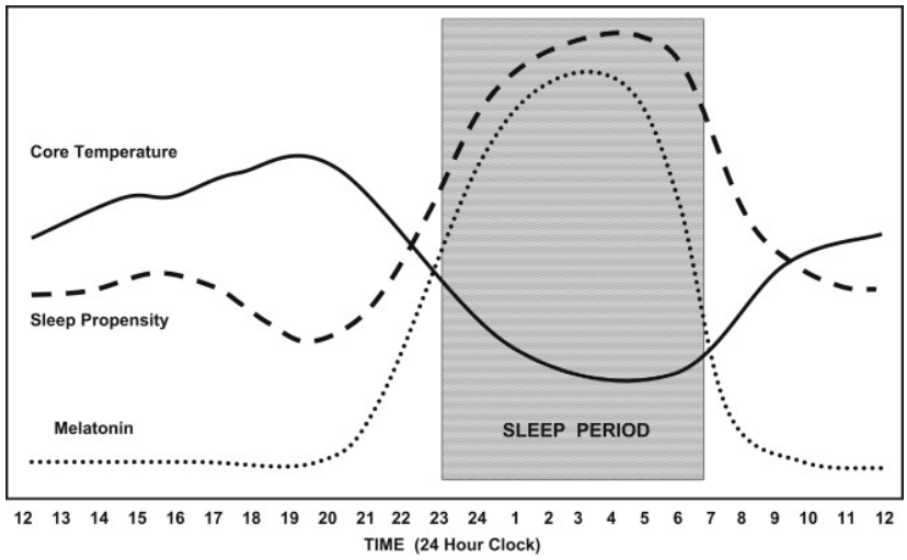


Figure 1.2: Illustration of the relationship between core temperature, likelihood of sleep, and melatonin. The figure is provided by [4].

Heat-related injury: Monitoring muscle temperature in individuals exposed to high physical stress, such as first responders, athletes, and military personnel, can help prevent heat-related injuries. By monitoring muscle temperature in real-time, overheating can be recognized early, allowing the prevention of heat exhaustion, heatstroke, and other conditions. Additionally, temperature tracking enables optimal performance management, ensuring these individuals can operate at peak efficiency [13, 14].

Infection and inflammation indicators: Internal tissue temperature serves as a critical indicator of infections, joint inflammation [15], and burn healing [16]. An increase in temperature can signal potential infection or inflammation in joints. In burn patients, monitoring temperature in affected tissues provides crucial insights into the healing process, helping clinicians to adjust treatments and enhance recovery outcomes.

1.2 Existing Methods

Currently, there is no commercially available wearable device capable of non-invasively measuring temperature at depths of a few centimeters within the body. Various methods exist to measure internal body temperature, each with distinct limitations, as illustrated in Fig. 1.3.



(a) (b) (c)

Figure 1.3: Existing methods for internal body thermometry. (a) Thermometer pills, (b) MRI, and (c) heat-flux device.

Invasive methods, such as needle probes and ingestible radio pills, offer accurate internal temperature readings but come with notable drawbacks. Needle probes, though precise, are invasive and uncomfortable, making them unsuitable for continuous temperature monitoring outside clinical settings. Radio pills are difficult to localize within the body and can produce variable, unreliable measurements influenced by food intake and intestine temperature. Furthermore, both methods are single-use, which adds to their cost over time, especially in scenarios requiring repeated monitoring.

Non-invasive approaches have also been explored but have limitations. For example, Magnetic Resonance Imaging (MRI) can measure internal temperature accurately [17], yet its high cost and non-wearable nature make it impractical for continuous or outside clinical settings monitoring [18][19]. Heat-flux devices, demonstrated in clinical settings [20] can measure temperature indirectly by measuring the heat flow from the internal to the surface during thermal equilibrium. However, this is limited to detecting it at shallow depths below the skin on the order of 1 cm due to the thermal resistance of the tissues. Recently, heat-flux sensors have been adapted for wearable use, primarily focusing on exercise monitoring [21]. Despite the existence of these methods, there remains a need for a non-invasive, wearable device that can measure temperature at greater depths within the body, a few cm at least with some spatial resolution.

1.3 Microwave Thermometry

Microwave thermometry offers a promising solution for a non-invasive, passive, and wearable device capable of measuring subcutaneous internal temperature.

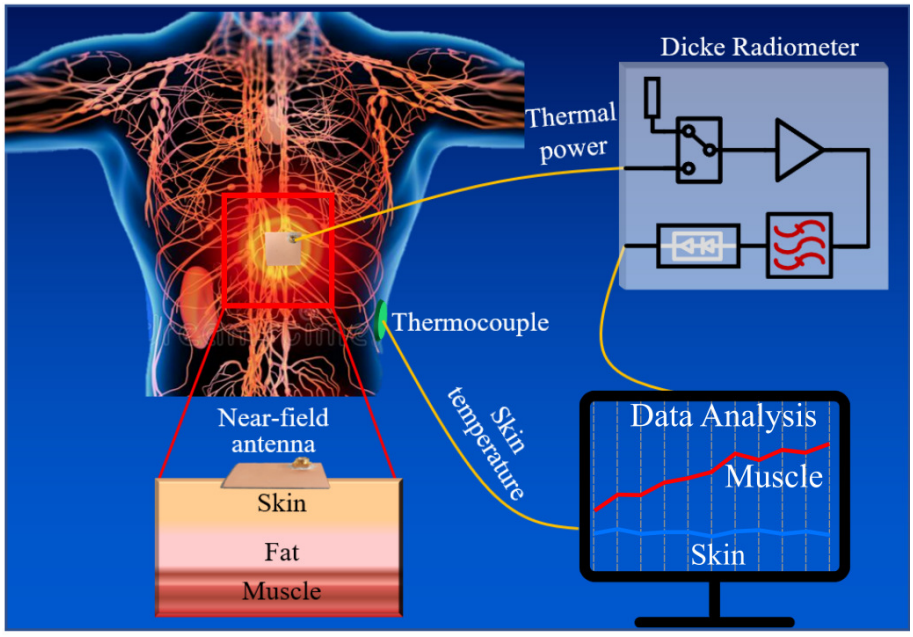


Figure 1.4: Illustration of non-invasive internal body thermometry using a microwave radiometer placed below the sternum [5]. A near-field antenna is placed on the skin to detect thermal power from a stack of tissue layers. This signal is transferred to a low-noise receiver, depicted as a Dicke radiometer in this example, and processed through a temperature estimation algorithm. A thermocouple on the skin provides additional data to enhance the accuracy of the temperature estimation algorithm.

The method estimates the temperature of specific tissue layers by analyzing the total thermal noise power emitted from a combination of layered tissues [22, 23, 24, 25]. The high-level approach is shown in Fig. 1.4. The system involves a near-field antenna placed on the skin, which passively captures thermal power from various tissue layers. To detect this extremely low-power signal (in the range of tens of fW), the system uses a highly sensitive receiver known as a radiometer, which amplifies and processes the captured thermal noise. The figure shows a type of radiometer known as a Dicke radiometer, a widely used design in radiometry. Additionally, a separate thermocouple placed on the skin provides data for an estimation algorithm used to determine the temperature of the inner tissue layers.

Microwave thermometry functions by detecting black body radiation, which is noise present in all materials at temperatures above absolute zero (0 K). This phenomenon is a fundamental concept in thermodynamics, as in Oliver's excellent review on thermal and quantum noise [26].

Oliver's paper starts with the basic laws of thermodynamics and Planck's law, stating that the average energy in a resonator per mode is given by $\overline{W} = \frac{hf}{e^{hf/kT}-1}$, where h is the Planck constant ($6.63 \cdot 10^{-34}[\frac{\mathrm{m^2kg}}{\mathrm{s}}]$), k is Boltzmann constant ($1.38 \cdot 10^{-28}[\frac{\mathrm{m^2kg}}{\mathrm{s^2K}}]$), f is the frequency (Hz), and T is the temperature (K). Building on these principles, the paper proceeds to calculate the volumetric and spectral mode density in one (m_1) and three dimensions (m_3). Since each mode possesses an average energy $\overline{W}$, the thermal energy density(ρ) is expressed as $\rho = m\overline{W}$.

Referring to Fig. 1.6, where a 1-D transmission line feeds a 3-D antenna, we first find the equation of the power ρ_1 on a resonant line. Assume that the 1-D shorted resonant transmission line has a length $l = n\lambda/2 = nc/2f$, where n is an integer number, λ is the wavelength, and c is the velocity of propagation. For a sufficiently long l, the mode density becomes frequency-independent and can be represented as $m_1 = \lim_{l\to\infty} \frac{1}{l}\frac{dn}{df} = \frac{2}{c}$. This expression describes the number of modes per unit length per unit bandwidth in a 1-D transmission line. When this transmission line is connected to a matched load Z_0 in thermal equilibrium, the load delivers and absorbs an equal amount of power to the transmission line. The energy density in the line is thus given by $\rho_1 = m_1\overline{W} = \frac{2}{c}\frac{hf}{e^{hf/kT}-1}$. To obtain the amount of power flowing in one direction along the transmission line, the energy density has to be multiplied by propagation velocity and divided by 2. The division by 2 is necessary because the energy density equally contributes to the power propagating in the forward and backward directions. This results in the power expression $p = \frac{hf}{e^{hf/kT}-1}$.

When extended to 3-D, accounting for two polarization states, the number of modes per volume per Hz is $m_3 = \frac{8\pi f^2}{c^3}$. In this 3-D scenario, the mode density is proportional to the square of the frequency. The average electromagnetic energy density in the cavity can be expressed as:

$$\rho_3 = m_3\overline{W} = \frac{8\pi h f^3}{c^3}\frac{1}{e^{hf/kT}-1} \tag{1.1}$$

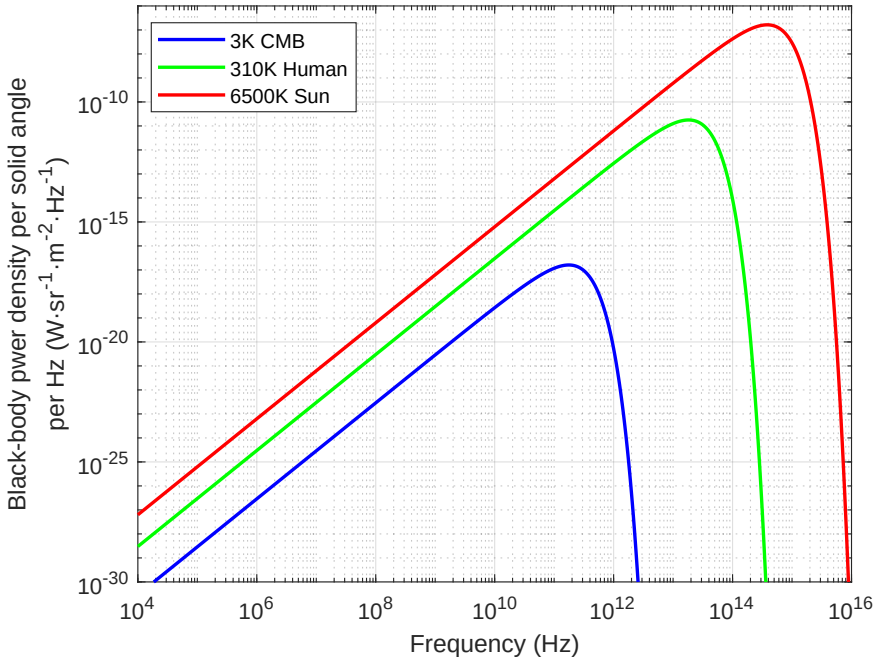


Figure 1.5: Black-body intensity curve of spectral radiance. Curves are shown for the temperature of the Cosmic Background Radiation (CMB), a healthy human, and the sun.

This equation defines the black body radiation curve, which is essential for understanding the thermal emission of objects of various temperatures. Black body curves for Cosmic Microwave Background (CMB), healthy humans, and the Sun are illustrated in Fig. 1.5. For a healthy human body temperature around 310 K, the black body curve peaks in the infrared frequency range at approximately 18 THz. However, at this frequency, the electromagnetic wave penetration into most tissues is limited to depths on the order of millimeters. For example, the plane-wave sensing depth in various tissues is shown in Table.2.2. Therefore, infrared thermometry primarily captures skin temperature rather than deeper tissue temperatures. This depth at which temperature can be measured is referred to as the "sensing depth". To achieve greater sensing depth, microwave frequencies are employed. However, microwave frequencies are on the tail of the power spectral density curve described by eq. 1.1.

Coming back to the 3-D case, the black-body object can be modeled as a matched transmission line connected to an antenna within an enclosed thermal equilibrium environment, as shown in Fig. 1.6. In this thermal equilibrium setup, the power delivered from the transmission line and

radiated by an antenna equals the power received by the antenna ($P_{rad} = P_{rec}$). The total power received by the antenna can be written as:

$$P = \frac{hfB}{e^{\frac{hf}{kT}} - 1} \tag{1.2}$$

Since $hf/kT \ll 1$ at microwave frequencies, the power spectral density P can be approximated as $P = kTB$. This approximation implies that, in a radiometer system, the power received from a stack of tissue layers will be directly proportional to the tissue temperature. By capturing this power using a near-field antenna, the system can estimate internal temperatures based on the detected thermal noise emissions.

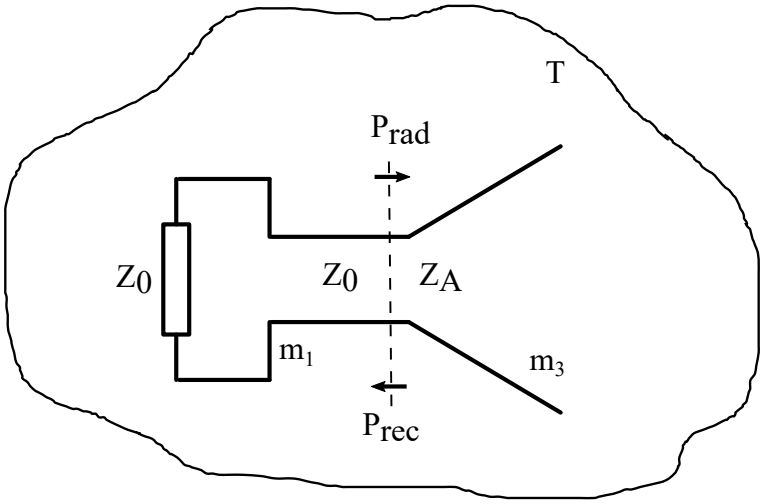


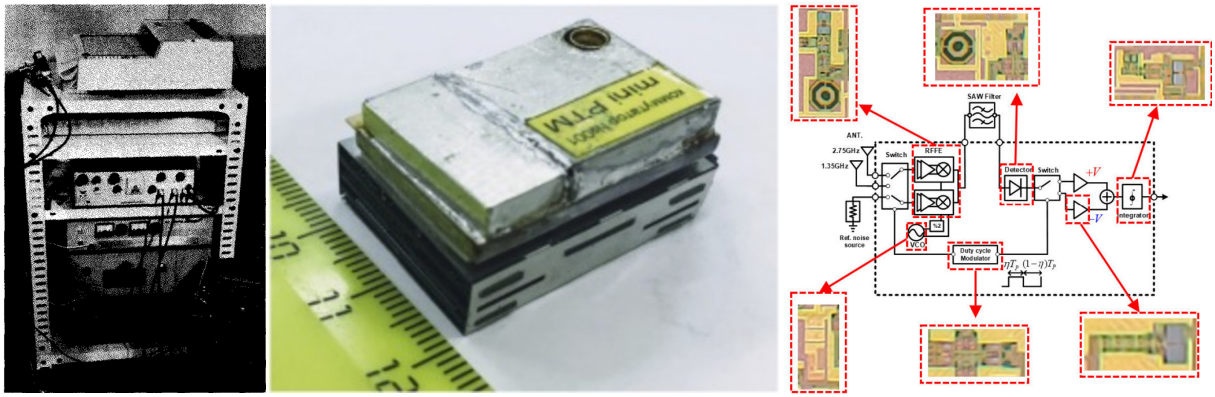
Figure 1.6: An antenna transmitting and receiving in a closed system in thermal equilibrium.

In the U.S., various frequency bands have been designated for distinct purposes, such as television broadcasting and mobile communications. Among these, the band from 1.4 to 1.427 GHz stands out as a relatively narrow band reserved exclusively for passive radio astronomy. This "quiet band" offers minimal radio frequency interference(RFI), making it ideal for sensitive passive measurements. The $f = 1.4$ GHz frequency has been selected as the operating frequency for microwave thermometry due to its advantageous combination of factors: it provides sufficient sensing depth, receives low RF interference, and supports manageable component sizes, such as the size of the

near-field antenna.

1.4 Previous Research

Microwave radiometry for internal tissue measurements has been demonstrated in the literature over the past few decades.



(a) (b) (c)

Figure 1.7: Previous works on microwave radiometers for internal body temperature measurement. (a) Multi-frequency Dicke radiometer at at 1.5, 2.5, and 3.5 GHz [6]. (b) Dicke radiometer at 3.4–4.2,GHz with a circulator at the input [7]. (c) Dual-band Dicke radiometer operating at 1.35 and 2.75 GHz implemented on CMOS [8].

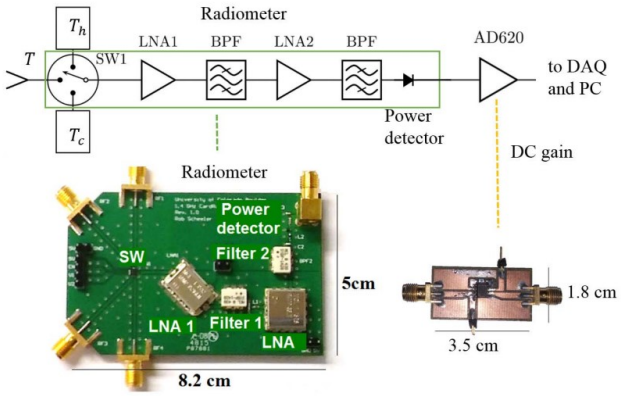
For instance, a multi-frequency Dicke radiometer operating at 1.5, 2.5, and 3.5 GHz with a 1 GHz bandwidth is shown in Fig. 1.7(a) [6]. This microwave radiometer was used in a water-bath experiment, demonstrating its capability to measure the temperatures of the surface layer, the subjacent layer, and the boundary depth between these layers, showcasing its capability to capture temperature gradients at different depths.

In another study, a Dicke radiometer operating at 3.4–4.2,GHz with a circulator for reducing reflection coefficient fluctuations is presented in Fig. 1.7(b) [7]. With a power consumption of 1.05 W, this radiometer has applications in breast cancer detection and back pain assessment.

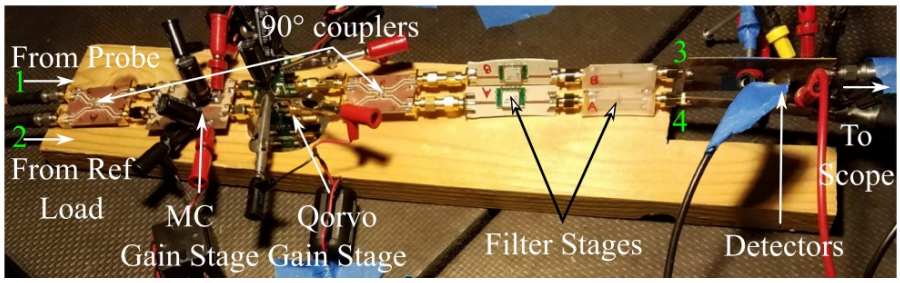
Another example is a dual-band Dicke radiometer operating at 1.35 and 2.75 GHz, implemented on a 65 nm CMOS process to achieve a compact design, as shown as Fig. 1.7(c) [8]. This radiometer employs two 50 Ω noise sources for precise temperature measurements, achieving an error

of less than 0.9 °C was obtained under room temperature conditions.

Additional studies have explored other frequency ranges and applications. A 0.9–1.2 GHz Dicke radiometer with a matched loop antenna, positioned on the stomach, was used to observe a 1.5,°C temperature change following the ingestion of cold water [27]. Another study implemented a 45 GHz radiometer with a horn antenna to capture body temperature images, which successfully revealed the location of the heart [28].



(a)



(b)

Figure 1.8: Previous works on microwave radiometers for internal body temperature measurement from University of Colorado Boulder. (a) Dicke radiometer (b) modular correlation radiometer.

Microwave radiometer research at the University of Colorado Boulder has also contributed significantly to this field. A 1.4 GHz Dicke radiometer with off-the-shelf components, with a power consumption of approximately 0.6 W and a noise figure of 1.58 dB, is demonstrated in Fig. 1.8(a) [23]. This radiometer successfully measured the temperature of a muscle tissue phantom beneath skin and fat layers with a resolution as low as 0.2 K. More recently, Fig. 1.8(b) [29] shows a modular correlation radiometer design using off-the-shelf components.

Previously published radiometers, which were built from off-the-shelf components, typically have a minimum size of about 3 cm × 3 cm, which poses limitations for wearable applications. To address the need for a smaller and more power-efficient radiometer, this thesis proposes a monolithic integration of key radiometer components. This integrated approach is intended to produce a compact, wearable, and low-power device that is less susceptible to interference, positioning it as an ideal candidate for continuous internal temperature monitoring.

Table 1.1: Microwave radiometers for internal body thermometry

Radiometer	f **(GHz)**	**Type**	ΔT
IMS 1984 [6]	1.5, 2.5, 3.5	Dicke	0.5
Emerg. Elec. 2018 [30]	1.1-1.6	Dicke	0.5
Sens. 2021 [7]	3.4-4.1	Dicke	0.2
Access 2023 [8]	1.35, 2.75	Dicke	0.9
This Work	1.4	Hybrid	0.35

1.5 Radiometer Miniaturization

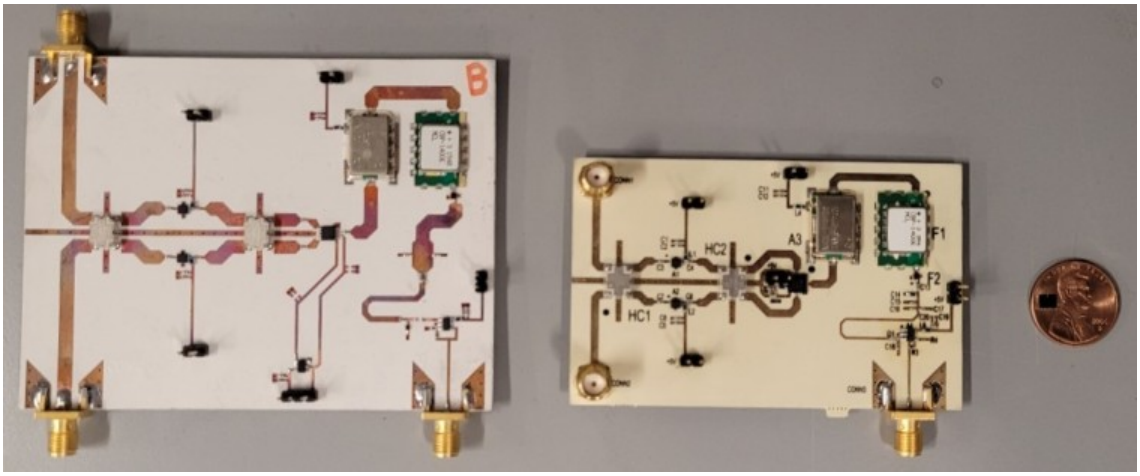


Figure 1.9: Illustration of a few different radiometers describe for this work. From left to right, the form factor of the radiometer is reduced for wearability. A radiometer MMIC is placed on top of a penny.

The focus of this thesis is on the miniaturization of the radiometer hardware to enable continuous monitoring of internal body temperature across various environments. A compact and wearable device is essential to meet the practical demands of long-term temperature measurement applications. As illustrated in Fig. 1.9, several radiometer designs are presented, each achieving a progressively smaller form factor than its previous version. To further reduce the size, the radiometer is implemented on a Monolithic Microwave Integrated Circuit (MMIC), which integrates multiple radiometer components into a single chip. This approach not only significantly decreases the device's physical dimensions but also minimizes the potential for external interference, as the compact structure reduces signal paths and the associated exposure to ambient noise sources.

1.6 Thesis Goal and Outline

With the goal of miniaturizing the radiometer for wearable applications, continuous research for miniaturized radiometer design is needed. This thesis demonstrates the design of different radiometers capable of sensing to a depth of approximately 3 cm beneath the skin and advanced measurement methodologies.

Chapter 2 outlines the design of the near-field antenna, which is used to capture blackbody radiation emitted from layered tissues. Various types and near-field antennas are explored to optimize size reduction while mitigating the reception of RFI, which is critical for enhancing measurement accuracy in diverse environments.

Chapter 3 provides an overview of different radiometer architecture options, emphasizing key design tradeoffs and parameters that motivate the choice of hybrid radiometer architecture. This hybrid concept is illustrated first through the design of a PCB using off-the-shelf components, followed by implementation on a GaAs MMIC to achieve greater miniaturization and efficiency.

Chapter 4 describes the MMIC design of a Dicke radiometer, focusing on the detailed design of essential components such as the LNA and RF switch. Packaging considerations for the MMIC are also discussed to ensure connection to the near-field antenna as well as other components.

Chapter 5 presents experimental results from radiometry measurements and temperature

estimation across various phantom tissue configurations. These results validate the accuracy and depth of the radiometer's sensing capabilities under controlled scenarios.

Chapter 6 extends the testing to *in-vivo* measurements, where the near-field antenna is positioned on the cheek to measure temperature variations of a liquid inside the cheek. This setup demonstrates the device's capability to capture real-time internal temperature changes in a biologically relevant setting.

Chapter 7 concludes with a summary of the key contributions of this work and proposes directions for future research.

Chapter 2

Nearfield Antenna

Contents

2.1 Introduction **14**

2.2 Weighting Factor Analysis **15**

2.3 Rectangular Patch Antenna **18**

2.4 Slotted Circular Antenna **21**

2.5 Two-feed Antenna **23**

2.6 Conclusion **29**

2.1 Introduction

For a microwave thermometer, a near-field antenna is connected to the input of the radiometer. Unlike typical free-space radiators, near-field antennas are specifically designed to detect black-body radiation emitted from subcutaneous tissue layers. Key design goals for these antennas include achieving a compact form factor suitable for wearable applications, along with providing spatial resolution in the lateral dimension, and ensuring sufficient sensing depth in the vertical direction to capture temperature readings from layers within.

Previously published works have examined various antenna topologies, which are summarized in Table. 2.1. These topologies include waveguide, cavity-backed slot, circular patch, bow-tie, and rectangular patch antennas, among others. While each design has unique benefits, many do not prioritize the efficient reception of black-body radiation from subcutaneous layers. Additionally,

many existing designs feature wideband characteristics to facilitate the reception of higher power for easier detection. Nonetheless, wideband near-field antennas can increase the system's susceptibility to radio frequency interference (RFI), which can introduce significant measurement errors, particularly in variable environments.

This chapter presents the design of several near-field antenna configurations, along with detailed analysis aimed at developing the optimal antenna for internal body temperature measurement. These antennas will be used for internal body temperature measurements presented in chapters 5 and 6.

Table 2.1: Previous works on near-field antenna for microwave thermometry

Reference	**Frequency**	**Size(mm)**	**Topology**
Sensors [31]	1.2 - 1.6	45 x 45	cavity back slot
TMTT [23]	1.4	40 x 40	circular patch
Access [32]	1.25, 2.7	20 x 30	bow-tie
APS [33]	1.4	37 x 41	rectangular patch
Dissertation [34]	1.5-3.1	29.5 x 30	folded dipole
TBME [35]	1.1-1.6	28	cavity log spiral

2.2 Weighting Factor Analysis

Before discussing the design of various near-field antennas, it is essential to understand the concept of weighting factors, which play a critical role in accurately estimating internal tissue temperatures. As mentioned in Chapter 1, a matched antenna receives thermal power, quantified as kTB, enabling the capture of temperature information from multiple tissue layers. The weighting factor is a measure that indicates the contribution of each individual tissue layer to the total received power.

Reciprocity is utilized in simulations to analyze the weighting functions of the near-field in tissue layers. While reciprocity is a well-established principle for far-field antennas, it is equally applicable to near-field scenarios. In the case of near-field antennas, the absorption of power emitted

by the antenna can predict the amount of power that the antenna will receive from the attached dielectric layers. Specifically, the power received by the antenna from a given layer is proportional to the power loss that would be observed if the antenna were transmitting through that same layer. Thus, by simulating the power absorption when transmitting, it is possible to estimate the contribution of each layer to the received signal. This method allows for an understanding of the depth-specific sensitivity of the antenna. A more detailed derivation of this approach to weighting functions in radiometric measurements is provided in [36].

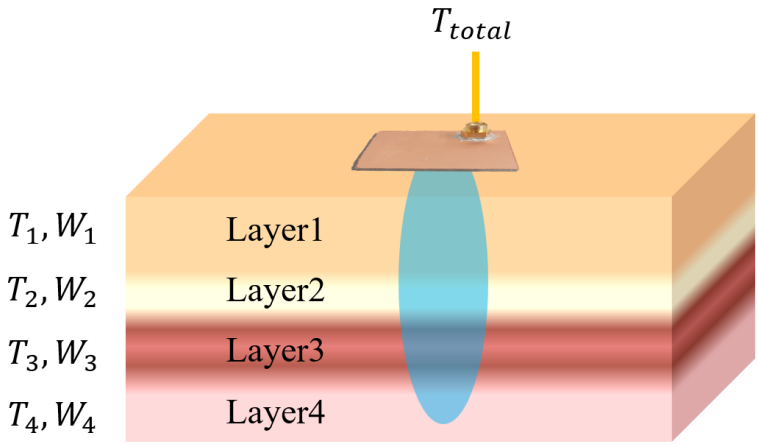


Figure 2.1: A near-field probe positioned on the stack of 4-layer tissue stack. Thermal power is received by the antenna and transferred to a radiometer to detect T_{total}, which is the weighted sum of the temperatures in different layers.

Fig. 2.1 illustrates one example of how the internal temperature is estimated, shown as a 4-layer tissue stack. In this setup, the received thermal power, represented as kTB, is measured by a near-field antenna connected to a sensitive receiver. Knowing the received power enables the calculation of the total temperature (T_{total}). The total temperature is determined by the weighted sum of the temperatures of all the layers sensed by the antenna. Specifically, T_{total} is the sum of the temperatures of each individual layer, where each layer's contribution is proportional to a specific weighting factor. Consequently, the total thermal noise power received by the near-field antenna is defined by a weighted sum of the power contributions from each tissue layer within the sensing depth. This relationship can be expressed as:

$$T_{total} = \sum_{i=1}^{N} W_i \cdot T_i \ \ , \tag{2.1}$$

Where T_i is the temperature of the i-th layer, W_i is the weight representing the contribution of the i-th layer to the total received power, and N is the number of significant layers, including a lossy antenna. This weighted sum approach enables an estimation of the internal temperature by taking into account the contribution of each tissue layer to the overall thermal noise power received by the near-field antenna.

In this model, the individual layer temperatures T_i are the unknowns that need to be estimated using an algorithm. Accurate estimation requires prior knowledge of the weighting factors W_i. These weights are derived from a 3-D electromagnetic simulation. In this work, Ansys HFSS software is utilized for the simulation, where a near-field antenna is modeled in contact with a stack of phantom or real tissues. Knowing the dielectric constants of each layer in the stack, which significantly impact the weighting factors, is an essential input to these simulations. The profiles of the dielectric layers used in this study are detailed in Table. 2.2.

The weighting factor W_i for each layer is determined by the ratio of the Joule loss in a specific volume v_i to the total Joule loss across all layers. This is expressed by the following equation:

$$W_i = \frac{\int_{v_i} \rho_J(x,y,z)\,\mathrm{d}v}{\int_V \rho_J(x,y,z)\,\mathrm{d}v} \ \ , \tag{2.2}$$

where $\rho_J(x,y,z)$ is the Joule loss density at every point within the tissue, v_i is the volume of the i-th layer, and V is the total volume of the tissue considered in the simulation.

Even with known weights W_i and T_1 obtained from a thermocouple placed externally on the skin, there are still three unknowns and only one equation. Therefore, additional assumptions are required to resolve the unknowns. These assumptions may include defining an expected temperature range for specific layers or stating that the temperature difference between two layers falls within a certain degree, thereby enabling a more accurate internal temperature estimation.

Table 2.2: Phantom and tissue electromagnetic properties at 1.4 GHz. [1]

Tissue	ϵ_r	$\sigma(S/m)$
Human skin dry	39.6	1.03
Human skin wet	44.6	1.04
Human muscle	54.1	1.14
Human fat	5.39	0.64
Skin phantom [37]	23	0.84
Saline [38]	77.7	1.26
Tap water	5.39	0.15
Playdoh	32	5.4
Rogers 6010 [39]	10.2	0.0027

2.3 Rectangular Patch Antenna

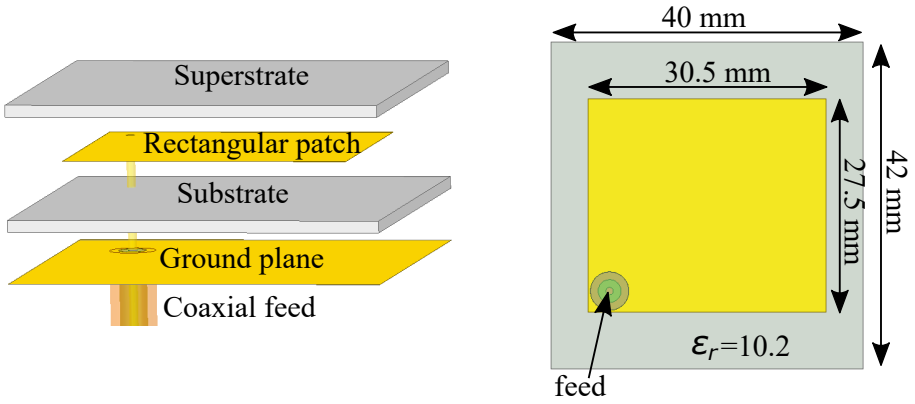


Figure 2.2: Cross-section of the near-field antenna designed for thermal power retrieval, featuring a high sensing coefficient from the muscle phantom layer (left), along with top view of the near-field antenna with detailed parameters (right).

The first near-field antenna designed for this project is a rectangular patch antenna. This topology was selected for its simplicity and because the ground plane helps reduce back lobes that could receive interference. This antenna is intended for use with both a 2-layer phantom stack, representing skin and muscle, as well as the human cheek tissue stack. The primary design objective is to capture as much power as possible from the muscle layer located beneath the skin layer. If the

weight of the skin is too high compared to that of the muscle weight, the error in estimating the muscle phantom temperature increases. This occurs because the amount of power received from the muscle decreases significantly.

To achieve these goals, a coaxial-fed rectangular patch is designed using simulation in Ansys HFSS. A 1.27 mm thick Rogers RO3010 material is used for the substrate and superstrate, with dimensions shown in Fig. 2.2. The antenna is positioned on top of a 2 mm thick commercial skin phantom layer ($\epsilon_r = 28, \sigma = 0.82\,\mathrm{S/m}$) based on the model from [37]. This layer is placed over a plastic bag filled with saline solution ($\epsilon_r = 77.7, \sigma = 1.26\,\mathrm{S/m}$) used as a muscle phantom, approximating the values given in [38]. The x and y dimensions of the tissue phantom layers are $6\,\mathrm{cm} \times 6\,\mathrm{cm}$, and the setup is surrounded by air. The Rogers RO3010 substrate has a high permittivity of $\epsilon_r = 10.2$, which reduces the size of the near-field antenna. The superstrate, placed atop the rectangular patch, serves as an intermediate matching layer to improve near-field coupling and facilitates deeper penetration into the tissues. Additionally, the superstrate reduces the sensitivity of return loss to variations in tissue layers. The resulting dimensions of the rectangular metal patch are $42\,\mathrm{mm} \times 40\,\mathrm{mm}$.

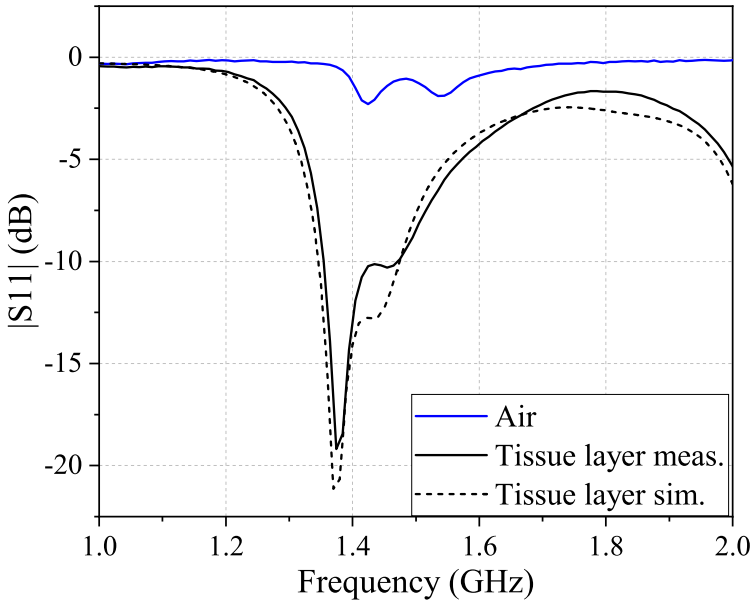


Figure 2.3: Simulated and measured reflection coefficient magnitude when the near-field antenna is placed onto the phantom tissue stack. The measured reflection coefficient is also shown for the antenna in free-space for comparison.

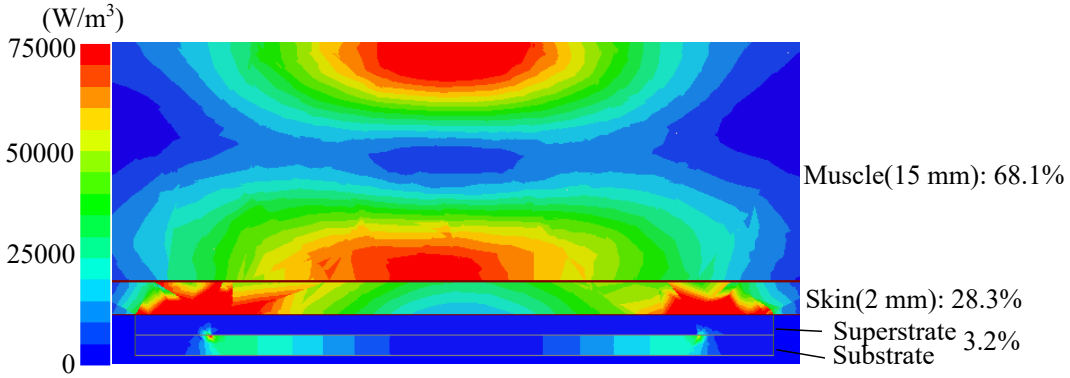


Figure 2.4: Full-wave simulations of volume Joule loss density (W/m^3) of the near-field antenna on a skin-muscle phantom with 1 W at the feed. The weighting factors (percentages of total power) are also stated, with 3% of the total power radiation into free space outside the tissue and unaccounted for here.

Figure 2.3 shows the simulated and measured reflection coefficient magnitudes of the antenna when placed onto the phantom tissue stack. The reflection coefficient is also measured in the air for comparison, demonstrating that the antenna is matched to the specific tissue stack configuration.

Fig.2.4 illustrates the full-wave simulation results illustrate the volume density of Joule loss for the near-field antenna positioned on the 2-layer skin-muscle phantom. During this simulation,

the antenna operates in transmission mode with 1 W input power at the feed. By integrating the power density of Joule losses within each layer ($\int_{V_i} p_J \mathrm{d}V_i = \int_{V_i} \sigma_i |E_i|^2 \mathrm{d}V_i$) and dividing by the total dissipated power, the weighting factor for the muscle and skin are determined. In this setup, 68% of the total power is absorbed by the muscle layer, and 28% by the skin layer, with 3% of the power, dissipated in the surrounding air, which is not accounted for in this analysis.

2.4 Slotted Circular Antenna

In the next antenna design, a circular patch antenna with slots is selected, utilizing a high-permittivity Rogers 3010 substrate ($\epsilon_r = 10.2$) to minimize size. The ground plane in this design is essential for minimizing back lobes that could pick up interference. Fig. 2.5 illustrates the cross-section of the near-field antenna design. The use of two nested C-shaped slots increases the electrical length, effectively miniaturizing the antenna to fit onto a 3.5 cm diameter substrate. The same high-permittivity material is used as a superstrate, enhancing the antenna's robustness to impedance changes caused by variations in skin characteristics. This superstrate also reduces the electric field intensity on the skin, lowering power losses in the skin layer and allowing for greater power absorption in the underlying muscle layer.

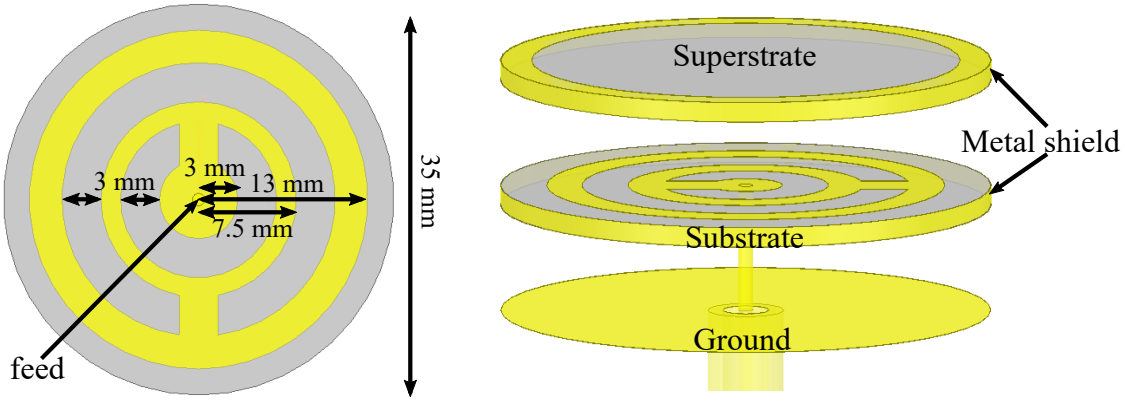


Figure 2.5: Top view and cross-section of the near-field antenna designed for thermal power retrieval. The sides of the antenna are covered by metal shielding.

The near-field antenna design incorporates a conductor around the sides of the substrate

and superstrate to reduce RFI. RFI from communication and other bands with allocations close to 1.4 GHz frequency range introduces additional power that results in an increase in measured temperature that does not reflect the body temperature increase and can result in substantial errors. By containing the fringing fields that extend to the ambient environment, the side shielding limits RFI. Simulations indicate that this side shielding reduces the amount of received RFI by more than 15% compared to an antenna without side shielding.

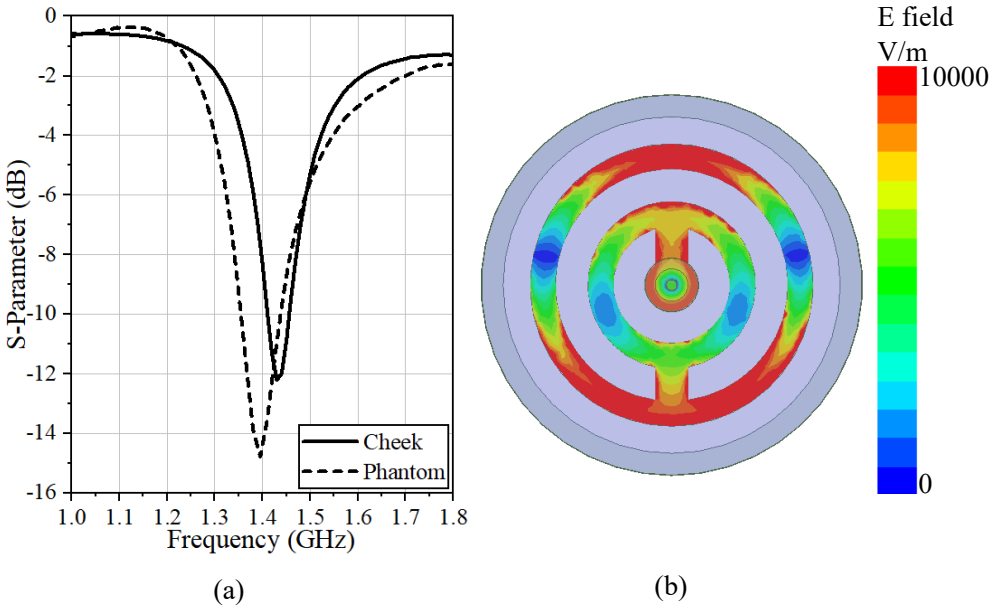


Figure 2.6: (a) Measured reflection coefficient of the near-field antenna when placed on the cheek and phantom stack. (b) Total E-field magnitude on the conductor surface of the near-field antenna at 1.4 GHz when placed on the cheek. This indicates the normal E field of the surface.

Fig. 2.6 presents the measured reflection coefficient magnitude of the near-field antenna when placed on the tissue phantom stack and the cheek. The electrical properties of the tissue layers used for the simulation are documented in [1], and the properties of liquids are found in [40]. This figure also illustrates the total E-field magnitude across the conductor surface at 1.4 GHz when the antenna is placed on the cheek.

Fig.2.7 illustrates the simulated volume density of Joule loss of the near-field antenna on the 2-layer phantom and cheek tissue stack. In these simulations, the antenna operates in transmission mode with 1 W of input power at the feed. The weighting factors for each tissue layer are also

provided. These weights are derived from the ratio of Joule loss density in each layer to the total loss and are crucial for accurate estimation of the internal temperature, as they quantify the contributions from each tissue layer to the overall received power.

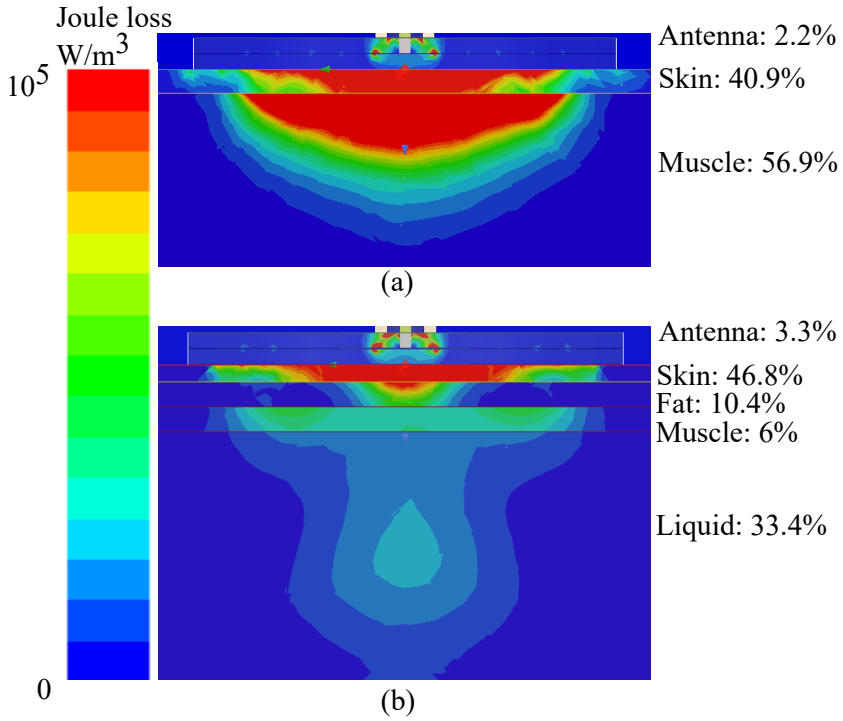


Figure 2.7: Simulated Joule loss density of antenna on (a) skin-muscle phantom stack and (b) tissue stack of the cheek with 1 W of power at the feed. The weights of each layer are shown. The weights are used to estimate the temperature of the internal layer.

2.5 Two-feed Antenna

In the case of a conventional single-feed antenna applied to an N-layer tissue model, the equation introduces N unknown temperatures $(T_1, T_2, ..., T_N)$ if there are no separate thermocouple sensor to measure the temperature of the skin. However, it provides only a single equation, thereby leading to an underdetermined system that necessitates estimation techniques to resolve this inverse problem. To address this limitation, a multiple-sensing depth antenna (Fig. 2.8) can provide additional equations through new weighting factors W_{i1} and W_{i2}, corresponding to the two feeds.

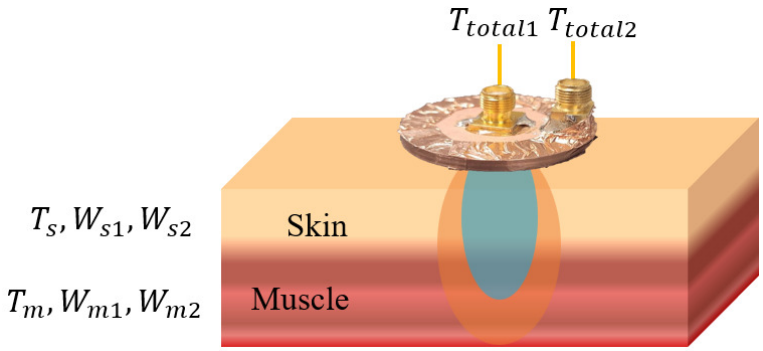


Figure 2.8: Concept diagram of dual-feed near-field antenna. Two antenna is implemented on one hardware, separately receiving black body radiation from a skin-muscle tissue stack. (T: temperature, W: weighting factor)

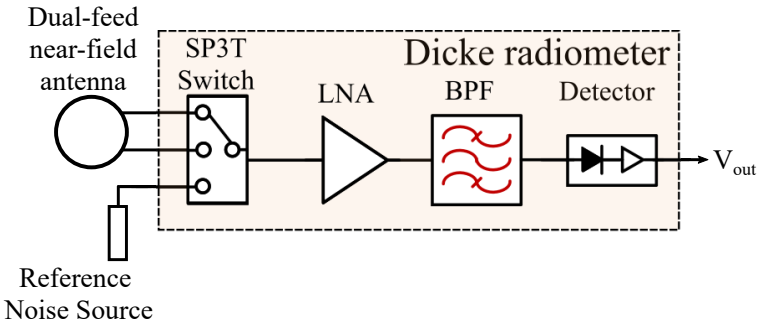


Figure 2.9: Block diagram of internal body thermometry with dual-feed near-field antenna. This allows more information on multi-stack tissue layers.

Another effective approach to achieve different weighting factors involves utilizing different operating frequencies. Previous studies have explored multi-band frequency NFAs [6, 41, 32]. Despite their potential, these solutions face significant challenges in design, characterization, and susceptibility to interference, making their implementation less practical. To address these issues, this NFA is a dual-sensing depth NFA with a Dicke radiometer, as shown in Fig. 2.9, is introduced. This NFA design enables two radiometer measurements using a single antenna and a single narrowband radiometer, simplifying implementation while improving performance.

To effectively capture black-body radiation emitted by subcutaneous tissues, a coaxial-fed circular patch antenna was designed and simulated in Ansys HFSS, taking into account the dielectric properties of tissue phantoms. The simulation setup includes a $6\,\text{cm} \times 6\,\text{cm} \times 22\,\text{mm}$ volume, surrounded by air. A 2 mm skin phantom ($\epsilon_r = 28, \sigma = 0.82\,\text{S/m}$) from [37] is placed over a 20 mm

Play-Doh muscle phantom ($\epsilon_r = 32, \sigma = 5.4\,\mathrm{S/m}$).

While earlier studies aimed at increasing sensing depth along the vertical axis [42], the unique contribution of this NFA design lies in its ability to differentiate the weighting factors for various tissue layers, e.g. in this case the skin and muscle layers. This distinction allows independent temperature measurements for each layer. For the skin-muscle phantom setup, the overall measured temperature is expressed as a weighted sum of the individual layer temperatures: $T_{total} = W_s T_s + W_m T_m$. The total temperature, T_{total}, is measured using a radiometer, as described in the next section. The weighting factors for the skin and muscle, W_s and W_m, are calculated via integration of the volume loss power density using a full-wave EM simulation tool. The weighting factors are found when the NFA transmits in simulation 1 W.

With the weighting factors obtained from EM simulations, the system reduces to two unknowns, T_s and T_m. Previous single-feed approaches lacked a method to determine the temperatures of both layers without an independent skin temperature measurement. In contrast, the dual-feed antenna enables this capability. For the two-feed design, the temperatures received at each feed can be expressed as:

$$T_{total1} = W_{s1} T_s + W_{m1} T_m \tag{2.3}$$

$$T_{total2} = W_{s2} T_s + W_{m2} T_m \tag{2.4}$$

These two equations, corresponding to the two feeds, form a solvable system with two unknowns, making it possible to independently determine the temperatures of the skin and muscle layers.

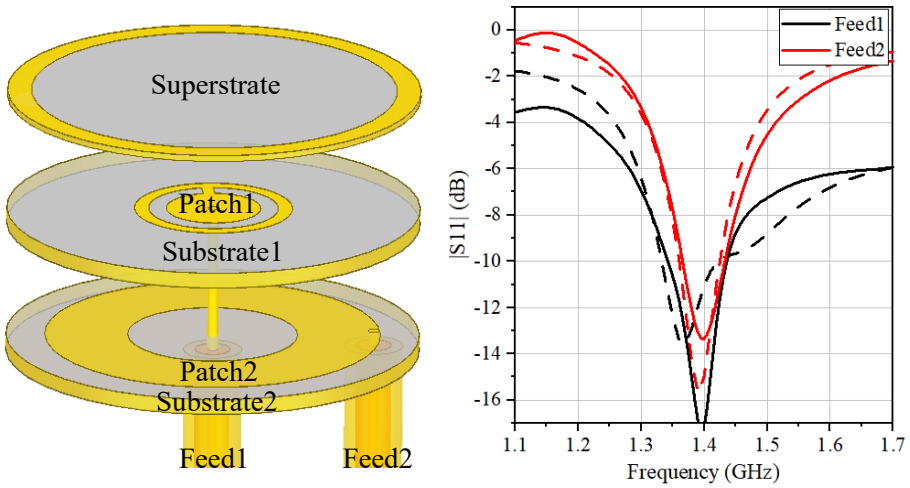


Figure 2.10: (a) Cross section of the two-feed near field antenna. (b) Reflection coefficient of near-field antenna when placed on the skin-muscle phantom. Measurement shown in solid line and simulation shown dashed line.

The determination of weighting factors is intrinsically tied to the design of the NFA. For this dual-feed antenna, the superstrate thickness plays a crucial role. To achieve a higher weighting factor for the muscle and increase the sensing depth, it is essential to minimize losses in the skin layer. Given that tissue conductivity is a fixed property, reducing the electric field strength within the skin layer is essential for maximizing the Joule loss density, p, in the muscle. This relationship can be analyzed using the boundary conditions for the electric field:

$$E_{1tang} = E_{2tang} \quad \text{and} \quad \frac{E_{1norm}}{E_{2norm}} = \frac{\epsilon_2}{\epsilon_1} \tag{2.5}$$

where the subscript "1" corresponds to the superstrate of the antenna, while subscript "2" refers to the skin. It is observed that the tangential component of the electric field remains consistent across the boundary, as it is preserved from one layer to the next. In contrast, the normal component of the electric field in the skin layer is influenced by the normal electric field in the adjacent layer, which, in this case, is the antenna's superstrate. This dependence highlights the critical role of the superstrate's permittivity and thickness in shaping the electric field distribution within the skin layer. On the other hand, the boundary condition for the current density is:

$$J_{1norm} = J_{2normal} \quad \rightarrow \quad \frac{E_{1norm}}{E_{2norm}} = \frac{\sigma_2}{\sigma_1} \tag{2.6}$$

Given the high conductivity of the skin, an excessively large tangential electric field component (E_{tang}) would result in the skin layer dominating thermal noise power emission. However, skin also has a high permittivity, therefore, with an appropriate permittivity and thickness of the superstrate, which is between the main radiator and the skin, the normal E-field component in the skin can be minimized. Thus, for an NFA with high weighting factor in a subcutaneous layer, the conductive layer of the patch is designed to have a substantial tangential component, while the superstrate is chosen to control the ratio of the normal and tangential components.

Figure 2.10(a) illustrates the cross-section of the NFA. The simulated and measured reflection coefficient magnitudes are presented in Fig. 2.10(b). The antenna is fabricated using Rogers RO3010 ($\epsilon_r = 10.2$) material with a diameter of 3.5 cm. Patch 1, connected to Feed1, is a circular patch antenna featuring a C-slot to miniaturize its size and is covered by a 0.508 mm thick superstrate. Patch 2, connected to Feed 2, is a ring antenna with the superstrate and also substrate 1 on top of it, resulting in a total of 1.778 mm thick superstrate.

The thicker superstrate in Patch 2 effectively reduces the electric field strength at the boundary between the superstrate and the skin. This reduction is visualized in Fig. 2.11, which illustrates the simulated electric field magnitudes for Feed1 and Feed2. Notably, Feed1 exhibits a higher electric field at the boundary, leading to greater power dissipation in the skin region and, consequently, a higher weighting factor for the skin layer. In contrast, Feed2 experiences reduced losses in the skin, enabling a higher weighting factor for the underlying muscle layer. This differentiation in electric field distribution demonstrates the effectiveness of the dual-feed design in achieving distinct sensing depths.

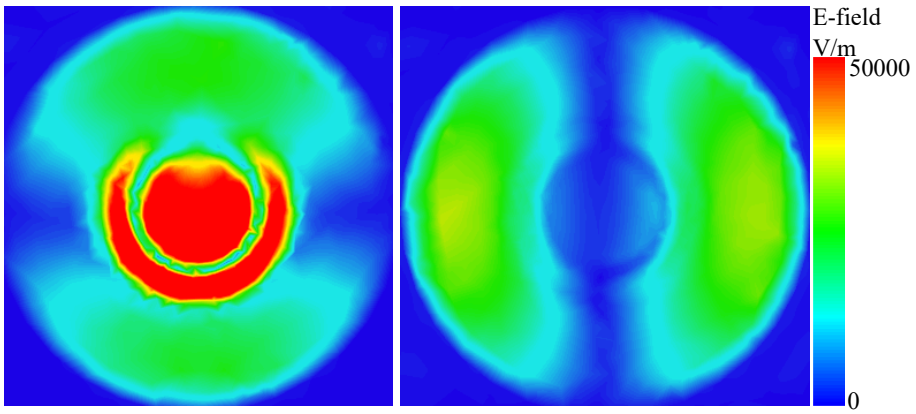


Figure 2.11: Simulated E-field magnitude at the boundary of the near-field antenna and skin phantom with 1 W on (a) Feed1 and (b) Feed2.

Figure 2.12 shows the simulated weighting factors as a function of distance from the superstrate-skin interface. The skin and muscle layers are sliced horizontally in the simulation into 0.5-mm thick layers, and the volume power density is integrated throughout each slice to calculate the corresponding weighting factors.

For Feed1 (depicted in black), the weighting factors are significantly larger in the skin layer compared to those of Feed2 (depicted in red). However, Feed2 demonstrates a higher weighting factor in the muscle layer due to its reduced power losses in the skin layer. The total weights used in Eqs. 2.3 and 2.4 are found by adding contributions of all slices, for both feeds. For Feed1, the weighting factors are $W_{s1} = 0.526$ and $W_{m1} = 0.474$, while for Feed2, the weighting factors are $W_{s2} = 0.403$ and $W_{m2} = 0.597$. These parameters are used in Chapter 5 to estimate the individual layer temperatures.

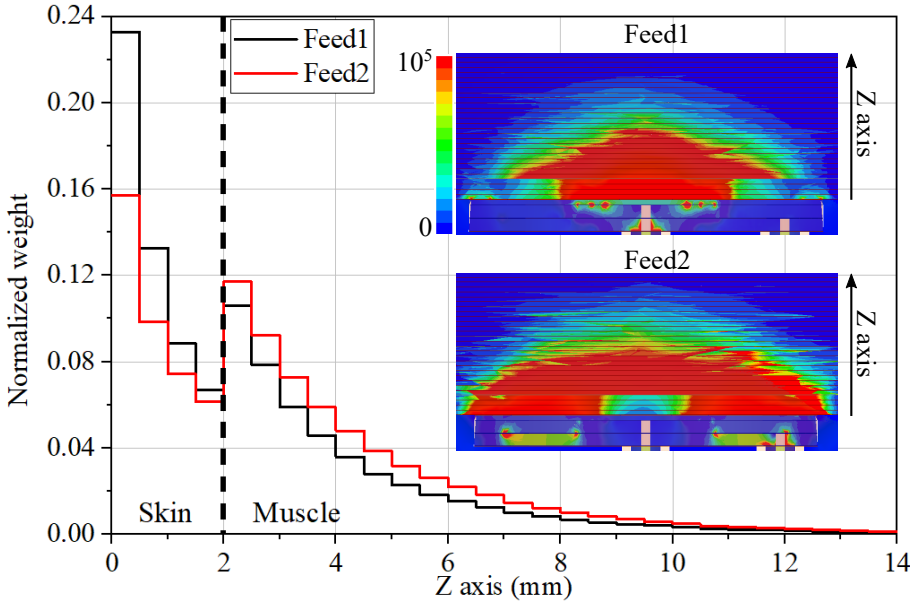


Figure 2.12: Simulated weighting factors as a function of distance from the superstrate-skin interface. The volume joule loss (W/m^3) is also shown when Feed1 and Feed2 is transmitting 1 W.

2.6 Conclusion

This chapter presents the design and analysis of near-field antennas for internal body temperature measurement, focusing on two configurations: a rectangular patch antenna and a slotted circular patch antenna. Both designs are optimized for operation at 1.4 GHz and demonstrate compatibility with tissue phantom stacks and human cheek tissues. The rectangular patch antenna, measuring 42 mm × 40 mm, provides high sensing coefficients from muscle layers. In contrast, the slotted circular patch antenna, with a diameter of 3.5 cm has improved RFI shielding through metal sidewalls.

These antennas have been recognized for their compact size. The rectangular patch antenna was highlighted in IEEE publications, including a conference paper at IMS 2023 [42] and extended research in IEEE TMTT 2024 [43]. The slotted circular patch antenna was presented at the IEEE MTT-S International Microwave Biomedical Conference (IMBioC 2024) [44], earning the Best Paper Award.

Chapter 3

MMIC Dicke Radiometer Design

Contents

3.1 Radiometer Theory **30**

3.2 SPDT Switch Design **34**

3.3 LNA Design **37**

3.4 Radiometer Measurements **41**

3.5 InGaAs Dicke Radiometer **47**

3.6 Conclusion **49**

3.1 Radiometer Theory

This section discusses key specifications for a radiometer and compares various radiometer architectures. A key metric for radiometer performance is the minimal detectable temperature difference, ΔT, which depends on the system noise temperature T_{sys}, measurement bandwidth B, and integration time τ. The value of T_{sys} is dominated by the first amplifying stage and the components preceding it. In this work, the measurement bandwidth is limited by the SAW filter, with a 1 dB bandwidth of 45 MHz. The integration time used in this work is 5 s and 2 s. Radiometer architectures, shown in Fig. 3.1, can be evaluated based on ΔT, allowing for tradeoff analysis to meet the needs of different applications. For the simplest total power radiometer, which consists of an LNA, filter, and a detector [45], the temperature resolution, or sensitivity, is expressed as:

$$\Delta T = \frac{T_{\text{sys}}}{\sqrt{\tau B}} \ , \tag{3.1}$$

The total power radiometer is highly susceptible to drift and fluctuations caused by factors such as inconsistent operating voltage, temperature changes, and environmental vibrations. These drifts cannot be calibrated during operation for the total power radiometer. Since the radiometer includes multiple amplifiers to achieve high gain, even small changes in gain can result in significant errors in temperature measurement. Therefore, a method to calibrate and compensate for these fluctuations is essential.

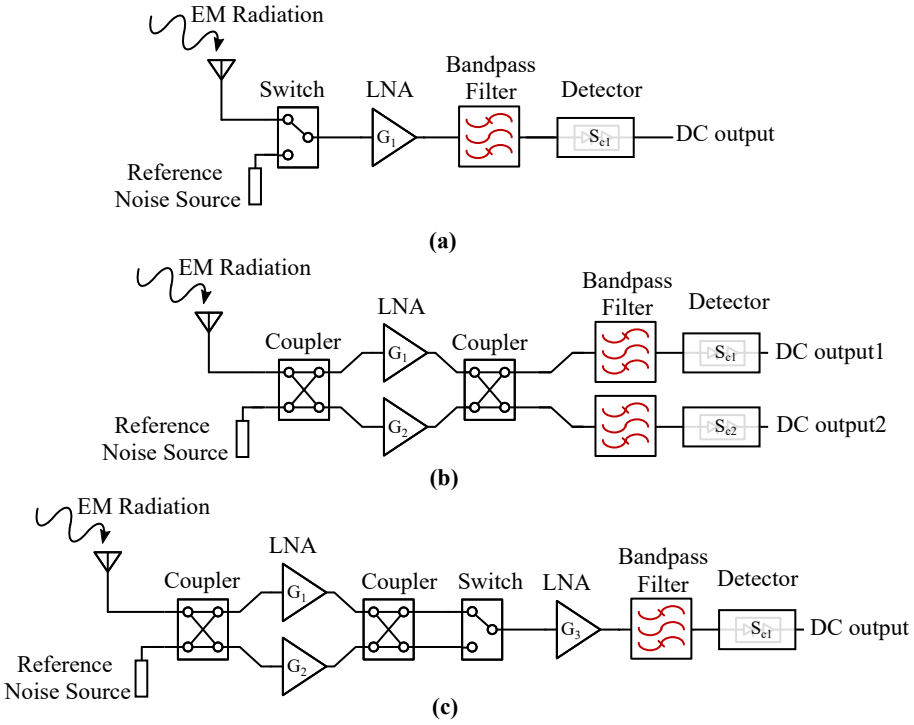


Figure 3.1: Diagrams of different radiometer architectures: (a) Dicke; (b) correlation; and (c) hybrid radiometers.

Other radiometer architectures which do allow for gain fluctuation calibration, include the Dicke radiometer, correlation radiometer, and a combination of the two, which we refer to as the "hybrid radiometer". A Dicke radiometer includes a switch after the antenna, allowing for calibration of gain fluctuations of all components that follow. This is performed by comparing the measurement

Table 3.1: Comparison of radiometer architectures

	Dicke [7]	**Correlation [46]**	**Hybrid [47]**
ΔT	$2T_{sys}/\sqrt{\tau B}$	$\sqrt{2}T_{sys}/\sqrt{\tau B}$	$2T_{sys}/\sqrt{\tau B}$
Pros	– Gain fluctuation calibrated	– No switch loss (but coupler loss) –100% duty cycle	– No switch loss (but coupler loss) – Gain flucturation calibrated
Cons	– Sensitive to input impedance – Limited time on target	– Duplicate components – Sensitive to phase balance	– Duplicate components – Limited time on target

to a known thermal reference. However, the switching reduces the effective measurement time due to the commonly used 50% duty cycle, which reduces the total received power from the target by 50% [45]. Additionally, the switch introduces losses, which increase T_{sys}.

The correlation radiometer has a balanced hybrid coupler with two low-noise gain paths, with the advantage of continuous measurement of both the target and reference. Additionally, the coupler makes this design less sensitive to impedance mismatches at the inputs since the output noise signal is only affected by the reflection of the source input and independent from the phase [48]. However, this structure remains sensitive to gain fluctuations in the detector stage due to the two separate paths. For the hybrid radiometer topology [47], the switch is placed after the hybrid couplers. This architecture is robust to load impedance variations and reduces the impact of gain fluctuations by positioning the switch before the components that follow it. Besides reducing the overall uncertainty, the hybrid radiometer is ideally balanced, meaning the voltage difference between outputs is zero. This will be delt more in detail in the next chapter. This balance, which will be discussed in more detail in the next chapter, further minimizes uncertainty by reducing the flicker noise contribution from components preceding the switch. Table 3.1 shows a summary of the achievable ΔT, as well as the *pros* and *cons* of various architectures. In this chapter, we show an implementation of a Dicke architecture, chosen due to its simplicity and the fact that human temperature changes on a scale much slower than the required switching period.

Fig. 4.7 shows a block diagram of the Dicke radiometer configuration. A near-field antenna is designed to effectively receive black-body radiation from a buried tissue layer. It couples the total

radiometric power received from all tissue layers to a switch that alternates between the tissue stack and a known noise reference. This allows calibration for gain fluctuations that are slow-varying compared to the switching speed.

The system's LNA gain is selected to meet a gain budget and is followed by broadband and narrowband bandpass filters. The detector converts the amplified thermal noise input to a dc voltage. The voltage amplitude resolution of the ADC, in this case, the oscilloscope, is $\Delta V = k\Delta T \cdot BRG = 0.8\,\mu$V, where k is the Boltzmann constant, ΔT is the temperature resolution, B is frequency bandwidth, R is detector responsivity, and G is the RF gain. The goal of the radiometer is to achieve a temperature resolution of 0.1 K. The calculation shows that the product BRG, which represents the responsivity of the entire radiometer, should be greater than $5.8\text{x}10^{17}$ V/W. Assuming the detector has a responsivity in the order of 10^3 V/W, and that the radiometer bandwidth is limited by the bandpass filter with a bandwidth of 45 MHz, the minimum required RF gain is 46 dB.

The design of the GaAs MMIC which includes a single-pole double-throw (SPDT) switch and 3-stage LNA, is described here. Both switch and LNA are implemented in the 110 nm PIH1-10 WIN Semiconductors GaAs process, known for its low noise and high-gain characteristics, as well as its single-polarity bias requirement. The components are first characterized separately, and then integrated on a single chip.

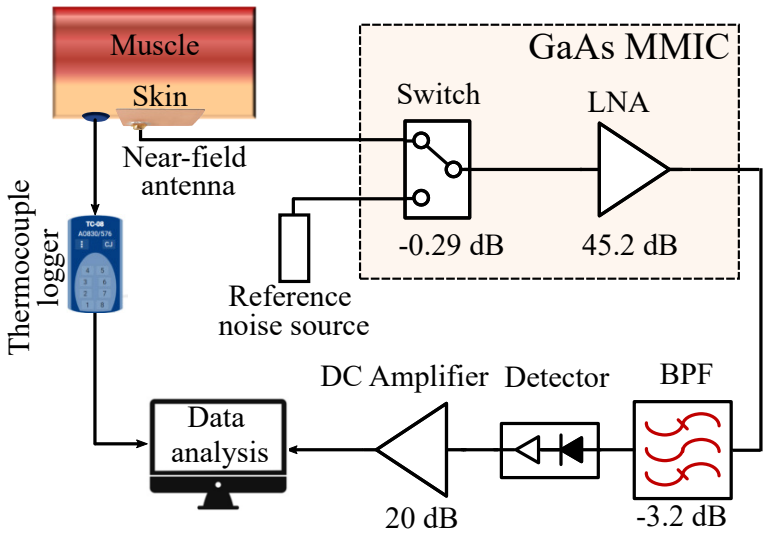


Figure 3.2: Block diagram of a Dicke radiometer connected to a phantom tissue stack of skin and muscle. The Dicke switch and LNA are implemented on a GaAs MMIC and followed by off-chip band-pass filter, detector, and dc amplifier. The output is digitized and processed for temperature retrieval. A thermocouple logger monitors skin temperature.

3.2 SPDT Switch Design

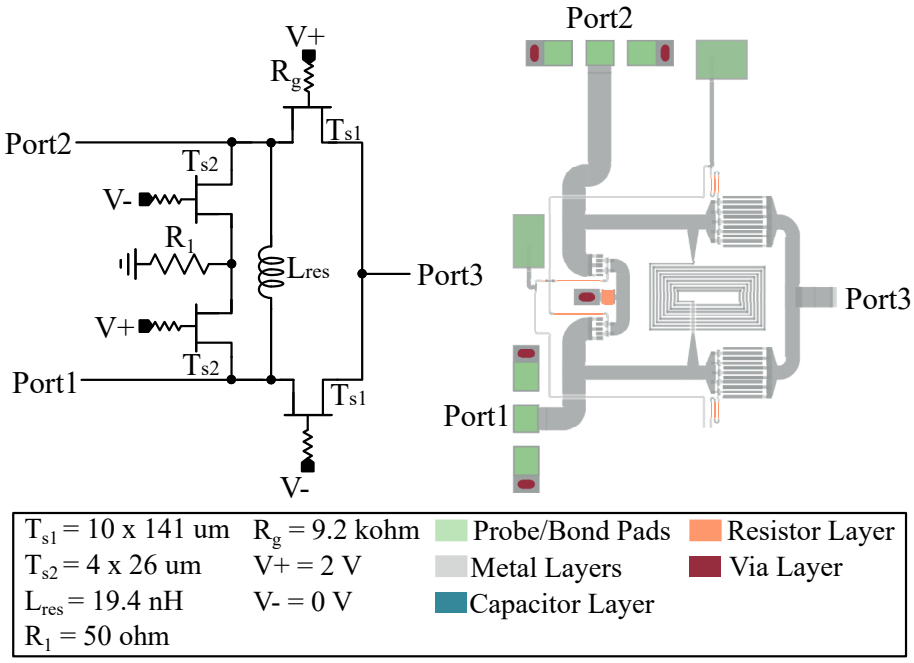


Figure 3.3: Circuit schematic (left) and layout (right) of the SPDT switch. Parameter values and the main metal, via, pad, capacitor, and resistor layers are shown. Several process layers are removed for clarity.

An SPDT switch is the first component of a Dicke radiometer, which alternates between two inputs for calibration. The insertion loss of the switch is crucial, as it directly contributes to the radiometer's total noise figure, affecting overall system sensitivity. The isolation should exceed 30 dB to ensure that the noise power corresponding to less than 0.3 K from the reference load at 300 K leaks into the near-field antenna port. Additionally, the return loss should exceed 10 dB to limit the signal-to-noise ratio (SNR) reduction to less than 10% during power transfer to the LNA. SNR is the ratio of the wanted power to the noise power. If the return loss is 10 dB, the noise power stays the same, however, the wanted power decrease by 10%.

Fig. 3.3 illustrates the circuit schematic, layout, and parameter values of an absorptive SPDT switch selected for this design. The SPDT switch uses a shunt-series topology for high isolation. The transistors are turned *on* and *off* by biasing the gate to 2 V and 0 V. R_1 is a 50 Ω resistor seen at the *off* port when T_{s2} is *on*. This reduces the reflection coming in from the *off* port. The inductor between the shunt and series transistors is used to create a resonance with the parasitic capacitance of the *off* transistors, improving the insertion loss and isolation of the switch. The *off* capacitors of T_{s1} and T_{s2} are 0.7 pF and 0.06 pF, respectively. An inductor L_{res} is used to create resonance with these two capacitors. The resonating inductor also biases all the nodes in the switch, avoiding extra loss and voltage drop from biasing resistors.

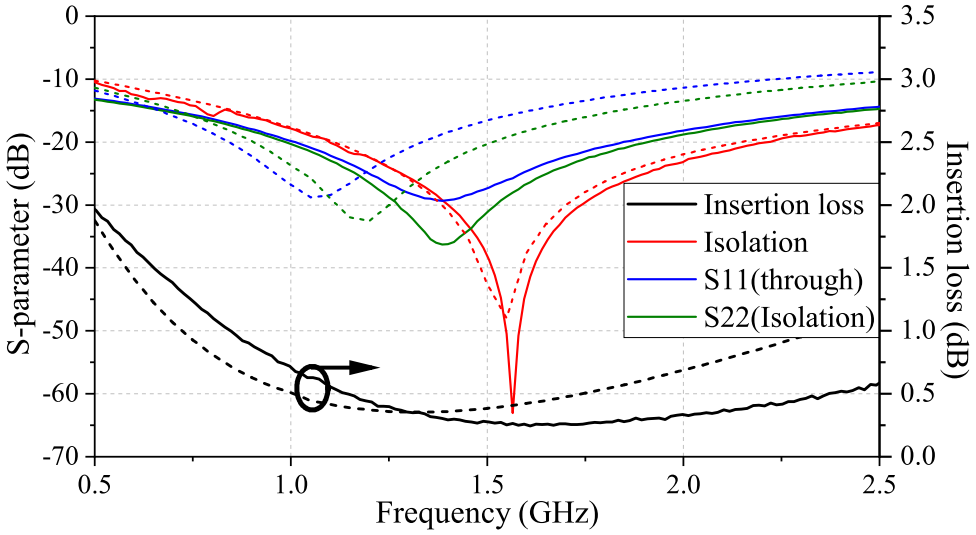
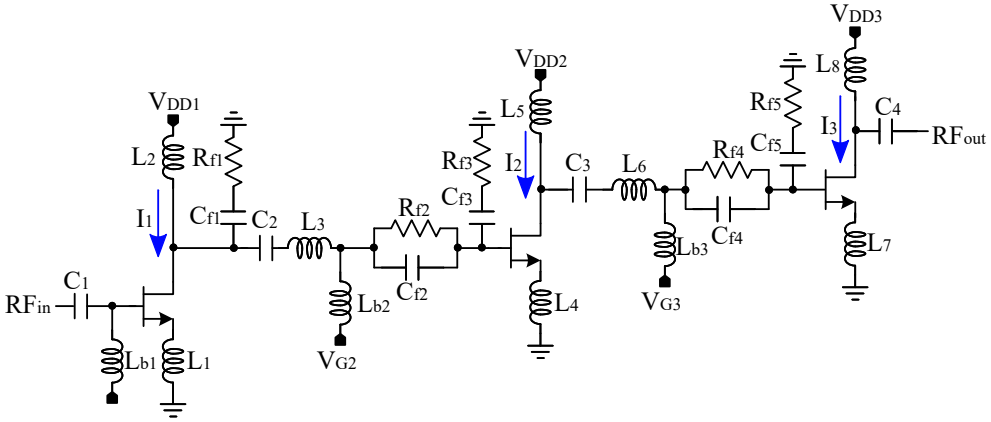


Figure 3.4: Measured (solid line) and simulated (dashed line) performance of the MMIC SPDT switch.

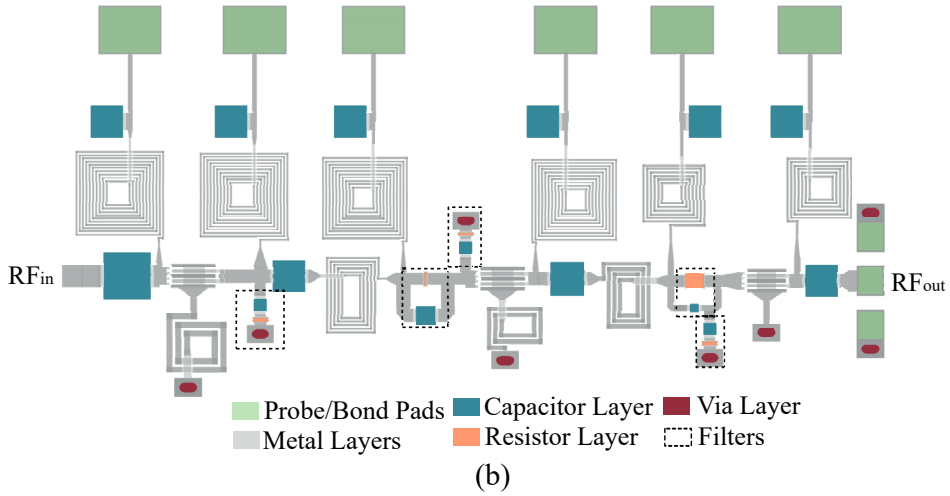
Fig. 3.4 presents both the measured and simulated performance of the MMIC SPDT switch. The minimum insertion loss is 0.24 dB at 1.61 GHz, and the maximum isolation is 63 dB at 1.58 GHz. At the design frequency of 1.4 GHz, the insertion loss is 0.29 dB and the isolation is 30.8 dB. A slight frequency shift is shown for the return loss due to an impedance mismatch of the load termination during the measurement. The compact dimensions of the switch are 0.9 mm×0.9 mm, making it suitable for integration within the overall radiometer.

3.3 LNA Design



M_1=4 x 164 um	L_{b1}=21.6 nH	L_1=0.95 nH	L_5=21 nH	C_1=8 pF	$V_{DD1,2,3}$=2 V	I_1=16.4 mA
M_2=4 x 180 um	L_{b2}=21 nH	L_2=20 nH	L_6=1.2 nH	C_2=4 pF	V_{G1}=0.49 V	I_2=12.2 mA
M_3=4 x 132 um	L_{b3}=6.2 nH	L_3=4.7 nH	L_7=0.2 nH	C_3=5 pF	V_{G2}=0.47 V	I_3=13.6 mA
		L_4=1.3 nH	L_8=6.5 nH	C_4=1.5 pF	V_{G3}=0.48 V	

(a)



(b)

Figure 3.5: (a) Circuit schematic and component values for the 3-stage LNA integrated into a GaAs MMIC. The element values and bias points are shown in the table. Five distributed filters are used as matching and stability networks. (b) Layout of the chip, where the various layers are shown with different colors.

For an LNA with more than 45 dB of gain at 1.4 GHz, a 3-stage common-source topology is chosen for its high-gain and low-noise characteristics [49]. Fig. 3.5(a) shows the circuit schematic, including circuit component values, and bias points, with layout in Fig. 3.5(b).

The design of the first stage is crucial for an LNA since it is dominant in determining the

noise figure of the cascade. For wideband applications, a common-gate structure is often used, providing an approximate input impedance of $1/g_m$, where g_m is the small-signal transconductance. The common-source topology is used for a high-gain and low-noise LNA because it can achieve simultaneous gain and noise matching. For the first stage, a device size of 4 x 164 um and a current density of 25 mA/mm is chosen for the lowest minimum noise figure (NF_{min}). The difference in impedance between optimum noise matching and conjugate matching is crucial in an LNA design. A source degeneration (feedback) inductor (L_1) is used to shift the optimum noise matching to a point closer to the input impedance, allowing simultaneous noise and impedance matching [50]. A low-loss input matching network is needed since the input matching network has a crucial effect on the overall NF.

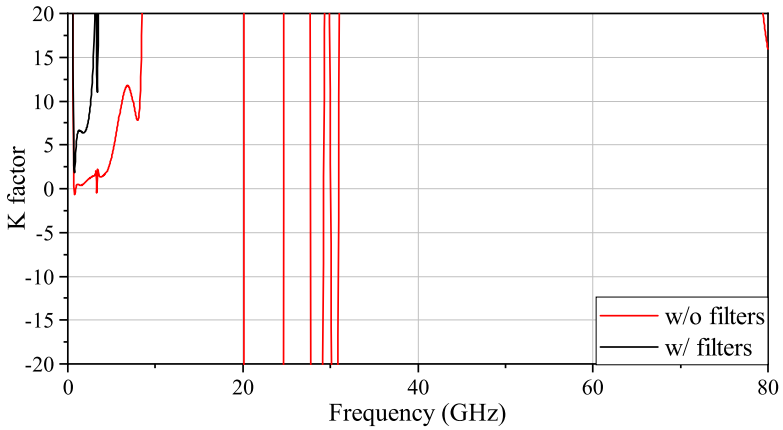


Figure 3.6: Simulated K factor comparison w/ and w/o filters. K> 1 for frequencies up to 80 GHz when filters are included.

The stability of an LNA is crucial since the LNA is multi-stage with > 45 dB gain. Several techniques improve the stability, including the use of a source degeneration inductor as a feedback technique [51] and the use of an *RC* shunt filter at the output to avoid negative resistance [52]. The LNA design achieves stability using source degeneration and five *RC* filters that operate as an inter-stage matching network. For multiple-stage LNAs, multiple filters are needed to ensure stability in all stages. For multiple-stage LNAs, multiple filters are needed to ensure stability in all stages. The distribution of the filters allows improved stability with minimal degradation in NF.

Stability is verified up to 80 GHz due to the high cutoff frequency of the PIH110 GaAs process. Fig. 3.6 shows the K factor of the LNA with and without the filters. Without the filters the K factor drops below 1 at 0.69-2.26 GHz, 20.1-24.6 GHz, and 27.7-31 GHz. Including all filters, K>1 in all frequency up to 80 GHz with a minimum of 1.83 at 0.75 GHz. A filter is not placed before the first transistor to avoid NF degradation. The filter's positions within the circuit provide minimal NF degradation of 0.02 dB at 1.4 GHz while stabilizing the LNA, according to simulation.

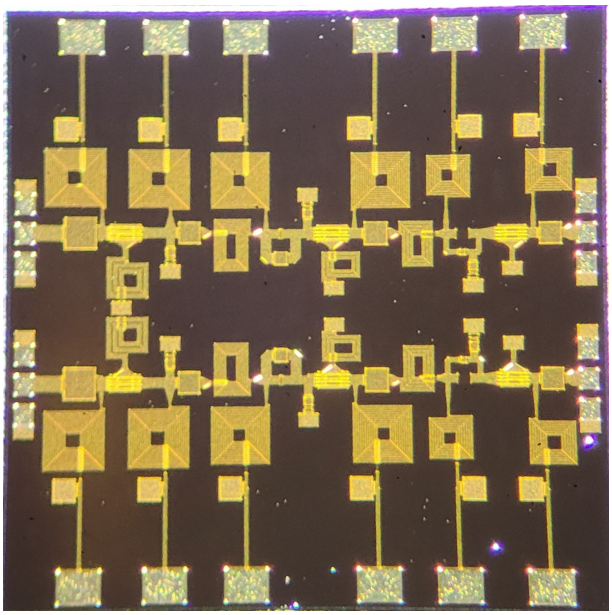
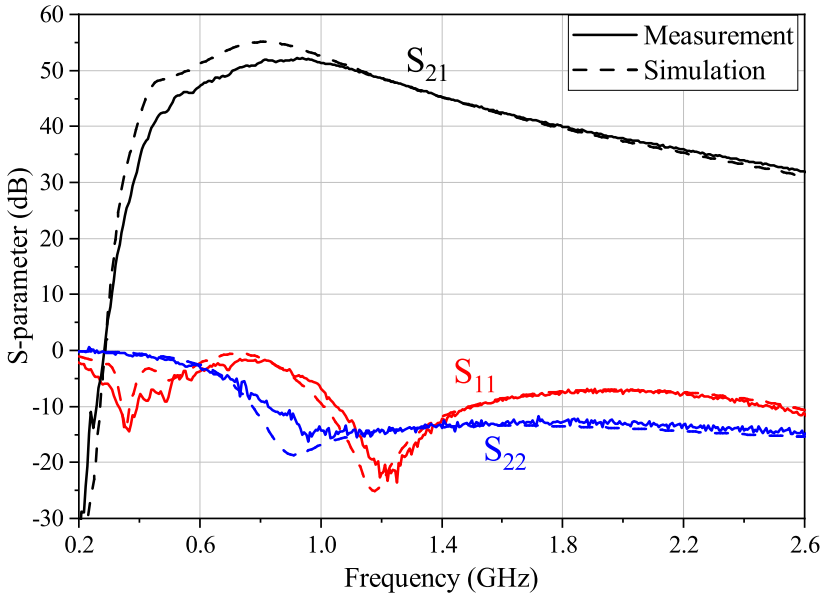
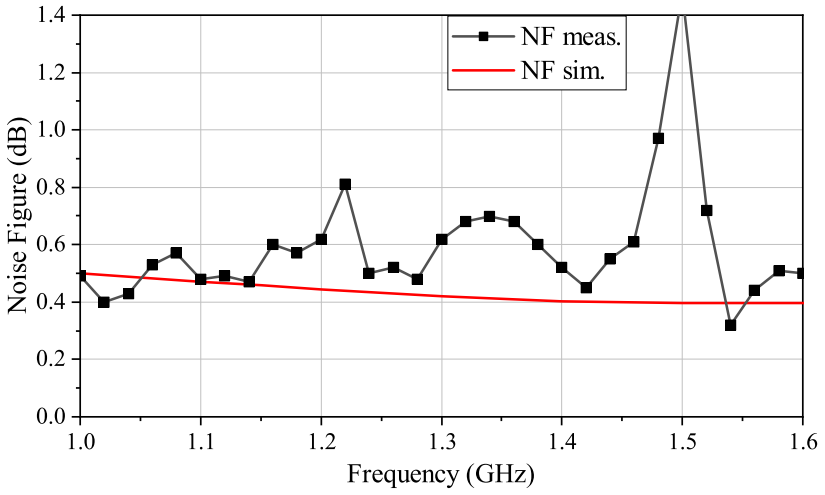


Figure 3.7: Chip photograph of the fabricated two LNAs, 3 mm × 3 mm in size.

Fig. 3.7 shows a photograph of the two-in-one chip LNAs fabricated using the 0.1 um pHEMT GaAs process. The size of the two-LNA die for 1.4 GHz operation is 3 mm × 3 mm and size of one LNA excluding the pads and unnecessary routings is 2.6 mm × 1 mm. Two LNAs are placed side-by-side in a single for integration into a correlation radiometer circuit as shown in Fig. 3.1(b)(c).



(a)



(b)

Figure 3.8: Measured and simulated (a) S-parameters and (b) NF.

Fig. 3.8a shows the LNA's S-parameter measurement and simulation results. A probe-tipe SOlT calibration is performed to the GSG probe reference planes. The peak gain is 52.3 dB at 0.94 GHz and the gain at 1.4 GHz is 45.2 dB. The measured reflection coefficients show that $|S_{11}| <$ -10 dB for 1.05-1.5 GHz, 2.45-3.7 GHz and $|S_{22}| <$ -10 dB for 0.83-3.3 GHz. Fig. 3.8b shows the measured and simulated NF. The NF is measured using a Keysight 8970B noise figure meter with a 346B noise source. The minimum NF is 0.35 dB at 1.54 GHz and at 1.4 GHz, the measured

Table 3.2: Performance Comparison of GaAs L-band LNAs

	This work	[53] EuMC '15	[54] RFIT '18	[55] MMS '18
Process	0.1 um GaAs	0.15 um GaAs	0.15 um GaAs	0.25 um GaAs
Frequency [GHz]	1.05-1.5	1.6-3.1	1.5-3.7	0.1-10
Gain [dB]	45.2	30.5	31.8	20
NF [dB]	0.52	0.65	0.73	1.4
P_{dc} [mW]	84.4	54.5	25	450

value is 0.52 dB. The measurement of the NF is about 0.12 dB higher than the simulation results. According to the high-frequency PIH110 process handbook, there is no NF data available in the model below 2 GHz in which the interpolation is used, and is a possible source of discrepancy between measurement and simulation.

Table 3.2 shows a comparison of L-band GaAs LNAs. Although some LNAs built with discrete InP transistors [56] achieve similar gains and lower noise figures, this work demonstrates the highest gain compared to other demonstrated GaAs MMICs with comparable power consumption, representing an optimal balance between gain, noise figure, and power efficiency.

3.4 Radiometer Measurements

Both the SPDT switch and LNA are integrated onto a single GaAs MMIC with a die size of 3.75 mm × 1.7 mm, as shown in Fig. 3.9. For characterization purposes, biasing, and convenient connections, the MMIC is packaged on a 45 mm×45 mm printed circuit board (PCB) on a 0.254 mm thick Rogers 4350B substrate.

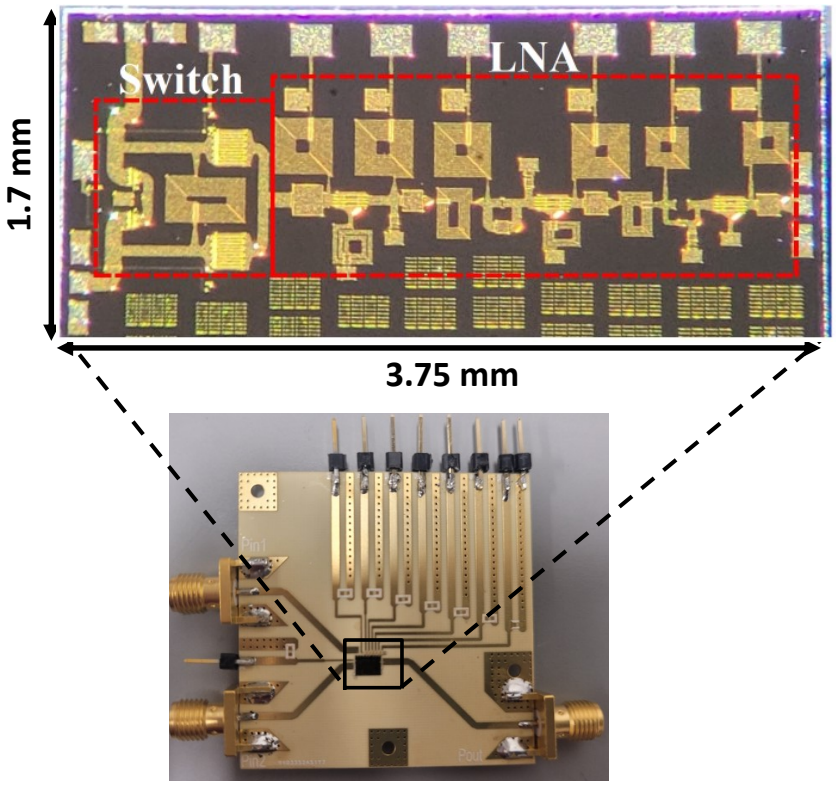


Figure 3.9: Photograph of the GaAs MMIC SPDT switch and a 3-stage LNA. The total chip dimensions are 3.75 mm × 1.7 mm.

Fig. 3.10 shows the S-parameter measurements of the packaged LNA together with the SPDT switch. The gain of the *through* ports (from *on* switch input to LNA output) at 1.4 GHz is 45.1 dB, and the gain through the isolation port (from *off* switch input to LNA output) is 15.5 dB. The return loss at 1.4 GHz is above 10 dB at all ports, indicating effective impedance matching. The resonance at 0.8 GHz is due to the biasing structure involving a 0.2 nH inductor and a 100 pF shunt capacitor. To verify stability, the measured and simulated K factors are illustrated in Fig. 3.11. The measured and simulated noise figure of the *through* port is shown in Fig. 3.12 and at 1.4 GHz, $\mathrm{NF}_{\mathrm{rad}} = 0.88\,\mathrm{dB}$.

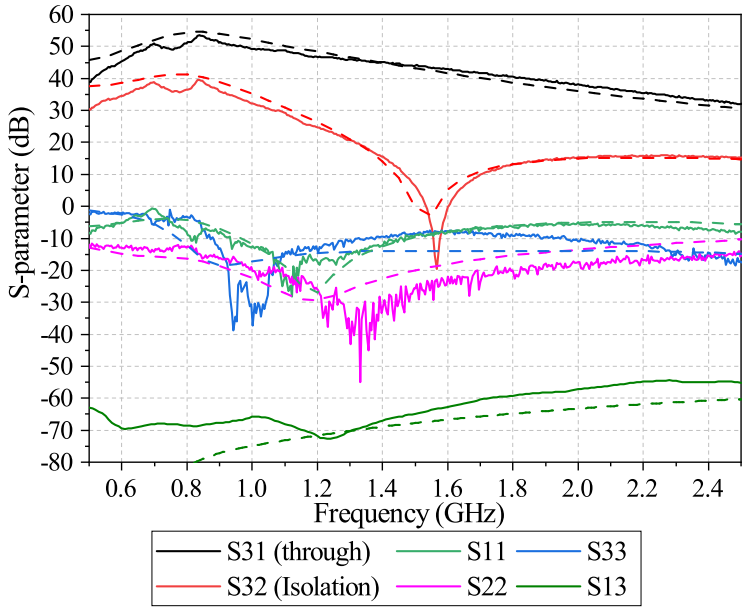


Figure 3.10: Measured (solid line) and simulated (dashed line) S-parameter magnitudes of the packaged SPDT switch and LNA MMIC portion of the Dicke radiometer. A coaxial calibration is performed to the connector reference planes.

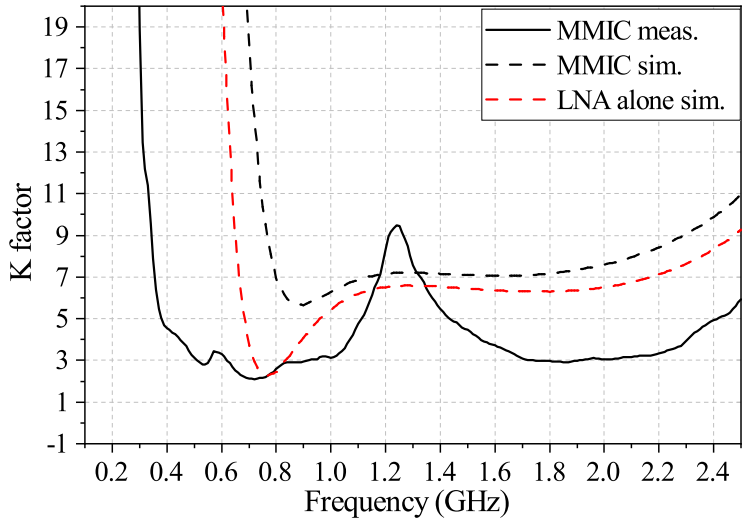


Figure 3.11: Measured and simulated stability K factor of the MMIC (LNA with switch), as well as simulated LNA K factor. The measured K factor of the LNA alone is not calculated since the reverse isolation was below the noise floor in the S-parameter measurement.

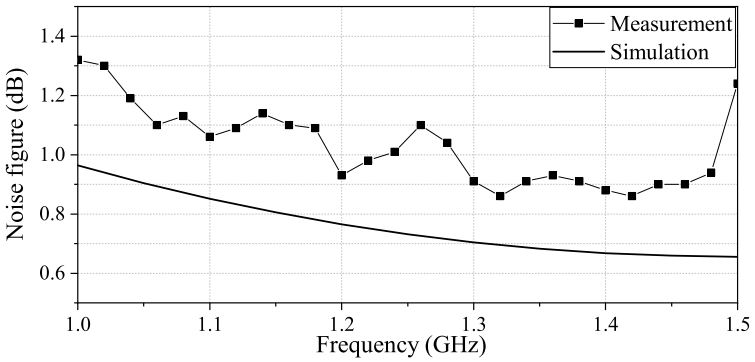


Figure 3.12: Measured and simulated noise figure of the packaged SPDT switch and LNA MMIC front end of the Dicke radiometer.

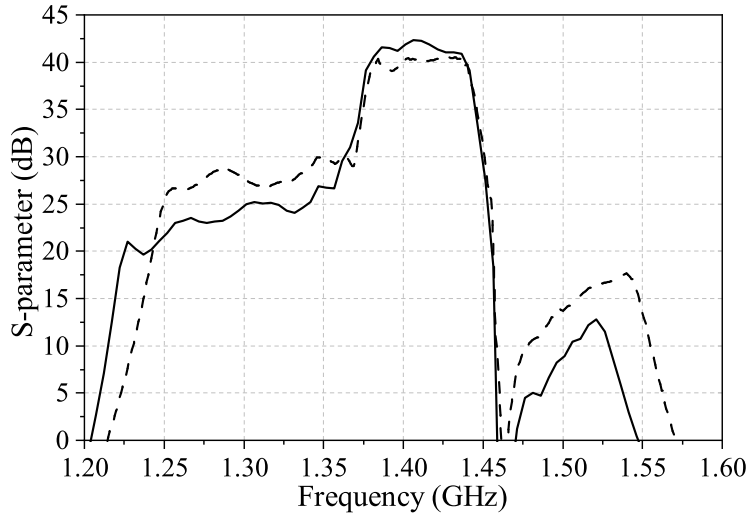


Figure 3.13: Measured (solid line) and simulated (dashed line) gain from the input of the *on* switch of the packaged MMIC to the output of the off-the-shelf bandpass filters. The gain has a 3-dB bandwidth of 64 MHz from 1.38 to 1.44 GHz.

To limit the received noise power bandwidth and minimize out-of-band interference, two off-chip band-pass filters are connected to the output of the packaged MMIC, as shown in Fig. 4.7. The first band-pass filter[57] has a bandwidth of 160 MHz from 1.32 GHz to 1.48 GHz and an out-of-band rejection of 32–41 dB from dc to 2.4 GHz. The second band-pass filter is a SAW filter that has a narrower bandwidth of 64 MHz from 1.38 GHz to 1.44 GHz[58]. Including the filter loss, the gain at 1.4 GHz is reduced to 41.9 dB and the gain across frequency near the operating band is shown in Fig. 3.13. The 3-dB bandwidth of the radiometer is about 63 MHz from 1.377 to 1.44 GH, wider

than the targeted 27 MHz bandwidth.

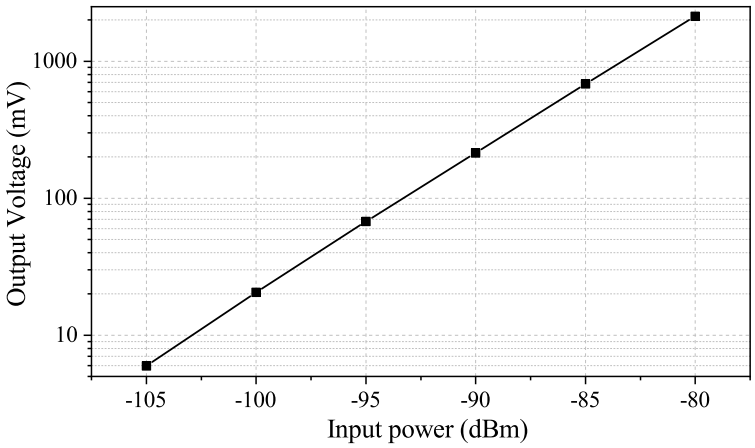


Figure 3.14: Measured voltage responsivity of the radiometer from the through port to the output of the dc amplifier. The responsivity is 213 GV/W at 1.4 GHz.

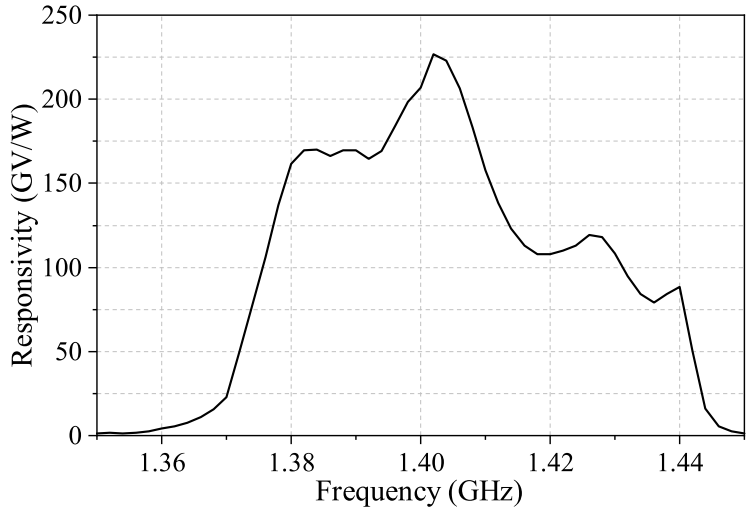


Figure 3.15: Measured frequency response of the entire Dicke radiometer responsivity when the input switch is *on*.

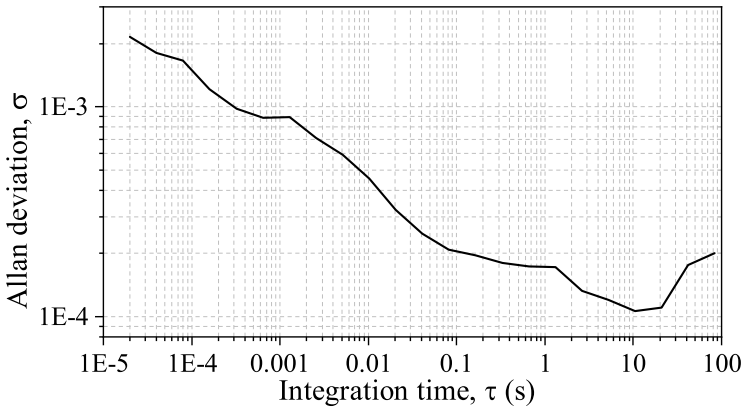


Figure 3.16: The Allan deviation of the Dicke radiometer to 100 sec integration time, obtained from measured data. A minimum in the Allan deviation is observed at an integration time of approximately 10 seconds, with a value on the order of $1.06 \cdot 10^{-4}$. In this work, an integration time of $\tau = 2\,\mathrm{s}$ is used, with a corresponding Allan deviation of $1.7 \cdot 10^{-4}$.

Since the integration time (τ in Eq. (3.1)) can be extended due to the relatively slow timescale of thermal measurements, bandwidth reduction is pursued to minimize interference. Narrowband matching of the detector is used to reduce the radiometer bandwidth from 62 MHz to 60 MHz. The detector is designed with the Skyworks SMS7630-079 diode, integrated with a matching circuit consisting of a $\lambda/4$ resonator and shunt capacitors. This configuration effectively matches the diode's impedance over a frequency range centered at 1.412 GHz with a bandwidth of approximately 60 MHz [29]. The rectified dc voltage from the detector is amplified through a post-detection amplification stage, featuring a voltage gain of 100. This amplification is integrated into the identical board of the detector. The dc amplifier operates within a 5 V voltage range while consuming a current of under 1 mA.

Fig. 4.13b shows the responsivity of the radiometer from the input *through* port to the output of the dc post-amplification stage. The measurement is done with a sinusoidal signal at 1.4 GHz at the input to the radiometer. The voltage responsivity of the full radiometer at 1.4 GHz is 213 GV/W, assuming a 1 MΩ dc load and a 50 Ω input impedance. The measured voltage responsivity at the output of the detector for an RF input signal at the switch port when the switch is *on* is shown in Fig. 3.15, and is a function of frequency over the operating bandwidth.

The system gain directly impacts sensitivity, constrained by the oscilloscope resolution limit.

The oscilloscope (DSOX1102G) used in this setup has a voltage amplitude resolution of 3.14 μV. The corresponding temperature resolution ΔT is calculated as $\Delta T = \Delta V/(kBR(f)) = 0.0226\,\mathrm{K}$, where k is the Boltzmann constant, $B = 100\,\mathrm{MHz}$ is the measurement bandwidth and $R(f)$ is the frequency-dependent full receiver detector voltage responsivity in V/W. This calculation does not take into account any input noise, therefore the uncertainty from the oscilloscope resolution is 0.0226 K and this reduces the sensitivity of the radiometer.

The impact of the LNA and switch noise figure on radiometer sensitivity can be estimated based on the measured noise figure, gain, and detector responsivity. The 0.88 dB noise figure of the front-end translates to a noise temperature $T_A = 65.1\,\mathrm{K}$. The corresponding increase in detected voltage due to this noise is found by integrating the responsivity of the radiometer (including the detector, filter, etc.) across the operating bandwidth from 1.35 to 1.45 GHz. This results in $\Delta V = kT_ABR = 9\,\mathrm{mV}$. The Allan deviation of the output voltage of the radiometer is shown in Fig. 3.16 , presents the noise stability over integration times ranging from 10 μs to 100 sec, providing insight into measurement precision over time.

3.5 InGaAs Dicke Radiometer

A Dicke radiometer is designed with a switch positioned after the antenna, followed by an LNA, filtering, detection, and dc amplification stages, which allows sampling of the output signal. The circuit schematic of a switch and a 3-stage LNA implemented in the 0.18 μm InGaAs enhancement-mode and depletion-mode HEMT WIN Semiconductors PQH-0P process is shown in Fig. 3.17.

The single-pole triple-throw (SP3T) switch adopts a shunt-series topology to achieve high isolation, which is crucial for minimizing signal leakage between paths. To further optimize the design, an inverter circuit is incorporated using logic devices within each path of the switch. This approach reduces the number of required bias pads. The insertion loss of the switch is 0.4 dB and isolation is 35.2 dB at 1.4 GHz.

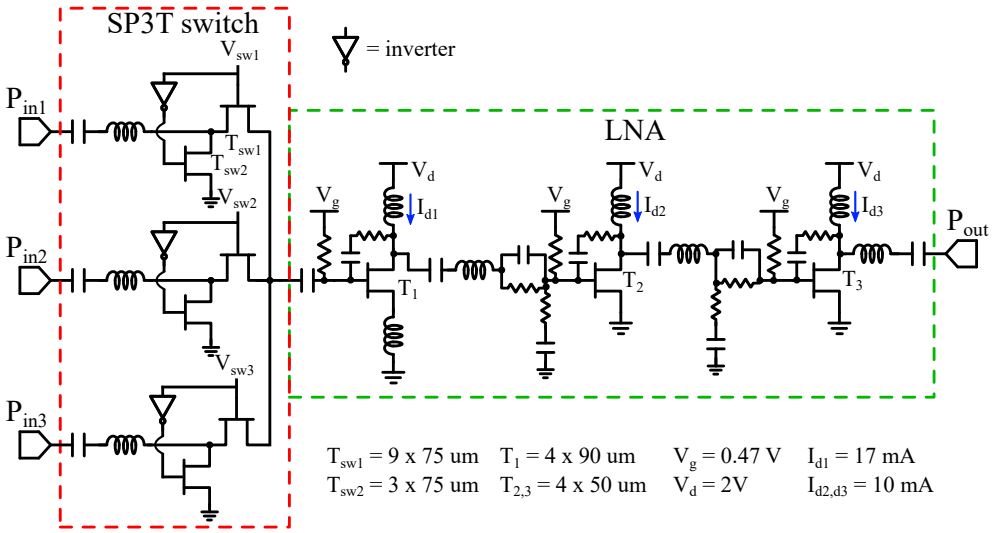


Figure 3.17: Circuit schematic for the Dicke radiometer with a SP3T switch and a 3-stage LNA. Transistor sizes, biasing voltages, and dc currents are shown in the figure. Stability is ensured through RC feedback in each stage, as well as low-pass and high-pass filters at the gates, and verified through Nyquist simulations.

A 3-stage LNA is designed to achieve >45 dB gain at 1.4 GHz. To meet the requirements for high-gain and low NF, a common-gate configuration was adopted. This configuration effectively minimizes the noise figure while providing significant gain, making it well-suited for sensitive applications like radiometry. The MMIC implementation of the LNA, which includes the SP3T switch, is shown in Fig. 3.18. The MMIC measures a compact 3 mm×1.1 mm. Compared to other on-chip radiometers with comparable gain, the size is very compact.

Fig. 3.19 shows the *S*-parameter and NF measurements of the LNA together with the SP3T switch. The gain of the through ports at 1.4 GHz is 45.2 dB. The isolation, defined as the signal attenuation between input and output when the switch is in the "off" state, is measured at 15.5,dB. The NF of the through port is 1.26 dB at the same frequency, which is a critical parameter for ensuring high sensitivity in radiometer applications. To reduce out-of-band interference, an off-chip band-pass filter is connected at the output of the MMIC. When accounting for the insertion loss introduced by the filter, the overall gain of the system is reduced to41.9 dB.

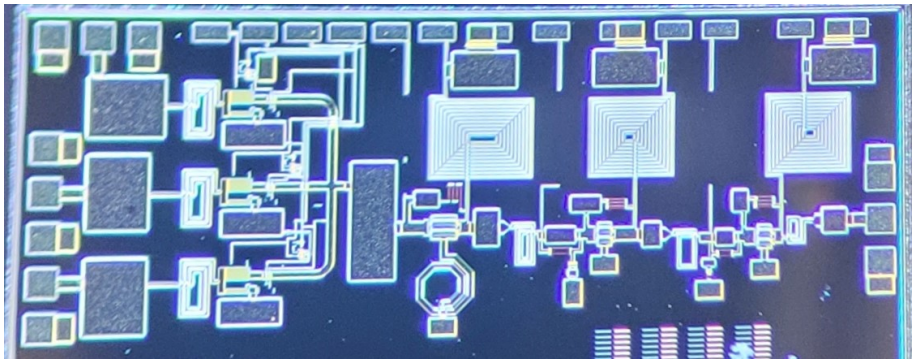


Figure 3.18: Photograph of SP3T switch and LNA for a Dicke radiometer. The size of the MMIC is 3 mm × 1.1 mm.

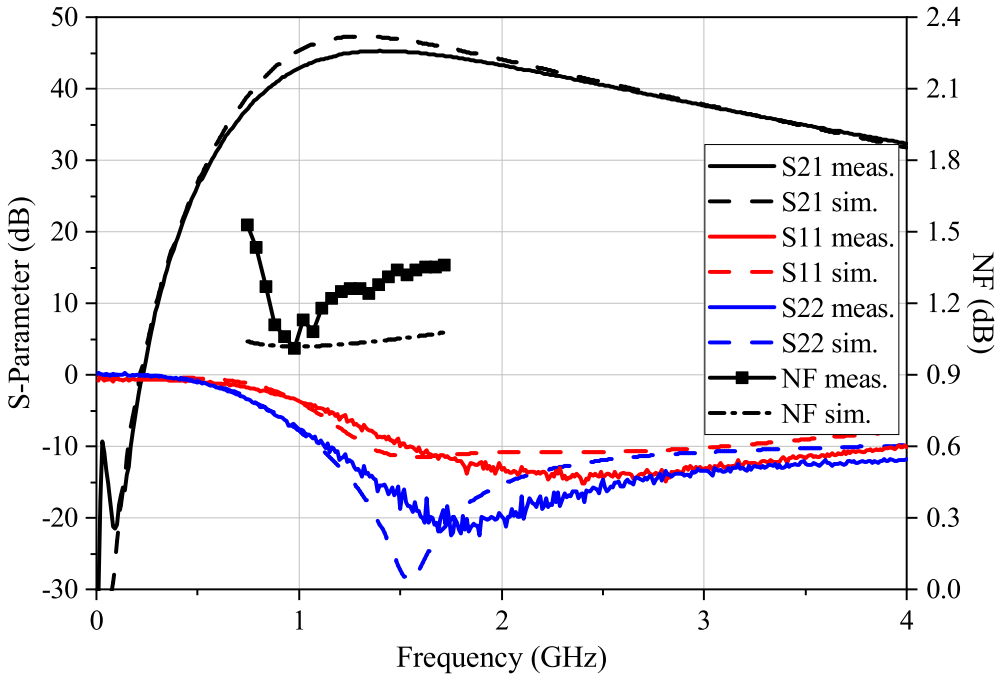


Figure 3.19: Measured and simulated S-parameter magnitudes and noise figure of the SP3T switch and LNA MMIC for a Dicke radiometer.

3.6 Conclusion

In conclusion, this chapter details the design and implementation of a MMIC Dicke radiometer for non-invasive internal body temperature measurement. By integrating an SPDT switch and a high-performance LNA into a compact and power-efficient MMIC design, this radiometer achieves a balance between high sensitivity, low power consumption, and compact size. The switch and LNA

were designed using advanced GaAs and InGaAs processes, known for their low-noise characteristic. The compact design not only simplifies integration into radiometric systems but also makes it a viable solution for portable and wearable devices.

This work was the first on-chip radiometer for internal body temperature measurement at the time of publication at IMS 2023 [42] and extended research in IEEE TMTT 2024 [43]. The 3-stage LNA is published at IEEE RWS 2023 [59].

Chapter 4

Hybrid Correlation-Dicke Radiometer

Contents

4.1 Hybrid Radiometer Architecture **51**

4.2 PCB Design **53**

4.3 MMIC Design **58**

4.3.1 Lumped-Element Hybrid Coupler 60

4.3.2 LNA and SPDT Switch 62

4.3.3 Radiometer Implementation 63

4.4 Conclusion **66**

This chapter begins with an analysis of the "hybrid" radiometer architecture, which combines the benefits of a correlation and a Dicke radiometer. Initially, this architecture is implemented on a printed circuit board (PCB) with off-the-shelf components. After validation, parts of the hybrid radiometer, up to the filter, are implemented in a GaAs MMIC for further miniaturization.

4.1 Hybrid Radiometer Architecture

The radiometer architectures were briefly introduced in the previous chapter. In this section a hybrid design that combines elements of both correlation and Dicke radiometers is explored in greater detail. This hybrid approach offers the advantage of reduced sensitivity to load impedance variations, while the switch minimizes sensitivity to gain fluctuations in the components that follow the switch.

The operation of the hybrid radiometer is outlined below, with reference to the ports shown in Fig. 4.1. We assume that the random processes $n_k(t),\ k = 1, \ldots, 6$ are Gaussian-distributed noise signals with zero mean, and band-limited to the observation (measurement) bandwidth Δf. The mean power received from the NFA is $\langle |n_1(t)|^2 \rangle = kT\Delta f$, where k is the Boltzmann constant, and T is the target temperature in K. The reference load is at temperature T_R, so that it delivers a power $\langle |n_2(t)|^2 \rangle = kT_R\Delta f$. When biased separately, the amplifiers LNA1 and LNA2 add effective uncorrelated zero-mean Gaussian noise with power $\langle |n_{3,4}(t)|^2 \rangle = kT_{3,4}\Delta f$ referenced to the LNA input.

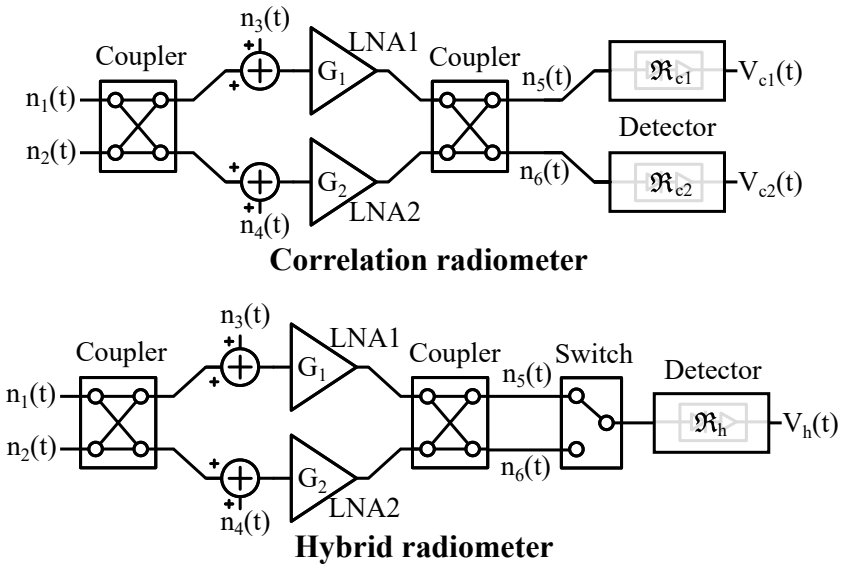


Figure 4.1: Block diagrams of correlation and hybrid radiometers, showing noise sources $n_i(t)$.

To show the robustness of the hybrid radiometer against gain fluctuations, The unit LNAs (LNA1,LNA2) have asymmetric gains $G_1 = G_o + \Delta G_c$ and $G_2 = G_1 + G_d$, where G_o is the mean value, and ΔG_c and ΔG_d are common and differential gain fluctuations, respectively. The average noise temperatures at the output of the second coupler are $\langle |n_{5,6}(t)|^2 \rangle / (k\Delta f) = \frac{1}{4}T_{2,1}(\sqrt{G_1} + \sqrt{G_2})^2 + \frac{1}{2}G_1T_3 + \frac{1}{2}G_2T_4$.

In the hybrid radiometer, the noise powers are detected after the switch with a single detector, with a voltage responsivity $\Re_h = \Re_o + \Delta\Re_c$ that fluctuates. For a correlation radiometer, these powers are received by separate detectors having common and differential responsivity fluctuations,

$\mathfrak{R}_{c1} = \mathfrak{R}_o + \Delta\mathfrak{R}_c$ and $\mathfrak{R}_{c2} = \mathfrak{R}_{c1} + \Delta\mathfrak{R}_d$. The temperature of the target can be estimated from the measured post-detection voltage difference $\Delta V = V_2 - V_1$ as $T^{\text{est}} = \Delta V/(kG_o\mathfrak{R}_o\Delta f) + T_R$. Considering only the effects of gain fluctuations and ignoring higher-order terms, the temperature estimated by the correlation radiometer is $T^{\text{est}} = T + \Delta T$. The uncertainty ΔT can be shown to have the form:

$$\begin{aligned}\Delta T = &\left[\left(\frac{\Delta G_c}{G_o} + \frac{\Delta G_d}{2G_o}\right)\left(1 + \frac{\Delta\mathfrak{R}_c}{\mathfrak{R}_o}\right) + \frac{\Delta\mathfrak{R}_c}{\mathfrak{R}_o}\right](T - T_R) \\ &+ \frac{\Delta\mathfrak{R}_d}{\mathfrak{R}_o}\left(1 + \frac{\Delta G_c}{G_o} + \frac{\Delta G_d}{2G_o}\right)T \\ &+ \frac{\Delta\mathfrak{R}_d}{2\mathfrak{R}_o}\left[T_3\left(1 + \frac{\Delta G_c}{G_o}\right) + T_4\left(1 + \frac{\Delta G_d}{G_o}\right)\right].\end{aligned} \tag{4.1}$$

Therefore, the gain and responsivity fluctuations originating from flicker noise increase the uncertainty of the estimation [29]. More importantly, that uncertainty does not vanish for a perfectly balanced correlation radiometer ($T = T_R$). One advantage of a hybrid architecture is that $\Delta\mathfrak{R}_d = 0$ because a single detector observes both outputs of the second hybrid coupler by switching faster than the responsivity fluctuations. Besides reducing the overall uncertainty, the hybrid radiometer can be balanced, becoming immune to flicker noise.

4.2 PCB Design

The hybrid radiometer is assembled with off-the-shelf (OTS) components, as listed in Table 4.1. The fabricated circuit, measuring 10 cm×6.7 cm, is shown in Fig. 4.2. It is built on a Rogers 3010 substrate with a thickness of 1.27 mm, selected for its high permittivity ($\epsilon_r = 10.2$) in order to reduce size.

Since the noise power received from the body is low compared to other ambient signals at radio frequencies, the radiometer is designed in the 1.4 GHz quiet band allocated to radioastronomy. As explained in chapter 3.1, an RF gain greater than 45 dB is required.

Table 4.1: Components in the designed radiometer.

Component	Manufacturer	Description
Hybrid coupler	Anaren	IL=0.3 dB
LNA1, LNA2	Qorvo	G=16.4 dB, NF= 0.4 dB
Switch	MACOM	IL=0.65 dB
LNA3	Mini-Circuits	G=35 dB, NF= 0.6 dB
BPF1	Mini-Circuits	IL=1.4 dB
BPF2	Tai-saw Tech.	IL=2 dB
Diode(detector)	Skyworks	SMS7621-079LF
DC amplifier	Diodes Inc.	G=100

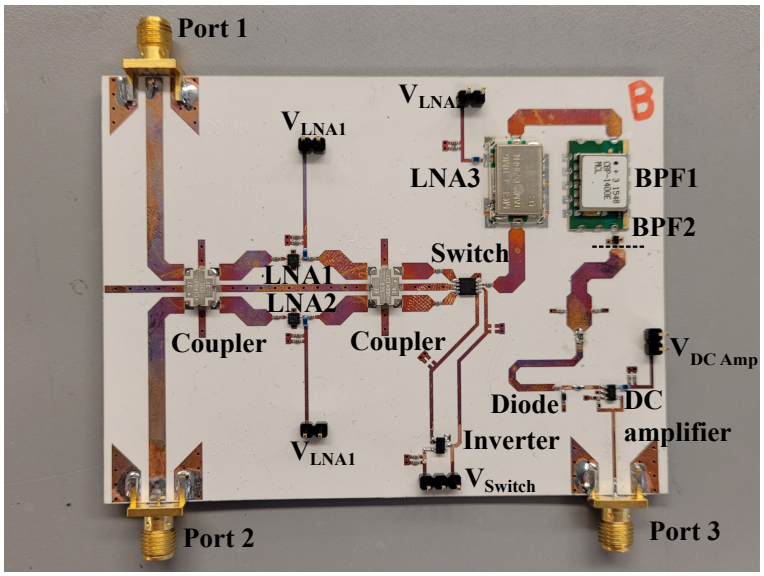


Figure 4.2: Photograph of the hybrid radiometer prototype. Off-the-shelf components are used on a 10 cm× 7.6 cm PCB.

The simulated 3-port S-parameters from the RF input ports 1 and 2 to the input of the detector, where the reference plane is shown as dashed line in Fig. 4.2 after BPF2, are shown in Fig. 4.3. The simulated gain from input to this reference is 45.5 dB, meeting the design specifications. The measured input reflection coefficients are also shown, with $|S_{11}| < -10$ dB from 0.95-1.7 GHz, indicating effective impedance matching across this band.

The detector was fabricated and characterized separately, with voltage responsivity shown in Fig. 4.4. It achieves an average responsivity of 4.1 x 10^3 V/W. The detector diode has an impedance of $Z_D = 27 - j812\,\Omega$, which is matched to the 50 Ω circuit. First, a high-impedance transmission

line moves a highly-capacitive impedance point to inductive. Then, two shunt SMD capacitors are used to move the inductive and low resistive impedance to 50 Ω. The matching optimizes power transfer and allow higher responsivity across the target frequency range.

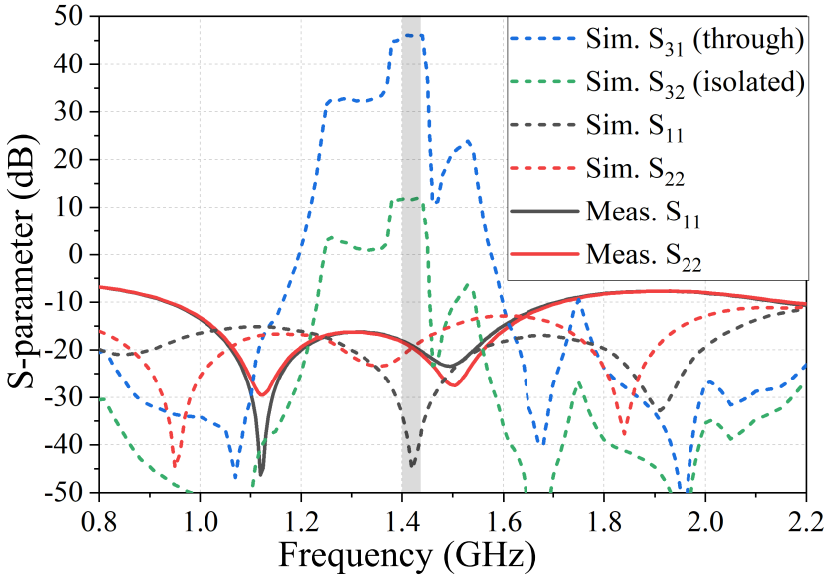


Figure 4.3: Simulated (dashed) and measured (solid) S-parameters of the radiometer prototype using components from Table 4.1. The shaded area indicates the design frequency band.

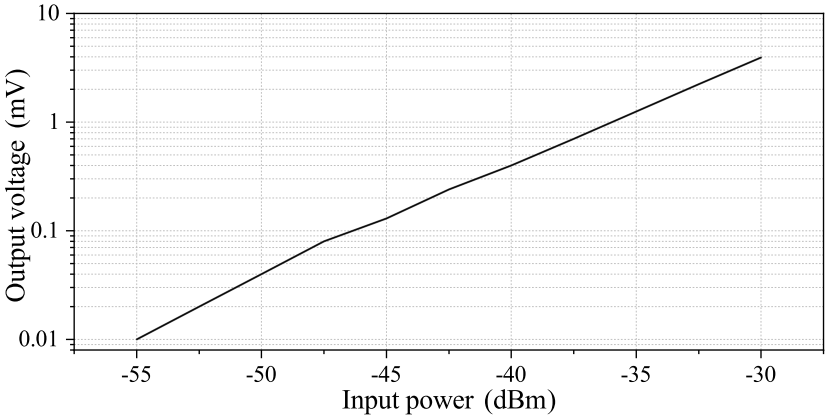


Figure 4.4: Measured voltage responsivity of the detector at 1.415 GHz.

The calibration and temperature measurement setup for the hybrid radiometer is illustrated in Fig. 4.5.

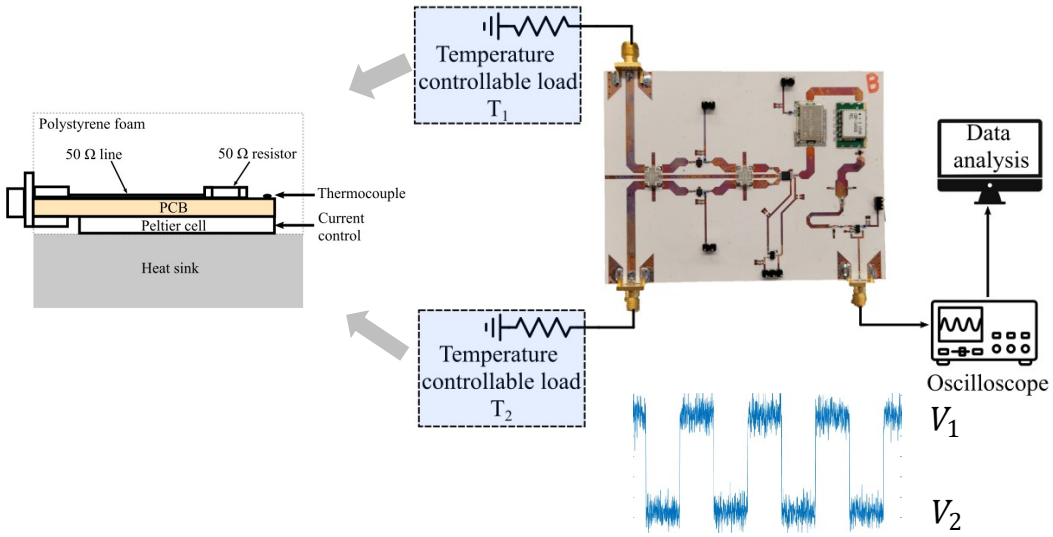


Figure 4.5: Measurement setup for temperature load testing. The design of the temperature controlled load using Peltier cell is shown. Two of these loads at temperature T_1 and T_2 are connected to the input of the radiometer and the dc output voltage of V_1 and V_2 are measured with an oscilloscope.

To calibrate the hybrid radiometer, two temperature controllable 50 Ω loads, set at temperatures T_1 and T_2 are connected to the input ports. Each load includes a chip resistor connected to a 50,Ω transmission line, mounted on a separate board. The circuit is attached to a Peltier thermoelectric cell, controlled by a ThorLabs MTD415T thermistor temperature controller, using thermally conductive tape, with the other side of the Peltier element connected to a heat sink. The structure is thermally isolated using polystyrene foam. Due to the imbalances from the hybrid couplers, amplifiers, and switch, the output voltages in the two switch states represent a linear combination of the inputs at ports 1 and 2, given by:

$$V_1 = \alpha_{11}T_1 + \alpha_{12}T_2 + \alpha_{13} \tag{4.2a}$$

$$V_2 = \alpha_{21}T_1 + \alpha_{22}T_2 + \alpha_{23}. \tag{4.2b}$$

Defining $\alpha_i = \alpha_{i1} - \alpha_{i2}$,

$$\Delta V = V_1 - V_2 = \alpha_1 T_1 + \alpha_2 T_2 + \alpha_3. \tag{4.3}$$

The constants α_i are determined by applying known temperature pairs of T_1 and T_2. While only three distinct pairs of T_1 and T_2 are theoretically required to solve for the three unknowns, 13 pairs of temperatures are used in the experiment to minimize errors and improve accuracy. The values of α_i are then calculated through linear fitting.

Two different estimation methods for determining temperature T_1 are next compared. Method 1 uses the measurement of ΔV at the output of the post-detector amplifier to directly estimate the temperature as:

$$T_1^{\text{est}} = \frac{\Delta V}{\alpha_1} + \frac{\alpha_2}{\alpha_1} T_2 + \frac{\alpha_3}{\alpha_1}. \tag{4.4}$$

Method 2 dynamically adjusts the reference temperature T_2 so that $\Delta V \approx 0$. This reduces (4.4) to:

$$T_1^{\text{est}} = \frac{\alpha_2}{\alpha_1} T_2 + \frac{\alpha_3}{\alpha_1} \tag{4.5}$$

Method 2 reduces the error caused by the gain fluctuation of the components. Quantities α_i vary proportionally to gain fluctuations, so their ratio remains constant [7].

Radiometric temperature measurements are performed to compare the two methods. The temperature controlled load at Port 1 is set to temperatures 15° – 33°C. Fig 4.6 shows the estimated temperature and the error. ΔV is an average value integrated over 5 seconds to reduce radiometric uncertainty. The average errors using Method 1 and Method 2 are 0.386 °C and 0.773 °C. In Method 2, the temperature control algorithm for T_2 and the limit to the temperature control resolution causes overshoot and residual error in ΔV. Improvement in the algorithm is needed to make $\Delta V \approx 0$ for Method 2 to have lower error.

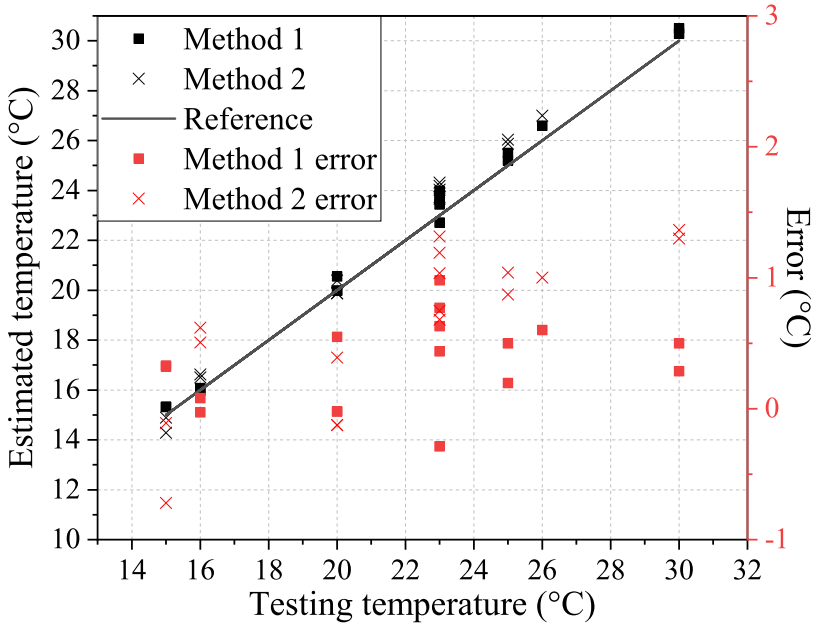


Figure 4.6: Measured temperature estimated from two calibration methods, measured on two different days, with and integration time of 5 seconds.

4.3 MMIC Design

For further miniaturization, the hybrid radiometer is implemented on a GaAs MMIC. Fig. 4.7 is a block diagram of a hybrid Dicke-correlation radiometer. The architecture comprises a 3-dB coupler, two LNAs, another 3-dB coupler, and a switch. The system's NF is primarily determined by the coupler insertion loss and the NF of the LNAs. Previous works have achieved > 45 dB gain levels using multiple cascaded off-the-shelf LNAs [7] and a 3-stage LNA after a Dicke switch [43]. In this work, the 45 dB gain is accomplished using two MMIC chips, both fabricated using WIN Semiconductor's PIH1-10 process. This process features enhancement-mode (E-mode) pHEMT devices with a threshold voltage (Vt) of 0.3 V and cutoff frequency ft=100 GHz, making it well-suited for high-frequency, low-noise applications.

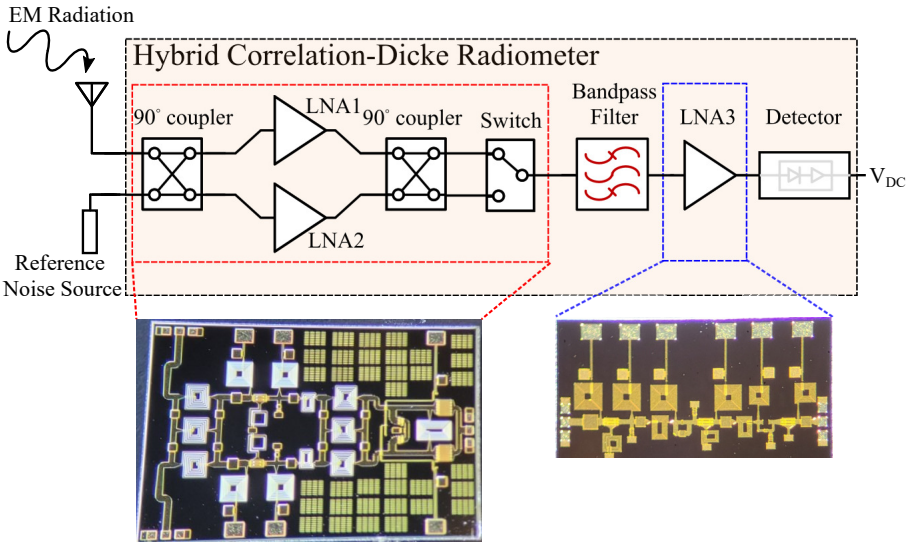


Figure 4.7: Block diagram of the correlation-Dicke hybrid radiometer for internal tissue thermometry.

All circuit components from the input coupler to the output of the switch are integrated on a single GaAs MMIC with size 3.8 mm x 2.4 mm. Fig. 4.8 displays the circuit schematic and the layout of these elements. This configuration allows the radiometer to switch between measuring two different thermal noises, a combination of the thermal noise from the tissue and a known reference. The switching frequency of 10 Hz is high enough to calibrate for the gain fluctuation of the components after the switch. The MMIC output is followed by filtering and additional amplification prior to detection. Detailed descriptions of each component are provided in the following subchapters.

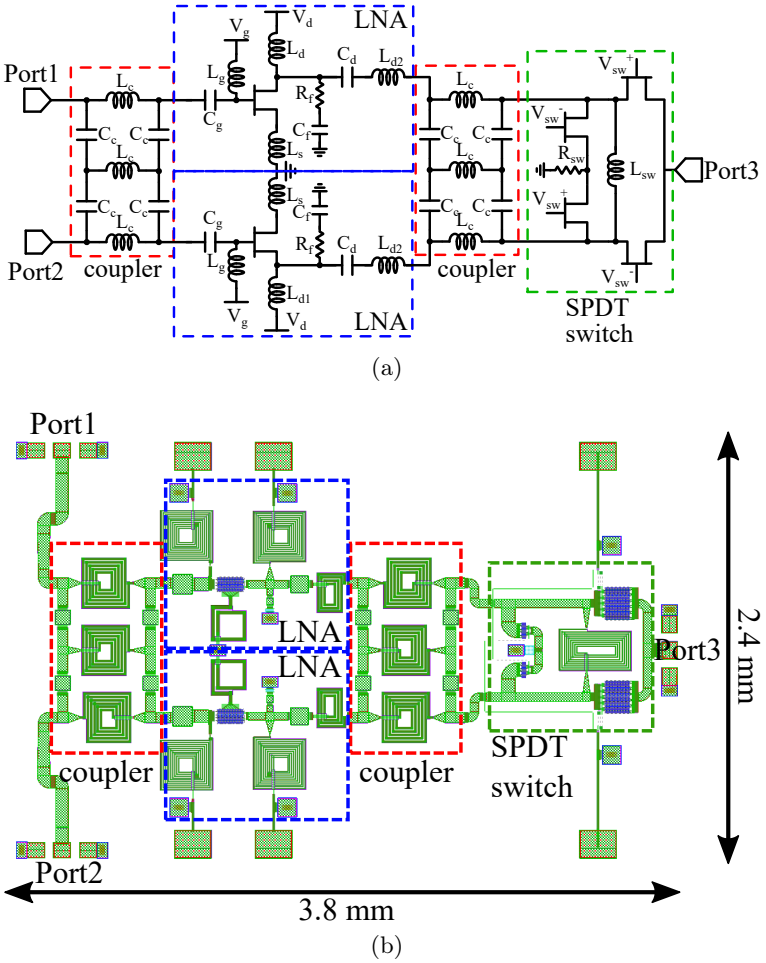


Figure 4.8: (a) Schematic and (b) layout of MMIC with two hybrid couplers, one-stage LNA in each path, and an SPDT switch.

4.3.1 Lumped-Element Hybrid Coupler

At lower microwave frequencies, transmission-line branch-line couplers while $\lambda/4$ lines can be prohibitively long for MMIC implementation. To reduce the size, couplers can be designed using lumped element approximations of $\lambda/4$ lines [60]. The lumped element model of the hybrid coupler is characterized by equations involving inductance (L_c) and capacitance (C_c) based on characteristic impedance(Z_0) for a π model of a $\lambda/4$ line and frequency (f). The inductance and capacitance are given by:

$$L_c = Z_0/(2\pi f) \quad \text{and} \quad C_c = 1/(Z_0 2\pi f). \tag{4.6}$$

Initial values for the inductors and capacitors are calculated using these equations and then fine-tuned through electromagnetic (EM) simulations. Fig. 4.10 shows the simulated S-parameter magnitude and phase performance of the coupler. Without EM simulations, the frequency of operation is 1.22 GHz. After conducting EM simulations, the final coupler design achieved a 3.7 dB loss from the input port to the output and coupled port with only 0.02 dB loss imbalance between the two at 1.4 GHz and the maximum imbalance at the operation frequency of 1.37-1.45 GHz is 0.34 dB. The phase difference between the output port and the coupled port is 89.7°, showing only 0.3° imbalance at 1.4ĠHz and the maximum imbalance at the operation frequency is 1°.

The compact design of the coupler, measuring 1.05 mm x 0.6 mm, is significantly smaller than a traditional branch-line hybrid coupler, which would require $\lambda/4 = 14.8$ mm for a transmission line on a GaAs wafer ($\epsilon_r = 13.1$) at 1.4 GHz. This compact design allows for the integration of the coupler into the MMIC hybrid radiometer architecture, significantly reducing the overall footprint of the MMIC.

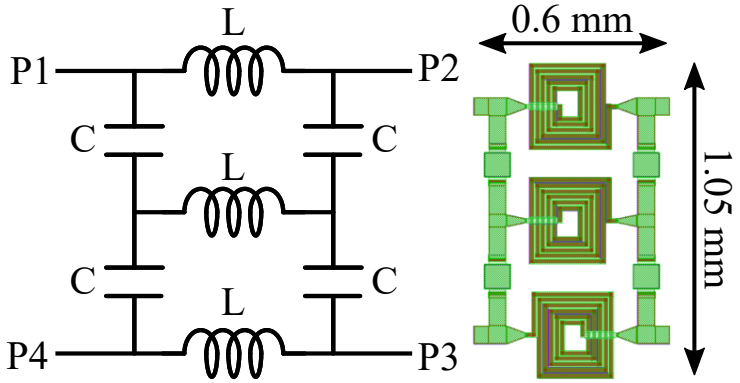


Figure 4.9: (a) Schematic of lumped-element on-chip hybrid coupler (b) Layout of hybrid coupler.

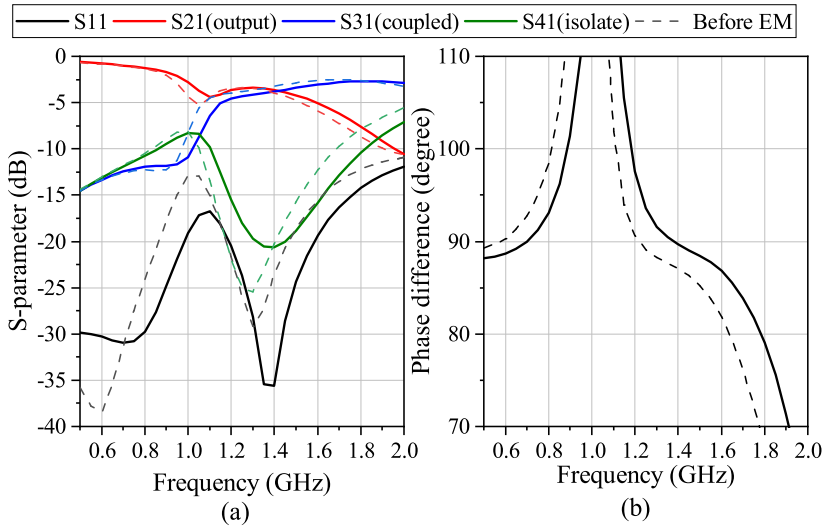


Figure 4.10: (a) S-parameter magnitude and (b) phase difference of S21 and S31 of the hybrid coupler. The coupler performance with PDK components is shown in dashed lines, and the performance with EM simulation is shown in solid lines.

4.3.2 LNA and SPDT Switch

Following the first coupler, a single-stage common-source LNA is implemented. The device size of 4 x 164 μm and a current density of 13 mA/mm are chosen as a compromise between the lowest minimum noise figure (NF_{min}), input impedance, and power consumption. The LNA features a degenerative inductor (L_s=0.7 nH) at the source of the transistor, allowing for simultaneous gain and noise matching. A shunt RC network, consisting of R_f and C_f at the drain of the transistor, acts as a low-pass filter to improve the stability of the LNA. The gain of the LNA is 15.5 dB at 1.4 GHz and the simulated noise figure is 0.43 dB. After the LNA, another lumped element coupler is placed, followed by the second coupler, an SPDT, described in Chapter 3.

The measured and simulated performance of the first MMIC, from Fig. 4.8 is shown in Fig. 4.11. The peak gain is 13.44 dB at 1.4 GHz. The measured $|S_{11}|$ is less than -10 dB for 0.7-1.73 GHz, and $|S_{22}|$ is less than -10 dB for dc–1.63 GHz. The minimum measured NF is 1.31 dB at 1.36 GHz and NF=1.41 dB at 1.4 GHz. The measurement of the NF is approximately 0.19 dB higher than the simulation results, likely due to model limitations of the high-frequency process at these low frequencies.

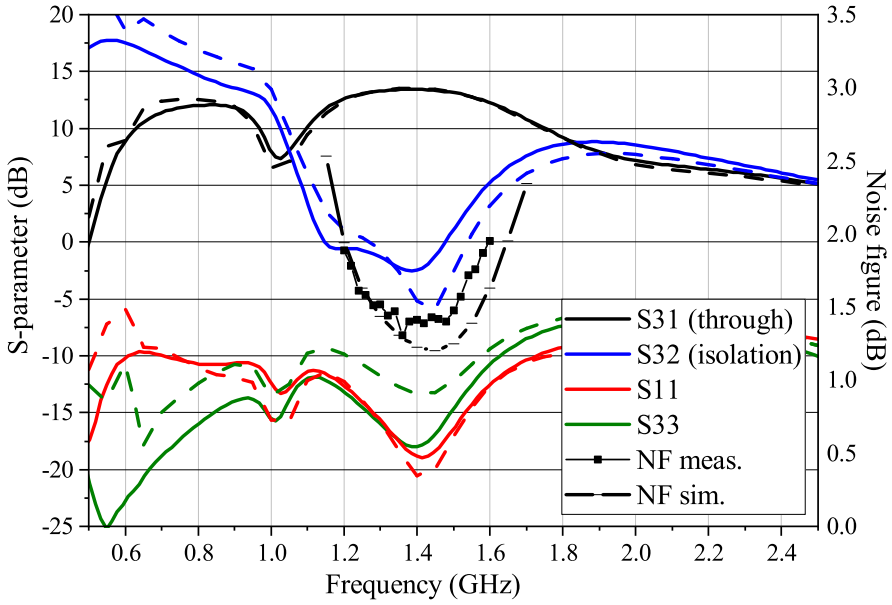


Figure 4.11: Measured (solid line) and simulated (dashed line) S-parameter magnitude and noise figure of the MMIC hybrid radiometer.

4.3.3 Radiometer Implementation

Following the MMIC described in the previous subsection, a narrowband bandpass filter and an additional LNA, providing approximately 35 dB of gain [49], are interconnected on a 20 mil Rogers 4350b PCB, as shown in Fig. 4.12. The S-parameters of the packaged RF components of the radiometer are illustrated in Fig.4.13a. The radiometer shows 49 dB of gain in the through path and about 32dB at S32, which is a 17 dB gain difference.

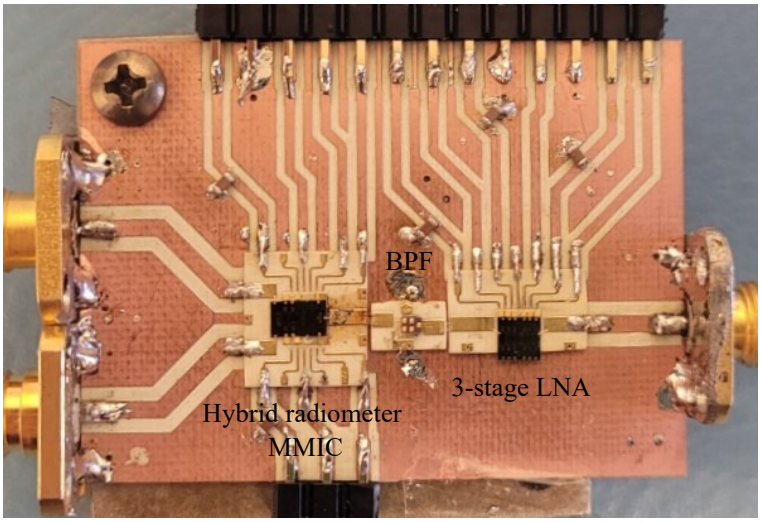
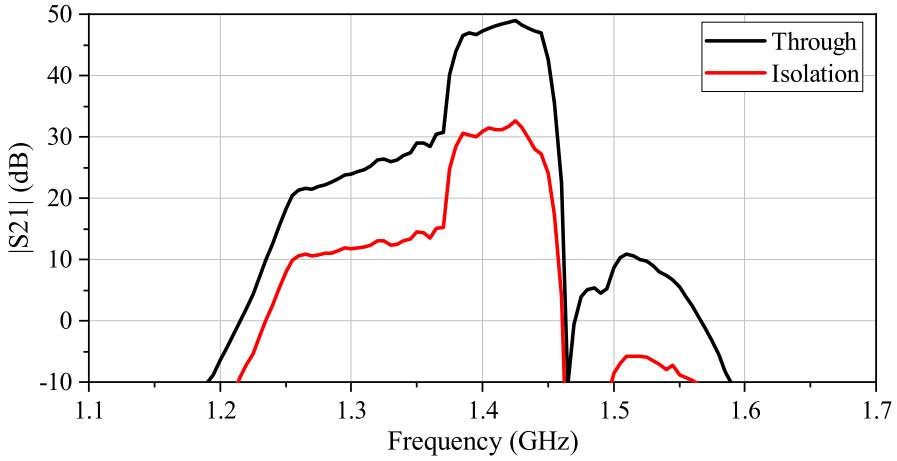
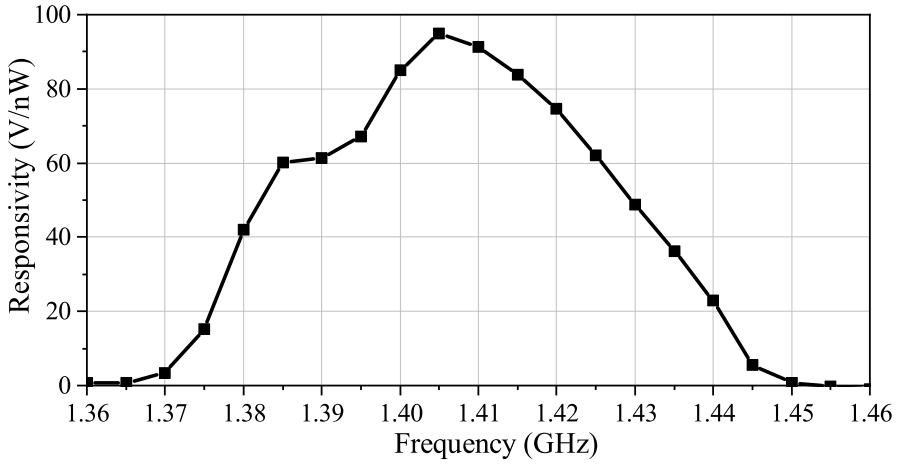


Figure 4.12: Photograph of hybrid correlation-Dicke radiometer mounted on a PCB. An on-chip hybrid radiometer MMIC, BPF, and on-chip three stage LNA are placed in order. The size of the PCB is 42.7 mm x 30 mm.

Subsequently, the amplified RF signal is routed to an RF-to-DC detector [29]. Fig.4.13b displays the measured voltage responsivity of the radiometer. This measurement is conducted by using a signal generator at the radiometer's input and using an oscilloscope to record the output DC voltage while increasing the signal power. The slope of the voltage change in response to the increasing power defines the radiometer's responsivity. The responsivity is frequency dependent and peaks at 1.405 GHz with a value of $R_{peak} = 95\,\mathrm{V/nW}$. The integrated responsivity over frequency is computed as $4.28{\times}10^{9}\,\mathrm{V/nW}$.



(a)



(b)

Figure 4.13: (a) Measurement of RF gain of the radiometer from the inputs to the node before the detector. (b) Measured responsivity (V_{dc}/P_{RF}) of the radiometer.

In the microwave frequency range, the power spectral density p of thermal radiation can be approximated as white noise, expressed as $p = kT$. Therefore, $\Delta V = k\Delta T R_{peak} B$, and B is the power equivalent bandwidth. By applying this equation, we calculate $\Delta V/\Delta$ T $= 59\,\mu$V/K, indicating that the dc voltage increases by $59\,\mu$V with a 1 C° rise in temperature at the receiving element. This value is used to calculate T_{total} from voltage, explained in chapter 5 and 6.

4.4 Conclusion

In conclusion, this chapter demonstrates the development of a hybrid correlation-Dicke radiometer, combining the advantages of correlation and Dicke architectures to enhance robustness against gain fluctuations and load impedance change. The initial design, implemented on a PCB using off-the-shelf components, validates the hybrid architecture's performance. The measured results confirms its ability to achieve the required sensitivity and stability for internal body temperature measurements.

For further miniaturization and integration, a GaAs MMIC implementation of the hybrid radiometer was designed and fabricated. This chip integrates key components, including hybrid couplers, LNAs, and a switch, within a compact footprint of 3.8 mm $\times$ 2.3 mm, achieving a noise figure of 1.31 dB and gain of 13.4 dB. This MMIC is mounted on a PCB with other components and achieves gain of 49 dB.

This work was recognized at multiple international conferences, including the European Microwave Conference (EuMC 2022) [47] where it was a finalist for the Young Engineer award, and the IEEE International Microwave Biomedical Conference (IMBioC 2024) [44], where it received the Best Paper Award.

Chapter 5

Phantom Temperature Measurements

Contents

5.1 Tissue Phantom Background **67**

5.2 Two-layer Phantom Temperature Measurements with GaAs Dicke MMIC . **68**

5.3 Two-layer Phantom Temperature Measurements with Hybrid Radiometer MMIC **75**

5.4 Two-layer Phantom Temperature Measurements with InGaAs MMIC Dicke **78**

5.5 Conclusion **80**

This chapter presents the internal temperature measurements obtained using the near-field antennas and microwave radiometers described in previous chapters. The focus here is on temperature measurements with human tissue phantoms, which offer a more controlled testing environment compared to *in-vivo* measurements. Phantoms allow for consistent dielectric properties, regulated temperature control, and the insertion of a thermocouple for direct "ground truth" temperature measurement, facilitating more precise and repeatable testing.

5.1 Tissue Phantom Background

It is essential for the phantoms to closely replicate the electrical properties of human tissues. These dielectric properties are incorporated into the electromagnetic simulations in HFSS and influence both the design of the near-field antenna and the calculation of the weighting factors. Previous studies have used various materials, such as smoked salmon, chicken breast, and agar,

as tissue phantoms to mimic tissues [36]. Additionally, other studies have focused on developing and characterizing the dielectric parameters of these phantoms, ensuring they provide a stable and accurate representation of human tissue properties [61, 62, 63].

5.2 Two-layer Phantom Temperature Measurements with GaAs Dicke MMIC

An internal phantom temperature measurement is conducted using a two-layer phantom that replicates skin and muscle tissues. The skin layer is represented by a 2 mm thick SPAEG's skin phantom [37], while materials such as saline and Play-Doh are used to simulate muscle tissue. The near-field antenna, discussed in Chapter 2, is positioned on the skin phantom to detect black-body radiation from the two-layer stack.

For a two-layer tissue model, the total weighted temperature, shown in eq.2.1, is expressed as:

$$T_{\text{total}} = W_{\text{skin}} T_{\text{skin}} + W_{\text{muscle}} T_{\text{muscle}} \ , \tag{5.1}$$

The weights of each layer, W_{skin} and W_{muscle}, are determined through the integration of Joule loss density in an EM simulation. The total temperature(T_{total}) is determined based on the radiometer characterization described in chapter 3 and 4. The skin temperature(T_{skin}) is measured using a thermocouple. By applying the eq.5.1, the only remaining unknown variable is the muscle temperature(T_{muscle}), which represents the internal temperature.

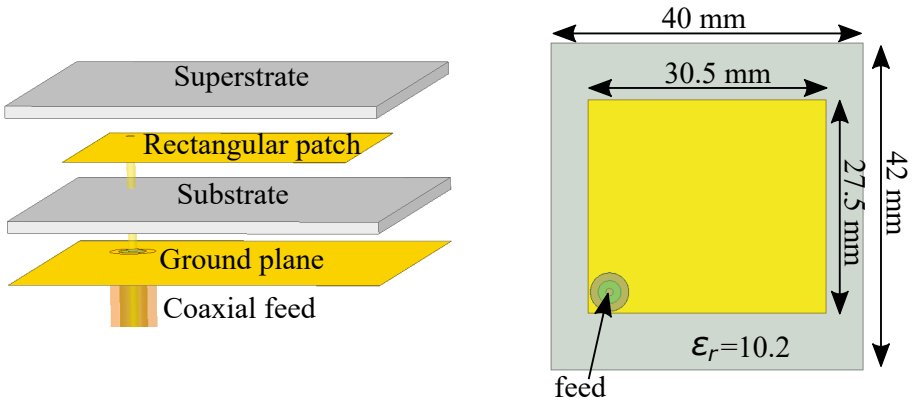


Figure 5.1: Cross-section of the near-field antenna designed for thermal power retrieval, featuring a high sensing coefficient from the muscle phantom layer (left), along with top view of the near-field antenna with detailed parameters (right). Details about the design is given in chapter 2.3.

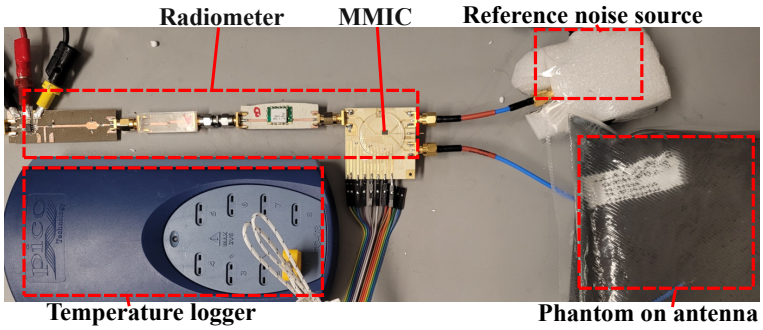


Figure 5.2: Photograph of test setup for temperature measurement.

First, temperature measurements are performed using the rectangular patch antenna described in Chapter 2.3 and shown in Fig. 5.1. The near-field antenna is connected to the input of the Dicke radiometer MMIC described in Chapter 3.4 Fig. 3.9. For these measurements, one of the radiometer inputs is connected to the near-field antenna, which is placed directly on the skin tissue phantom. Beneath the skin phantom, a saline-filled bag simulates muscle tissue and is either heated to 60 °C (referred to as the 'hot muscle phantom') or kept at room temperature (25 °C, referred to as the 'cold muscle phantom'). During the experiment, the hot and cold muscle phantoms are alternated, as shown in Fig. 5.3. By controlling the muscle phantom temperature in this setup, the calculated weighting factors W_1 and W_2 can be validated.

For these measurements, the radiometer is calibrated against a reference noise source, in this

case, a matched 50-Ω coaxial load held at 25 °C controlled by a ThorLabs MTD415T thermistor temperature controller. The load is placed on top of a Peltier element connected to a heat sink and is thermally insulated with polystyrene foam. The radiometer output dc voltage, measured with a sampling oscilloscope, captures signals both from the near-field antenna and from the reference noise source. Calibration is achieved by subtracting these two voltages in the data processor, mitigating the impact of gain fluctuations within the radiometer components.

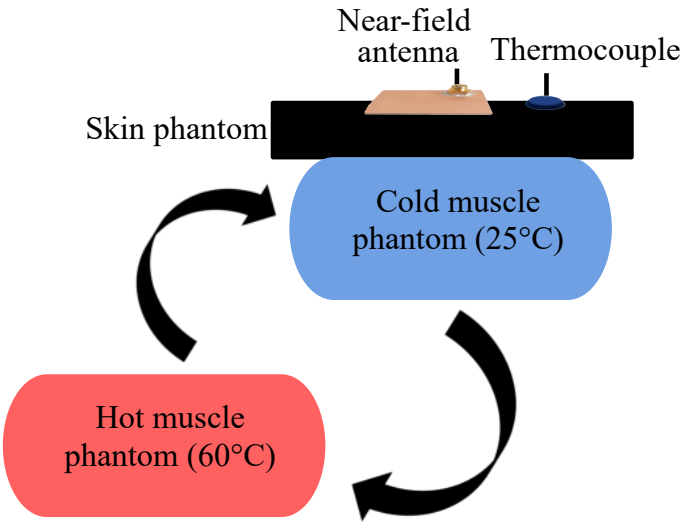


Figure 5.3: Illustration of the two-layer measurement setup. Two bags of saline muscle phantom ($\epsilon_r = 77.7, \sigma = 1.26$) are used. One is a hot phantom at 60°C, and the other is a cold phantom kept at room temperature, 25°C. These two phantoms are placed alternately one at a time under the skin phantom ($\epsilon_r = 28, \sigma = 0.84$) . The output voltage is then data processed and the estimated temperature is compared to the real "ground truth" temperature.

Fig. 5.4 shows the measured and calibrated output dc voltage of the radiometer, along with the temperatures of the hot and cold muscle phantom. This voltage represents the difference between the two inputs. At the staart of the measurement ($t = 0$), the cold muscle phantom is beneath the skin phantom. After approximately 20 seconds, the cold muscle phantom is swapped with the hot muscle phantom. During each 5 second transition period, the near-field antenna does not function as intended, due to mismatch. Thus, the voltage readings in these intervals are not meaningful and are shaded in grey in the plot. As expected, the radiometer shows a low output voltage when the cold muscle phantom is in place compared to the hot muscle phantom, indicating that the received

noise power is lower with the cold phantom.

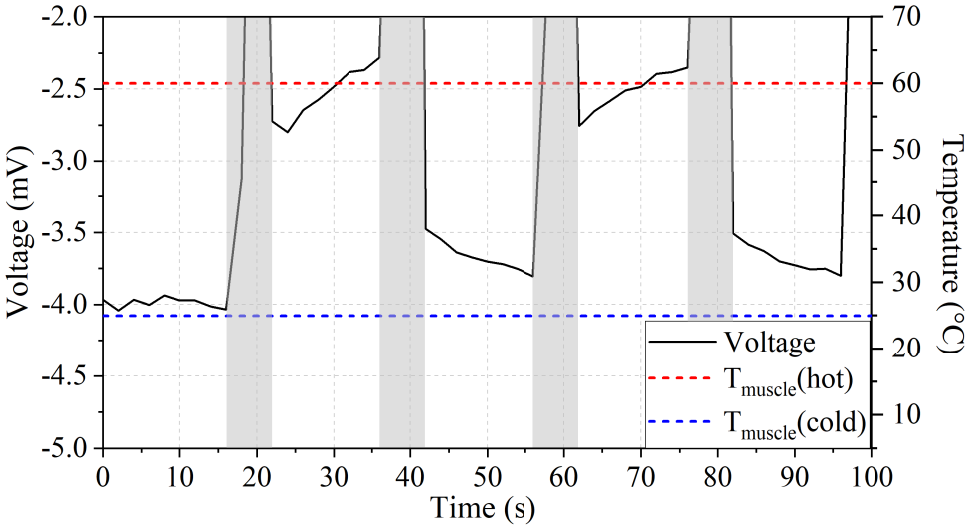


Figure 5.4: Measured calibrated output of the detector when a hot (60 °C) and cold (25 °C) muscle phantom is placed under the skin phantom approximately at 20 s intervals. The output voltage increases with the hot muscle phantom, as expected. The spikes around 20, 40 s, etc., shaded in gray, are periods when the muscle phantom is alternated and the antenna is thus not behaving as designed.

Using the calibrated voltage and known skin temperature, the temperature of the muscle layer, T_{muscle}, can be estimated using eq.5.1. The radiometer measures the total noise temperature from the skin and muscle phantoms, in addition to any ambient temperature. In this analysis, eq.5.1 assumes the ambient contribution is negligible. This assumption is validated in simulations, which result in an environment weighting factor below 5%.

The coefficients W_{skin} and W_{muscle} represent the percentage of noise power from each of the two separate layers, calculated by integration of the simulated volume loss power density using reciprocity [23]. Fig. 5.5 shows the simulated volume Joule loss density for the near-field antenna and phantom tissue stack, simulated in transmission with 1 W of input power at the probe feed. The weighting coefficients are determined as the ratio of the Joule loss in a particular volume to the total Joule loss across the stack up, and the values are shown in Fig. 5.5.

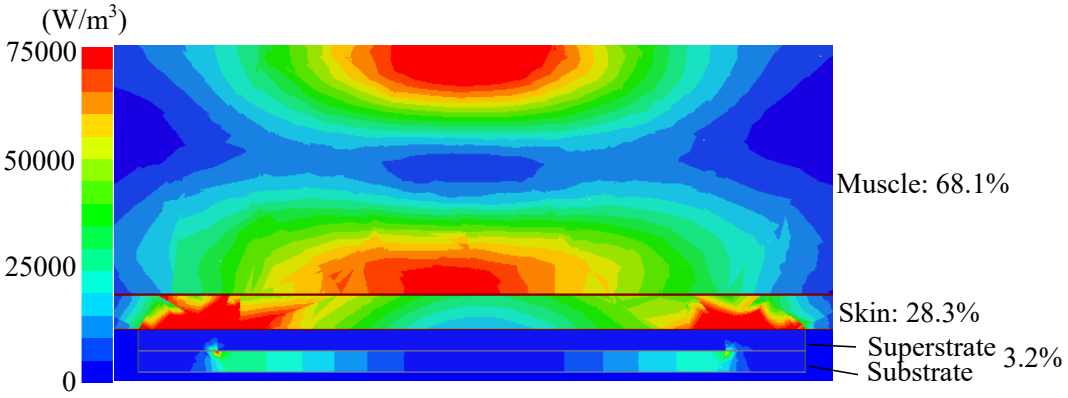


Figure 5.5: Full-wave simulations of volume Joule loss density ($\mathrm{W/m^3}$) of the near-field antenna on a skin-muscle phantom with 1 W at the feed. The weighting factors (percentages of total power) are also stated, with approximately 3% of the total power being in the surrounding air and unaccounted for here. The thickness of the skin is 2 mm and the thickness of the muscle is 15 mm.

In the simulations, the tissue stack volume is truncated to 6 cm × 6 cm×1.7 cm, with tests of larger volumes yielding similar results, confirming the validity of this approximation. The temperature of the skin phantom, T_{skin} is independently measured by a thermocouple in direct contact with the skin and is considered known. The temperature of the muscle, T_{muscle}, is calculated from eq.5.1. Fig. 5.6 shows T_{muscle} compared to the actual known temperature of the saline phantom. The average error is 0.77 °C and the maximum error is 3.2 °C.

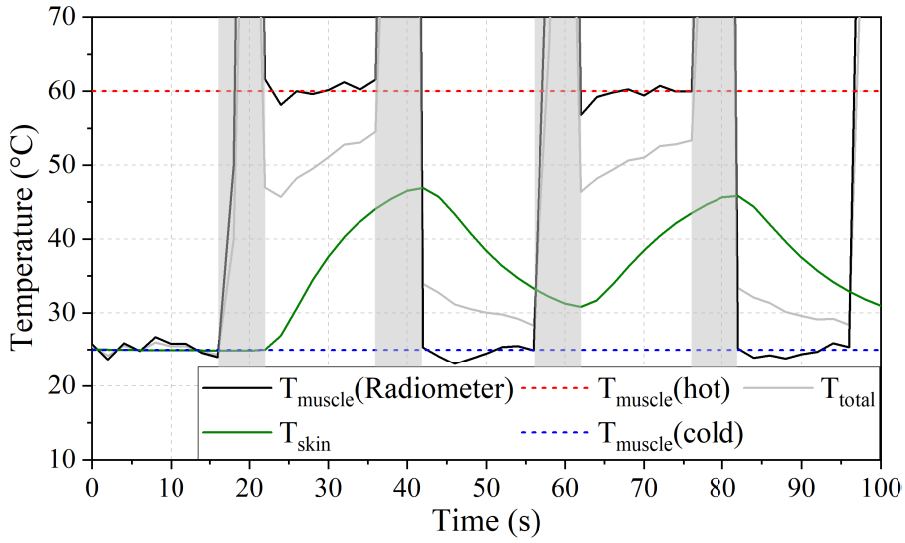


Figure 5.6: Measured temperature of the muscle tissue phantom, using T_{skin} (green line) measured by a thermocouple and subtracted in post-processing. The red and blue dotted lines show the temperatures of the water bath used to set the known phantom temperature, 60°C and 25°C.

A second temperature measurement is conducted using Play-Doh as the muscle phantom instead of a saline bag, with its dielectric properties listed in Table 2.2. The saline bag method had limitations due to unavoidable air bubbles, which introduced inconsistencies as bubbles moved to different parts of the phantom at various points during the measurement. Additionally, the true temperature of the saline muscle phantom could only be known for a limited time after it was removed from a heated water bath, impacting measurement accuracy.

In contrast, the Play-Doh phantom allows continuous temperature measurement using a thermocouple inserted directly into the Play-Doh, providing a more stable reference temperature. For this temperature test, a thermal insulator is placed between the skin and muscle phantoms to delay thermal equilibrium, ensuring that the muscle and skin temperatures remain distinct over an extended period. Due to the electrical property differences between the Play-Doh and the saline, the weighting factors are also different, as shown in Fig. 5.7.

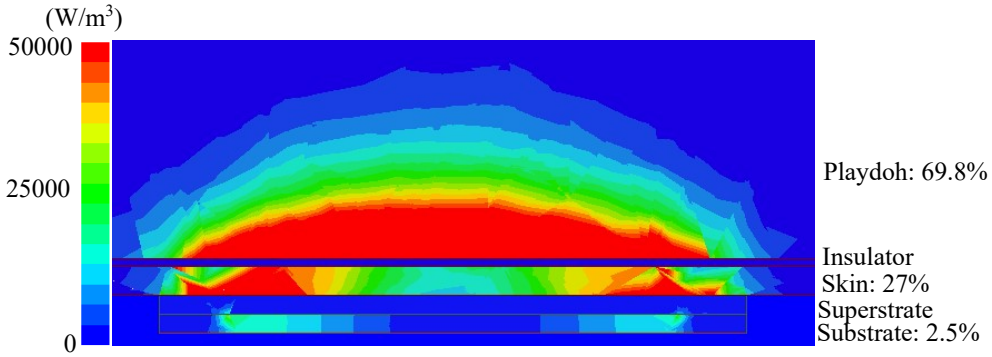


Figure 5.7: Full-wave simulations of volume Joule loss density (W/m^3) with 1 W at the feed. Play-Doh is used as a muscle phantom instead of saline. A thermal insulator is placed between the skin and muscle layer to delay the time of thermal equilibrium. The weighting factors (percentages of total power) are also stated. The thickness of the skin and muscle is 2 mm and 15 mm.

The temperature measurement takes 400 samples over approximately 45 minutes. The test uses hot and cold muscle phantoms, and both measurement results are shown in Fig. 5.8. For the hot muscle phantom test, a cooling trend of the muscle phantom is observed as the skin phantom warms up. The skin phantom temperature is subtracted from the total temperature, using the same method as for the saline phantom. However, the algorithm uses a different weighting factor value

(27% for skin instead of 28.3%) due to different electrical properties of the muscle phantom.

The estimated muscle phantom temperature closely aligns with the real-time value measured by a thermocouple, showing an average error of 0.247 °C and a maximum error of 1.25 °C. The thermocouple is placed at the bottom of the Play-Doh about 3 mm above the insulator since this is the area where most of the blackbody radiation originates due to the high Joule loss.

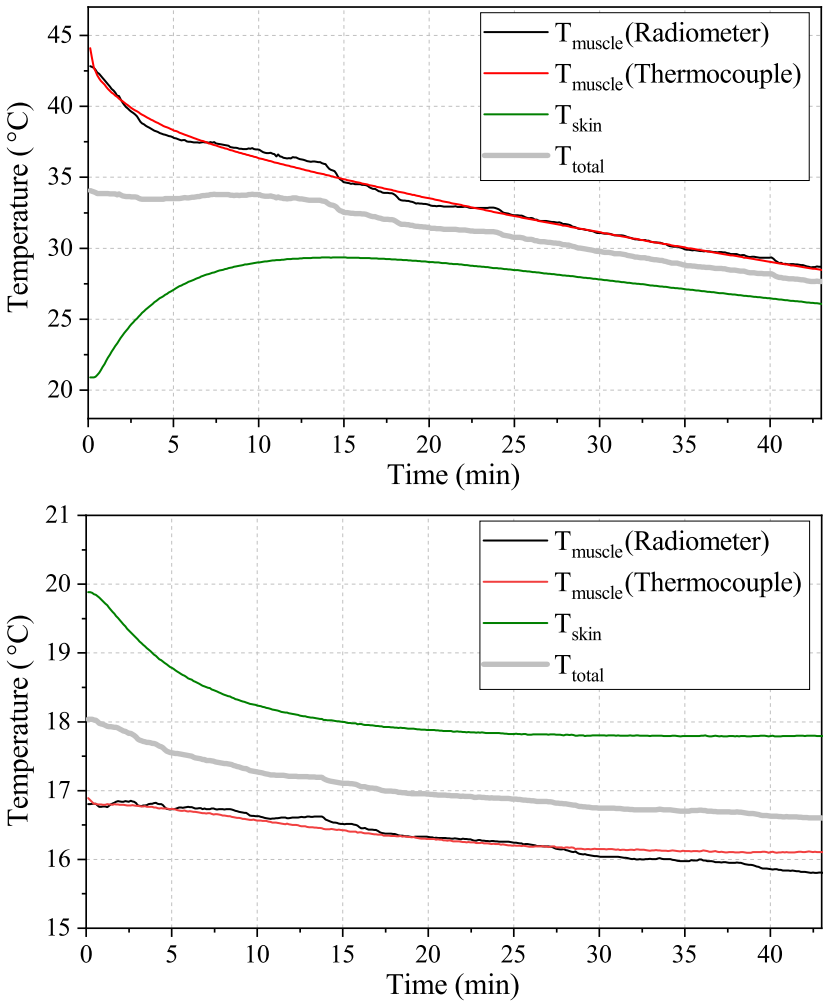


Figure 5.8: Temperature measurement (with thermocouple) and estimation (from radiometer output) when Play-Doh muscle phantom is placed under the skin phantom. Both hot Play-Doh (top) and cold Play-Doh (bottom) tests are conducted for validation across temperatures.

Another test is conducted using a cooled Play-Doh phantom. The estimation, in this case, has an average error of 0.1 °C and a maximum error of 0.31 °C ompared to the actual temperature

measured with a thermocouple. This test verifies that the radiometer can accurately measure the temperature of buried layers both above and below room temperature.

5.3 Two-layer Phantom Temperature Measurements with Hybrid Radiometer MMIC

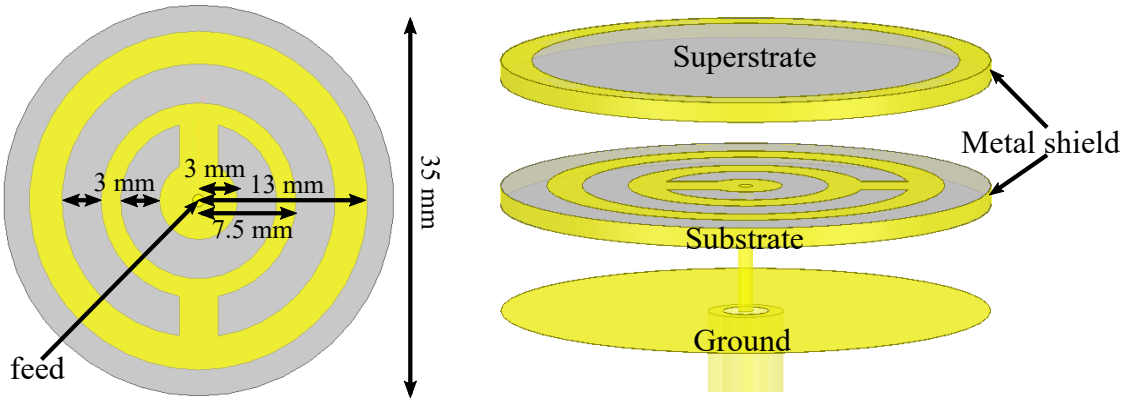
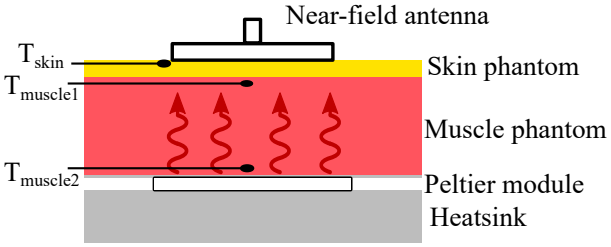


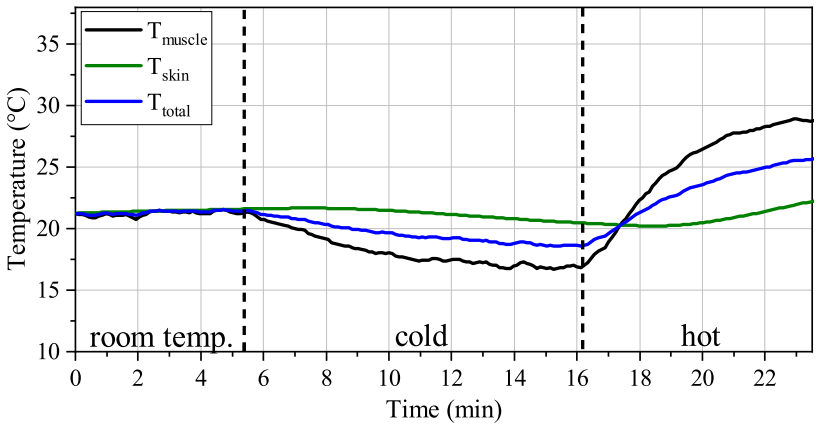
Figure 5.9: Top view and cross-section of the near-field antenna designed for thermal power retrieval. The sides of the antenna are covered by metal shielding.

The 2-layer skin and muscle measurement was also conducted using the hybrid radiometer MMIC, described in Chapter 4.3 Fig. 4.7, along with the circular slotted near-field antenna from Chapter 2.4 and shown in Fig. 5.9. The near-field antenna is connected to the input of the radiometer using a coaxial cable. A 50 Ω resistor at room temperature is connected to the other input as a known reference noise source. The SPDT switch on the MMIC alternates between these two inputs at a speed of 10 Hz to calibrate gain fluctuations.

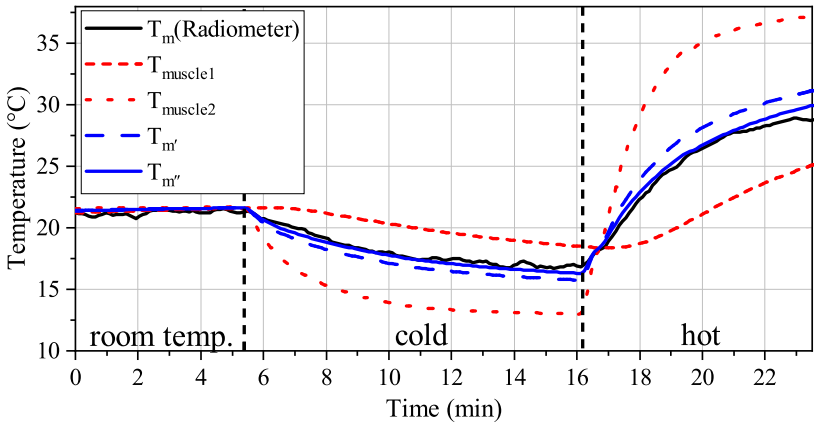
During the measurement, the radiometer's output dc voltage is continuously recorded using an oscilloscope. The voltages from the two states of the switch are subtracted for calibration and the difference is then integrated for 1 second to reduce error, and this integrated value is referred to as ΔV.



(a)



(b)



(c)

Figure 5.10: (a) Measurement setup of temperature measurement on a 2-layer phantom. (b) Measured temperature of 2 layer phantom. Skin temperature is subtracted from the total temperature to derive T_{muscle}. (c) plot compares T_{muscle} from the thermocouple measurement. T_{m1} and T_{m2} is the temperature measured from the thermocouple at the top and bottom of the muscle phantom. $T_{m\prime}$ is the average of T_{m1} and T_{m2} and $T_{m\prime\prime}$ is the combination of T_{m1} and T_{m2} in 6:4 ratio.

The temperature measurement setup for the 2-layer skin-muscle tissue phantom, shown in Fig.5.10a, includes a Peltier module positioned at the base of the muscle layer to control its temperature from the bottom. A 2 mm thick Spaeg phantom [37] is positioned on top of a 2 cm thick Play-

Doh, used as a muscle phantom. Three thermocouple sensors are placed to measure real-time temperature: one on the skin phantom(T_{skin}); the second on the top of the muscle phantom($T_{muscle1}$); and the third one on the bottom of the muscle phantom($T_{muscle2}$).

During the measurement, the Peltier module is initially turned off to measure the phantom stack at room temperature. The Peltier cell then cools the muscle phantom for about 10 minutes before heating it up. The voltage difference is integrated for 1 s, yielding a value that is called ΔV. As the measurement proceeds, ΔV changes and is divided by the $\Delta V/\Delta T$ value calculated from the characterization of the radiometer in Fig. 4.13b in Chapter 4 to determine the temperature change. The weighting factors are then applied to estimate the temperature of the muscle using the following equation:

$$T_{\text{total}} = W_{\text{skin}} \cdot T_{\text{skin}} + W_{\text{muscle}} \cdot T_{\text{muscle}} + W_{\text{ant}} \cdot T_{\text{ant}} \tag{5.2}$$

The value of T_{skin}, measured with a thermocouple, is used to calculate T_{muscle}. We assume that the skin and antenna temperature are the same, $T_{\text{skin}} = T_{\text{ant}}$. Fig. 5.10b shows both the total measured temperature, T_{total}, aswell as the calculated muscle temperature, T_{muscle}. The radiometer's measurements align with the expected cooling and heating trends observed in the muscle phantom, as confirmed by a thermocouple sensor within the phantom.

In Fig. 5.10c, the temperature measurements from the radiometer are compared with both the average of the two muscle phantom thermocouple readings and a 6:4 weighted ratio of the top and bottom thermocouple outputs. For the average real-time temperatures measured by thermocouples, the radiometric estimation exhibits an average error of 0.95 °C. However, for the 6:4 weighed ratio plot, the error decreases to 0.35 °C. This reduction in error occurs because the near-field antenna, positioned on top of the skin, receives more thermal noise from the upper portion of the muscle layer, giving it a higher weight in the temperature calculation and thus improving accuracy with the 6:4 weighted approach.

5.4 Two-layer Phantom Temperature Measurements with InGaAs MMIC Dicke

Temperature measurements were performed using the InGaAs-based radiometer in conjunction with a dual-feed NFA, as depicted in Fig. 5.11, on a tissue phantom. A 20 mm thick heated Play-Doh layer, simulating muscle tissue, is placed beneath a 2 mm thick skin phantom. This test setup tracks the changes in skin and muscle temperatures as they approach thermal equilibrium. As the skin phantom that starts at room temperature (20°C) heats from the 34°C heated muscle phantom, the radiometer reads a temperature increase over time. Thermocouples embedded within the muscle phantom and placed on the surface of the skin phantom enable direct "ground truth" temperature measurements.

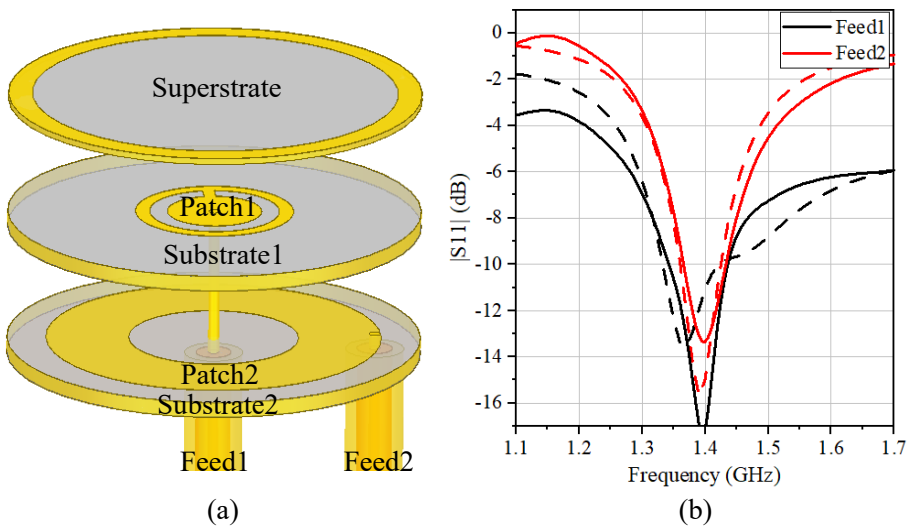


Figure 5.11: (a) Cross section of the two-feed near field antenna. (b) Reflection coefficient of near-field antenna when placed on the skin-muscle phantom. Measurement shown in solid line and simulation shown dashed line.

Figure 5.12 illustrates the relative temperature measurements acquired using the radiometer. For calibration, the radiometer is referenced against a known noise source, specifically a 50-Ω load maintained at room temperature. This calibration ensures accurate conversion of the radiometer's output signal into temperature values. Using the radiometer's characterization parameters, the total power temperatures, T_{total1} and T_{total2}, are derived from the output voltage levels recorded by a

sampling oscilloscope. By incorporating the known weighting factors of the skin and muscle layers, a temperature retrieval algorithm is applied to estimate the individual temperatures of the skin (T_s) and muscle (T_m). This algorithm is a linear relationship between the total measured temperature and the weighted contributions of each layer:

$$T_{total1} = W_{s1}T_s + W_{m1}T_m \tag{5.3}$$

$$T_{total2} = W_{s2}T_s + W_{m2}T_m \tag{5.4}$$

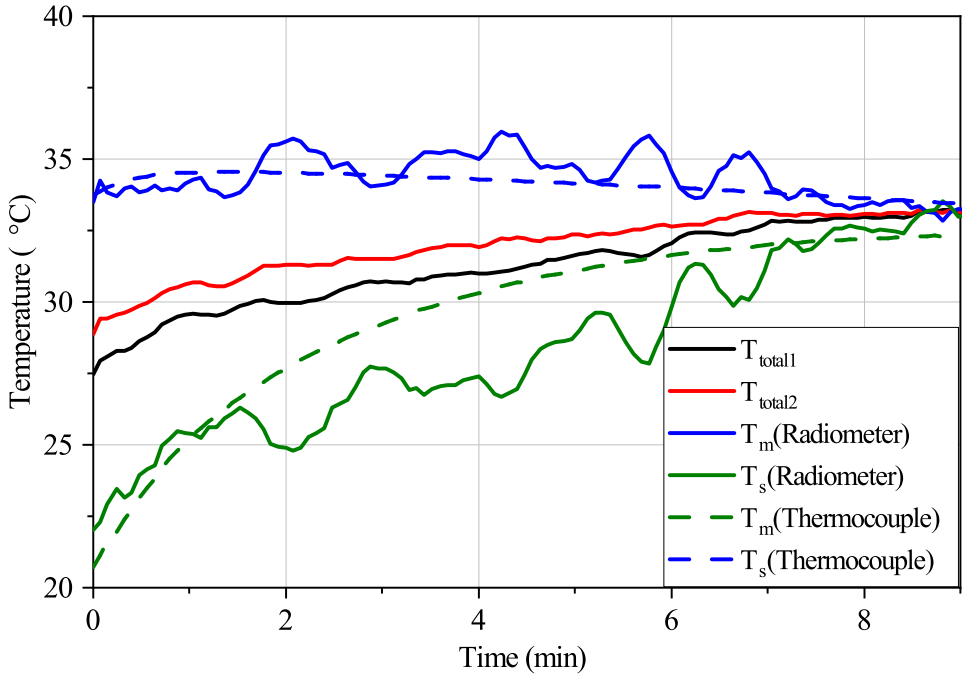


Figure 5.12: Temperature measurement of the system using 2-layer tissue phantom stack up, showing thermocouple "ground truth" measurements in dashed line. T_{total1} and T_{total2} are measured when the switch connects the radiometer input to Feed1 and Feed2, respectively.

The accuracy of the radiometer's temperature measurements was evaluated, with the following results. The average error for T_s is 1.58 °C and the maximum error is 3.8 °C. The average error for T_m is 0.57 °C and the maximum error is 1.79 °C. These results demonstrate the system's higher accuracy in estimating muscle temperature compared to skin temperature.

Fluctuation in the temperature measurements is quantified as follows. For this NFA design, with a difference in weighting factors (W_{m1} and W_{m2}) of only 0.123, a 1°C fluctuations in T_{total1} causes fluctuation of 4.84°C in T_s and 3.27°C in T_m. If an antenna with a larger difference in the two weighting factors is designed, for example 0.246 (twice as large) difference in W_{m1} and W_{m2}, the same 1°C fluctuation in T_{total1} would result in smaller fluctuations of 2.42°C for T_s and 1.63°C for T_m.

5.5 Conclusion

In conclusion, this chapter highlights the successful application of the developed radiometers for human tissue phantom temperature measurements. By employing near-field antennas designed for deep tissue sensing, along with Dicke and hybrid correlation-Dicke radiometer architectures, precise internal temperature measurements are achieved using two-layer tissue phantoms. The integration of controlled testing environments with reliable phantom materials enables the validation of weighting factors and provides direct comparisons with thermocouple measurements.

The results demonstrates the capability of the Dicke radiometer MMIC to distinguish temperature variations within the tissue layers effectively. Furthermore, testing with the hybrid radiometer MMIC paired with a circular NFA demonstrates enhanced performance. Measurements performed using a 2-feed NFA show the ability to monitor temperature variations in two-layer phantoms without reliance on external thermocouple measurements. With average temperature measurement errors as low as 0.1 °C for certain setups, these findings affirm the system's potential for non-invasive internal temperature monitoring.

This work was published in various IEEE publications. the Dicke radiometer with rectangular antenna was presented at IMS 2023 and published in the special issue of IEEE MWTL [42] and extended to IEEE MTT 2023 [43]. The hybrid radiometer with circular antenna was presented in IEEE ImBioc 2024 [44].

Chapter 6

In-vivo Measurements

Contents

6.1 *In-vivo* measurement with Dicke MMIC **82**

6.2 *In-vivo* measurement with Hybrid Radiometer PCB **85**

6.3 *In-vivo* measurement with Hybrid Radiometer MMIC **88**

6.4 Repeatability **90**

6.5 Sensitivity Study **92**

6.6 Conclusion **94**

This chapter focuses on *in-vivo* temperature measurements, which are critical for demonstrating the capability of the sensor to measure internal human temperatures. However, such measurements are challenging because accurately determining the ground truth temperature is difficult. For instance, demonstrating the ability to measure brain temperature is problematic as inserting a sensor into the brain for comparison would require animal studies, .

To address this, the method used in this work involves measuring the temperature of a liquid inside the subject's mouth while placing the near-field antenna on the cheek. This setup allows for the insertion of a separate thermocouple inside the mouth to provide a ground truth measurement for comparison.

This chapter begins by demonstrating the capability of 3 versions of the sensor, all at 1.4 GHz, to measure the temperature of a changing liquid inside a human cheek. This allows to compare 3 different radiometers and NFA designs. Following this, a repeatability analysis is conducted to

evaluate the consistency of measurements, along with an assessment of the system's sensitivity to variations in tissue properties.

6.1 *In-vivo* measurement with Dicke MMIC

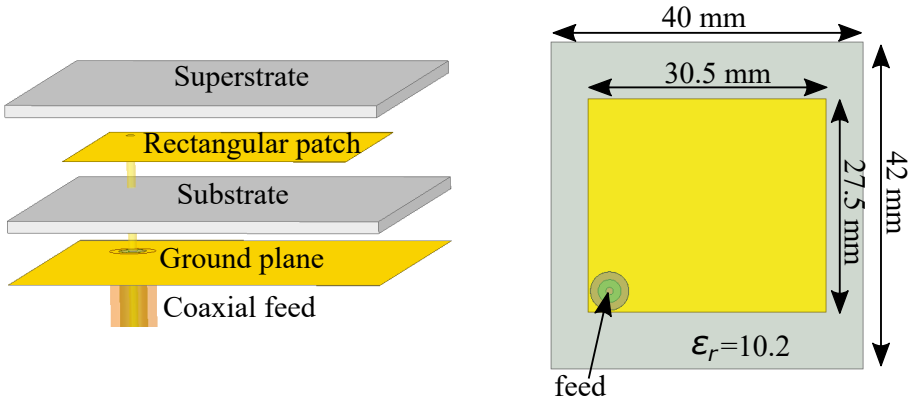


Figure 6.1: Cross-section of the near-field antenna designed for thermal power retrieval, featuring a high sensing coefficient from the muscle phantom layer (left), along with top view of the near-field antenna with detailed parameters (right). Details about the design is given in chapter 2.3.

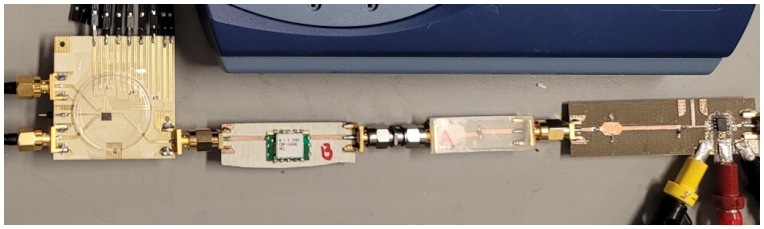


Figure 6.2: Photograph of test setup for temperature measurement. Hot and cold muscle phantoms are alternated and placed on top of the skin phantom, with the near-field antenna underneath and not visible in the photo.

The *In-vivo* measurement is first demonstrated using the rectangular patch antenna introduced in Chapter 2.3 and shown again in Fig. 6.1. This NFA is connected to the Dicke radiometer MMIC described in Chapter 3 and shown in Fig. 6.2. This measurement is conducted using temperature-varying tap water inside the mouth, providing a passive and non-invasive test setup. The near-field antenna is placed on the cheek, as shown in the photograph in Fig. 6.3, while the water temperature is varied inside the mouth.

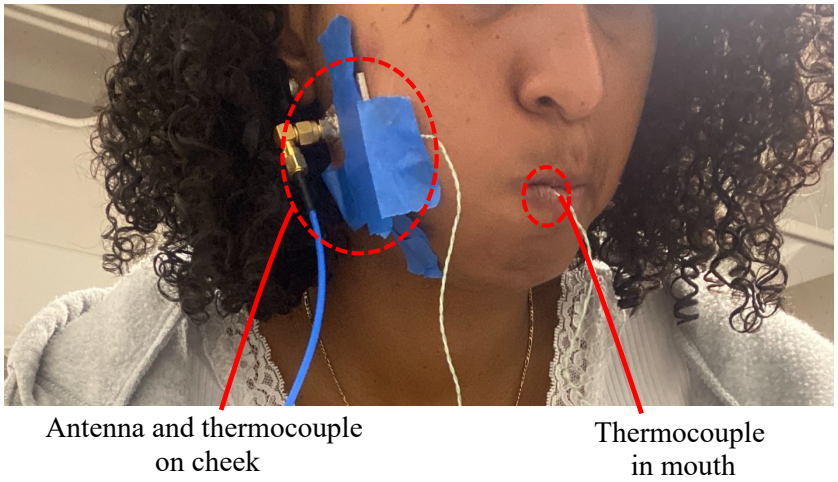


Figure 6.3: *In-vivo* measurement conducted on a human cheek. The near-field antenna is placed on the cheek to measure the temperature of hot or cold water inside the mouth. A thermocouple is placed inside the mouth to independently measure water temperature. (Courtesy Sofia Mvokany, University of Colorado, Boulder.)

The rectangular patch near-field antenna, previously tested with phantoms and detailed in Chapter 5, is well-matched to the tissue layers of the human cheek, with properties described in [1]. In this test, a circulator is connected between the antenna and the input of the radiometer to avoid power fluctuations due to antenna mismatch.

During the measurement, the near-field antenna is positioned on the cheek, and a thermocouple is placed inside the mouth to measure the actual water temperature. An additional thermocouple is positioned on the skin near the antenna to monitor any changes in skin temperature. Hot and cold water are alternately held in the mouth for 20 samples (about 110 s), while the radiometer records the temperature changes of the water. Notably, no significant changes in skin temperature were observed during these measurements, ensuring that the radiometer's readings were primarily influenced by the water temperature inside the mouth.

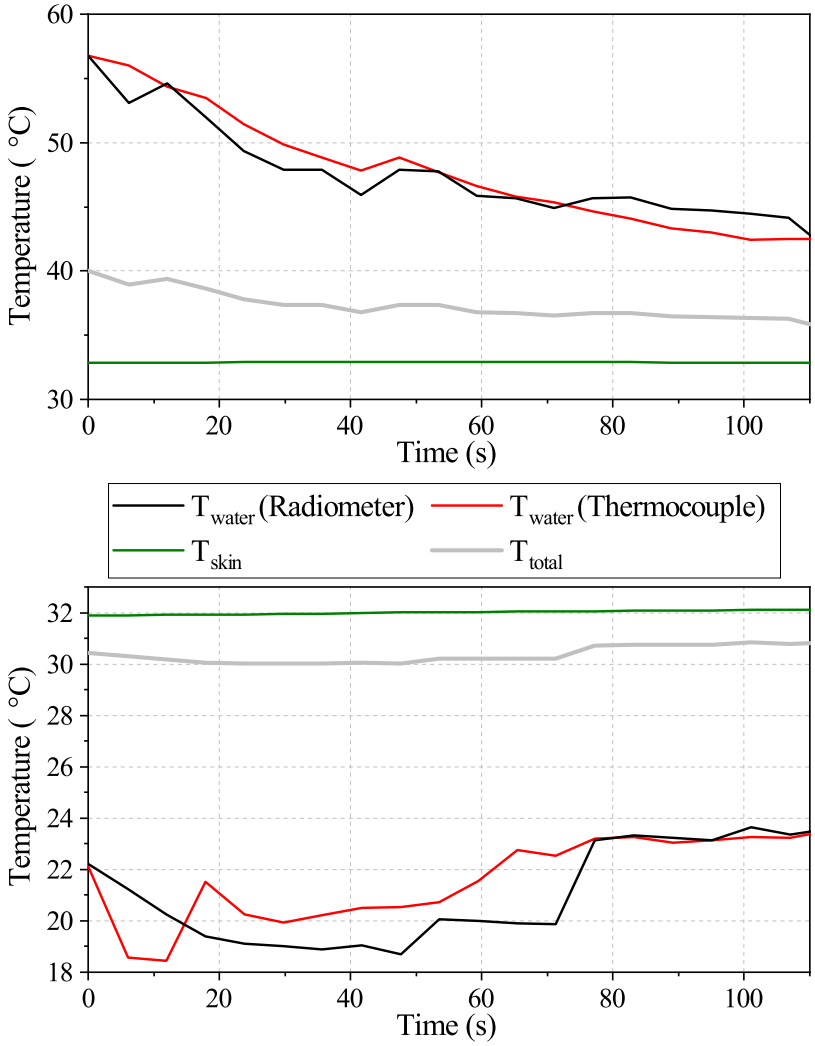


Figure 6.4: *In-vivo* temperature measurements on the cheek with hot water (top) and cold water (bottom) in the mouth. The temperature of the skin and the water inside the mouth is measured independently with thermocouples.

Equation (2.1) is used to estimate the water inside the cheek, applying weighting factors calculated by full-wave simulations of the near-field antenna placed on the cheek tissue stack comprising skin, fat, and muscle with properties shown in Table 2.2. The calculated weighting factor of the water inside the cheek is $W_{\text{water}} = 19.5\%$.

The estimated temperature results from these measurements are shown in Fig. 6.4. For both hot and cold water tests, the radiometer's temperature estimation closely tracks the real-time thermocouple measurements of the water temperature. The radiometer measurements shown an average

error of 1.17 °C and maximum error of 3.2 °C. The errors are the combination of many factors of the radiometer such as the reflection coefficient variation of the NFA and the RFI. The RFI near the 1.4 GHz band is substantially higher power then thermal noise, having a big influence in the radiometer measurement. Therefore, there needs to be a method to reduce RFI received by the NFA.

6.2 *In-vivo* measurement with Hybrid Radiometer PCB

Next, similar *in-vivo* measurements are performed with the hybrid radiometer implemented on a PCB. For these tests, the rectangular patch near-field antenna is utilized with the hybrid radiometer prototype described in Chapter 4.2 and reshown in Fig. 6.5. The near-field antenna uses a corner-fed rectangular patch topology on a 1.27 mm thick Rogers RO3010 substrate. The rectangular patch is similar to the rectangular patch shown for the previous measurement. However, the size of the patch is different and shown in [33]. The substrate size is 41.85 mm x 36.7 mm with patch size 29.15 mm x 4 mm. This NFA is designed specifically for the tissue layers of the cheek [1]. The near-field probe is positioned on the skin over the cheek. The reflection coefficient of this antenna is illustrated in Fig. 6.6.

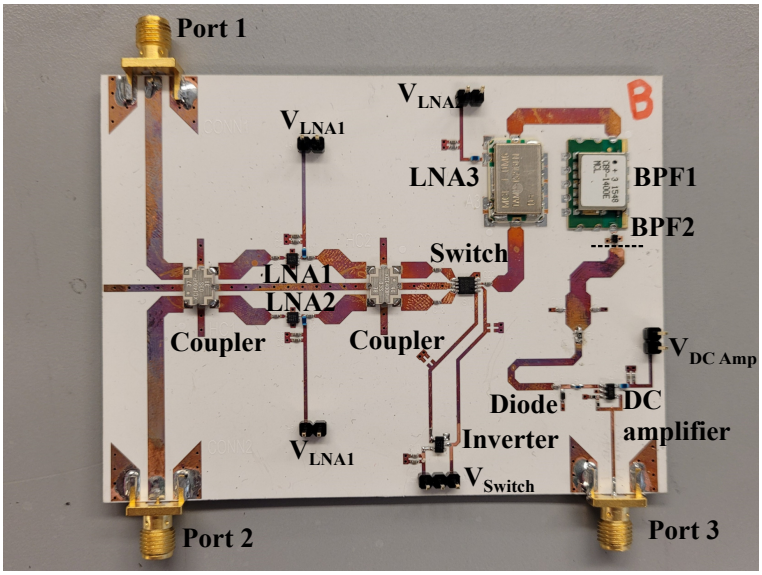


Figure 6.5: Photograph of the hybrid radiometer prototype.

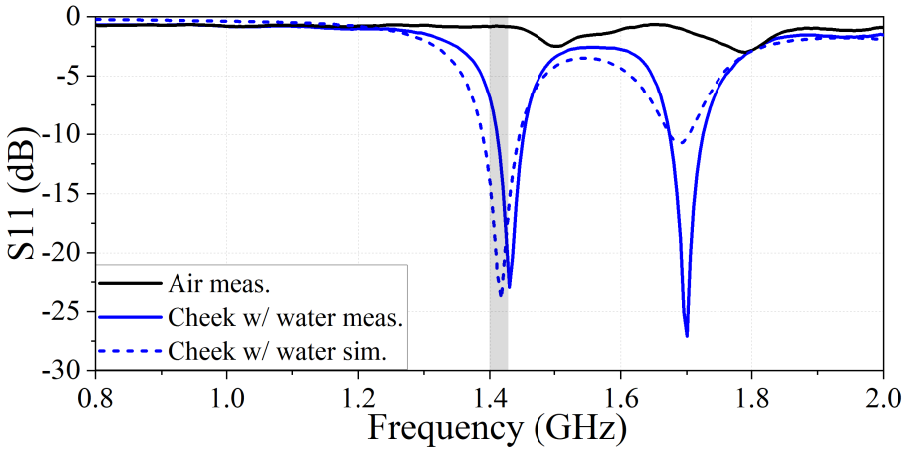


Figure 6.6: Measured reflection coefficient magnitude of the near-field antenna when placed on the cheek, comparing the match in air, on the cheek and simulations on the cheek. The shaded area is the design frequency band.

The weighting factors are determined by calculating the Joule losses, which depend on the electric field and conductivity properties of the cheek tissues. These calculations are shown in Fig 6.7.

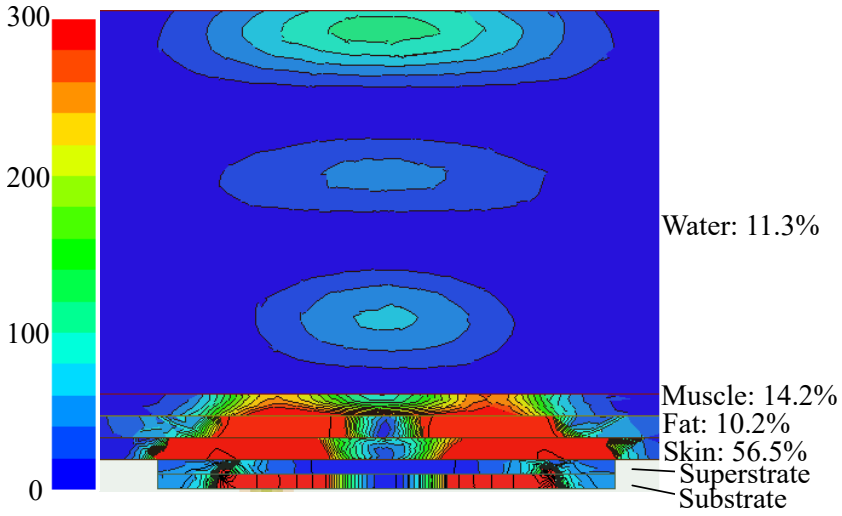


Figure 6.7: Full-wave simulations of volume Joule loss density (W/m^3) of the near-field antenna on a cheek tissue stack. The weights (percentage of total power) of cheek tissue layers are also stated.

The two input ports of the hybrid radiometer are connected to a reference load and the near-field antenna. The temperature of the reference load is stabilized using a Thorlabs temperature controller. The near-field antenna is attached to the cheek with adhesives, and a circulator is

included in the setup to prevent power fluctuations caused by probe mismatch.

The measured voltage at the output of the dc amplifier is shown in Fig. 6.8. The voltage difference, ΔV increases linearly with the temperature of the water inside the cheek, with a responsivity of 0.061 mV/°C.

When measured with a temperature-controllable load, the responsivity is 0.196 mV/°C, according to the temperature controlled load test done in Fig. 4.6. Using this data, the weighting factor of the water is determined to be $0.061/0.196 = 31\,\%$, instead of the 11% obtained from full-wave simulations. This discrepancy is primarily attributed to the variability in the electrical conductivity of tap water, which differs from the simulated assumptions.

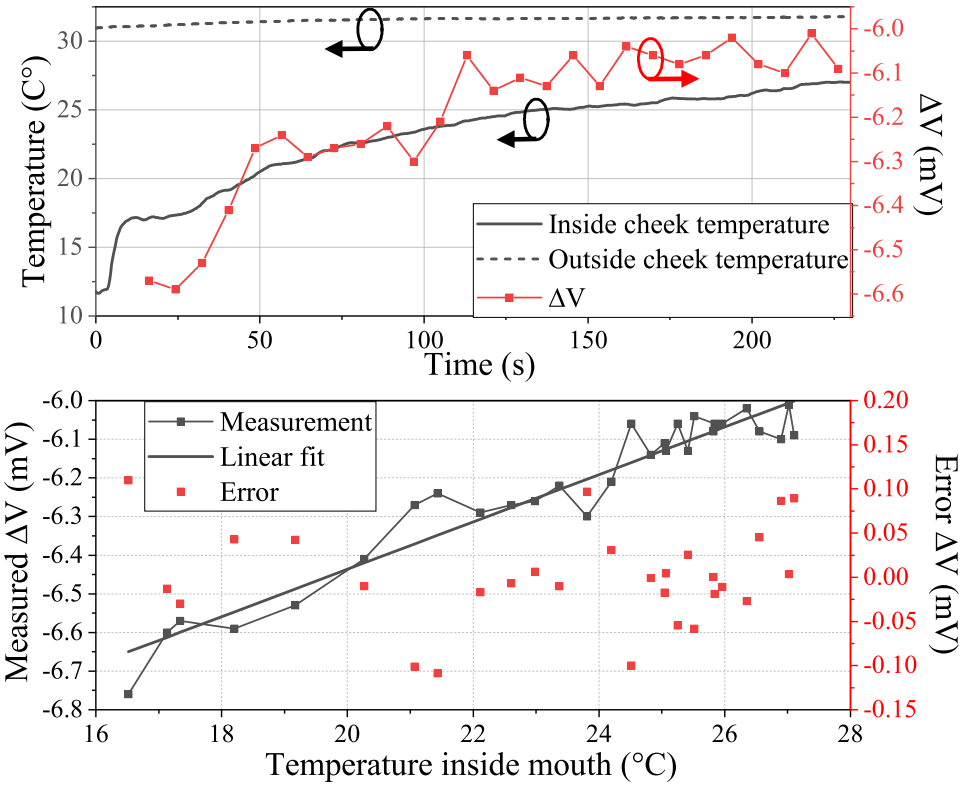


Figure 6.8: Top: Measured voltage at output of the radiometer as cold water in the mouth warms up. The temperature is measured with a thermocouple in the mouth. Bottom: Measured ΔV versus time for the same data set, with a linear fit and error of ΔV compared to the measured temperature.

6.3 *In-vivo* measurement with Hybrid Radiometer MMIC

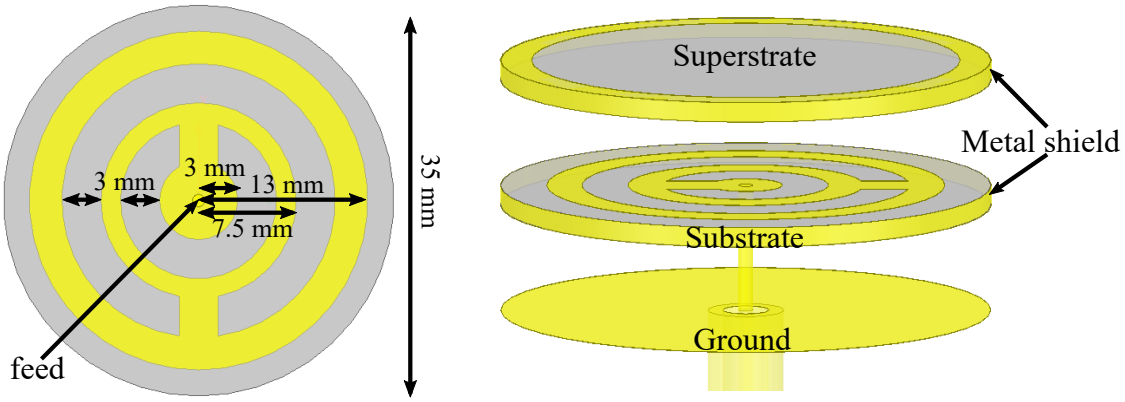


Figure 6.9: Top view and cross-section of the near-field antenna designed for thermal power retrieval. The sides of the antenna are covered by metal shielding. Details in Chapter 2.4.

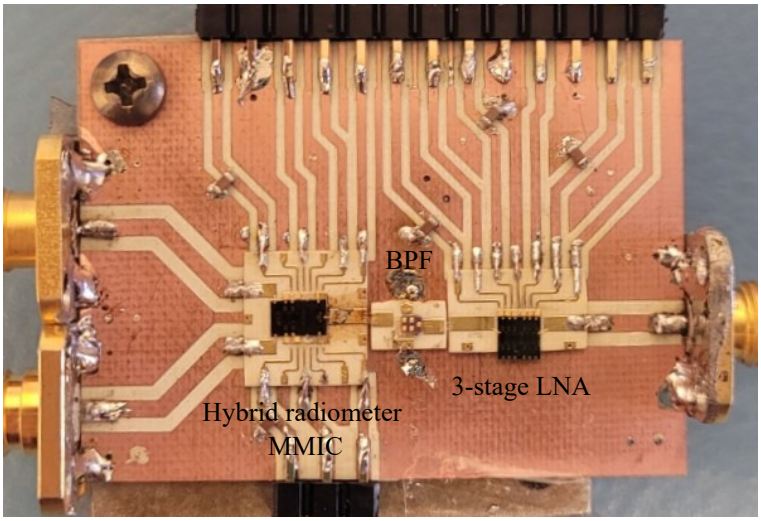


Figure 6.10: Photograph of hybrid correlation-Dicke radiometer mounted on a PCB. Details in chapter 4.2.

In-vivo measurements are also conducted using the circular near-field antenna detailed in chapter 2.4 and the hybrid radiometer MMIC described in chapter 4.3. The near-field antenna is positioned on the cheek, as shown in Fig. 6.11. Again, a thermocouple inserted inside the mouth serves as a ground-truth reference for the actual temperature of the liquid. Additionally, two other thermocouples are placed on the skin adjacent to the antenna to monitor any skin and antenna

temperature changes.

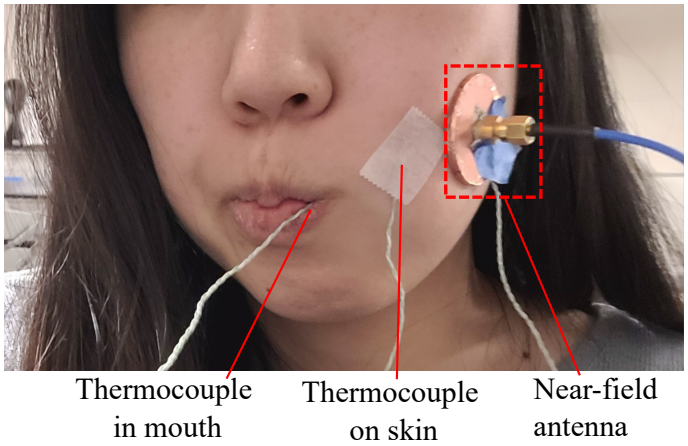


Figure 6.11: *In-vivo* temperature measurement on the cheek with liquid in the mouth. The temperature of the liquid, skin, and antenna is measured independently with thermocouples.

The measurement process begins with placing room-temperature liquid held in the mouth, followed by a 30 s radiometric measurement. Then, the liquid in the mouth is replaced with a heated liquid, around 43 °C. Another 30 s of radiometric measurement is conducted to track the temperature change of the liquid.

Weighting factors of this NFA were used to estimate the temperature of the liquid. The near-field antenna is placed on a tissue stack of skin, fat, muscle, and liquid. The calculated weighting factors are $W_{\text{skin}} = 46\%$, $W_{\text{fat}} = 10.4\%$, $W_{\text{muscle}} = 6\%$, $W_{\text{liquid}} = 33.4\%$ and the estimated temperature results of these measurements are shown in Fig. 6.12. The radiometer estimation follows the real-time thermocouple temperature measurement of the liquid with an average error of 0.72 °C and maximum error of 2.5 °C.

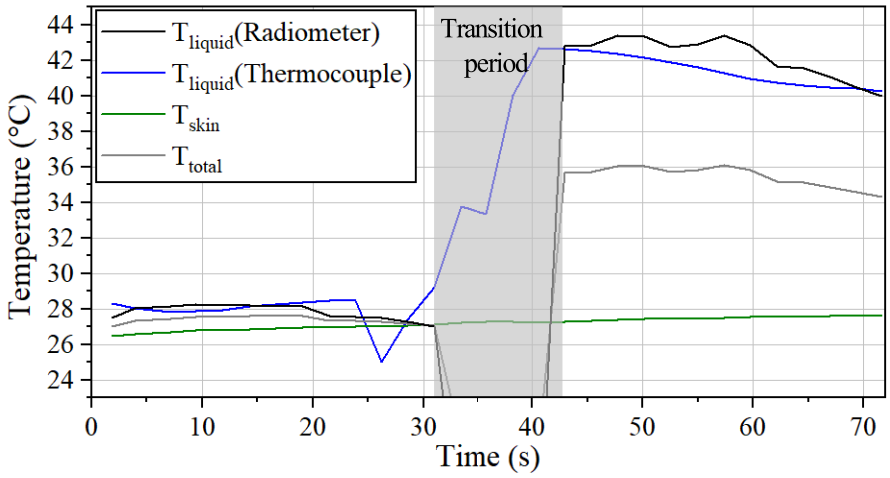


Figure 6.12: Measured temperature of liquid using radiometer output. The temperature is compared with the real-time temperature measured with a thermocouple inside the mouth.

6.4 Repeatability

Measurement repeatability is crucial for ensuring consistent and reliable thermometry results. However, previous works on microwave radiometers have not addressed repeatability. In this study, repeatability tests are conducted using the same setup as described in the previous section (Chapter 6.1.3). The near-field antenna is alternately placed on and off the skin of the cheek, and the test is performed with three different subjects. The test is conducted with three different subjects. It is assumed that the temperature of the cheek, as well as internal and external tissues, remains constant throughout the measurement. Therefore, the measured relative temperature should remain consistent each time the near-field antenna is placed on the skin.

Fig. 6.13 presents the measurement results, normalized to the mean value of each test run. The fluctuation in temperature, denoted as ΔT, represents the variation in the radiometer's output in temperature from the mean value. The measurement shows the maximum fluctuation of 2.5, 3.9, and 2.8 °C for the three subjects tested.

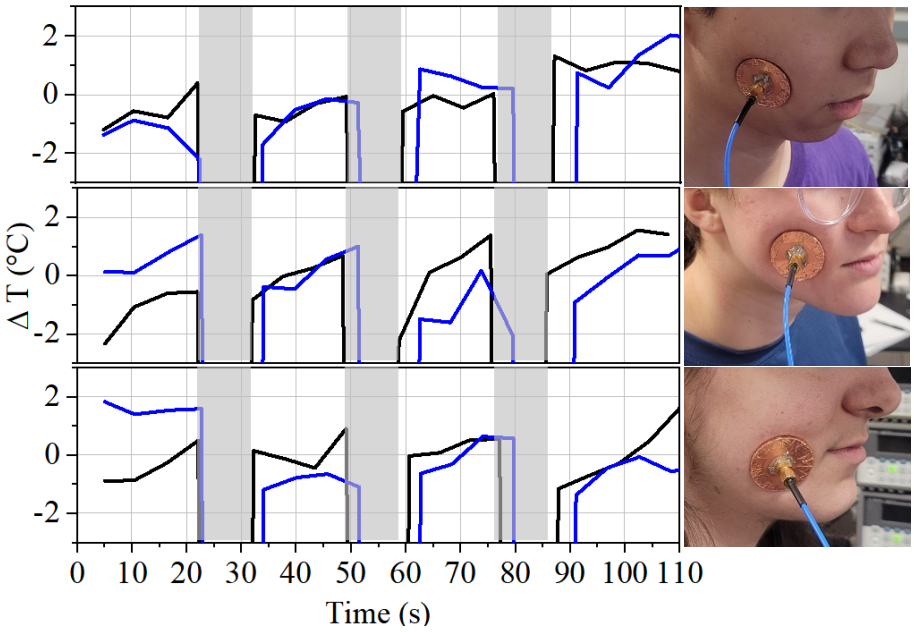


Figure 6.13: Radiometer *in-vivo* measurements repeated on multiple days for three subjects. The near-field antenna is placed on and off the cheek of the subjects. The transition period when the antenna is not on the cheek is shown in grey.

The primary cause of these fluctuations is attributed to changes in the reflection coefficient at the antenna feed. For instance, if the permittivity of the skin changes 10% in simulation, which is a reasonable change of skin tissue [64], the reflection coefficient minimum changes from $-16\,\mathrm{dB}$ to $-15\,\mathrm{dB}$. The percentage of reflected power is shown below:

$$\text{Reflected power}(\%) = \Gamma^2 = 100(10^{-\frac{16}{20}})^2 = 2.514 \tag{6.1}$$

$$\text{Reflected power}(\%) = \Gamma^2 = 100(10^{-\frac{15}{20}})^2 = 3.162 \tag{6.2}$$

This results in a 0.65% change in the reflected power, and a subsequent temperature error of 1.95 K in a 300 K environment. The repeatibility can be improved by e.g. measuring the reflection coefficient continuously and calibrating for the mismatch. Alternatively, a circulator can be used as in [7].

6.5 Sensitivity Study

The overall error in the internal temperature estimation is higher in the *in-vivo* measurements compared to measurements using phantoms. This discrepancy arises from several factors, including uncertainties in the temperatures of fat and muscle layers, as direct ground-truth measurements are not feasible without invasive methods such as needle probes. However, one of the main reasons for this increased error is the uncertainty in the electrical properties and thickness of the tissues. While the previous subsection discussed repeatability in measuring T_{total}, this section explores how variations in the electrical characteristics and thickness of tissues affect the temperature estimation algorithm.

Tissue layer properties, such as thickness, permittivity, and conductivity, vary significantly between individuals and across different body regions. To understand the impact of this variability, simulations were conducted to assess how changes in these properties influence the temperature measurements of subcutaneous tissue layers.

The sensitivity of the temperature estimate depends on the values of the weighting factors, which are directly influenced by variations in tissue properties. For example, the relative permittivity of dry and wet skin can vary up to ±6% at 1.4 GHz [38], while forehead skin thickness can vary by ±8% between different human bodies [64]. These variations, documented in the literature, provide standard deviation values for human skin properties, which were used to establish a property range for simulation.

Simulation results indicate that variations in skin thickness, from 1.84 mm to 2.16 mm, result in a 2.6 percentage point (pp) change in the skin's weighting factor. When varying the permittivity and conductivity, the weight of the skin changes by 4.4 pp and 3.7 pp, respectively. Among these factors, skin permittivity has the largest influence on the weighting factor values, demonstrating its critical role in temperature estimation accuracy. The sensitivity analysis and corresponding tolerances for weighting factors are summarized in Table 6.1. These findings highlight the importance of accurately characterizing tissue properties to improve the precision of *in-vivo* temperature

measurements.

Table 6.1: Weighting factors of tissue layers with skin property variation

Property	**Mean value**	**STD dev**	**Max** W_{skin}	**Min** W_{skin}
Thickness	2 mm	8%	0.291	0.265
ϵ_r	28	10%	0.303	0.259
σ	0.84 S/m	10%	0.298	0.261

Fig. 6.14 shows the volume Joule loss density for two scenarios of the skin-muscle stackup, Case 1 and Case 2, representing extreme variations in skin layer properties. The muscle phantom thickness is held constant across all simulations to match the dimensions used in the experimental setup.

In Case 1, the skin properties are set to minimize its weighting factor, with a thickness of $h = 1.84\,\text{mm}$, permittivity $\epsilon = 30.8$, and conductivity $\sigma = 0.756\,\text{S/m}$, respectively. Due to the reduced loss of the skin layer, the excitation from the near-field antenna senses deeper into the muscle, thereby increasing the muscle weighting factor. The weights corresponding to this configuration are $W_{\text{skin}} = 0.227$ and $W_{\text{muscle}} = 0.739$. The weighting factor of the muscle increased by 5.8 pp compared to the simulation done without these variation.

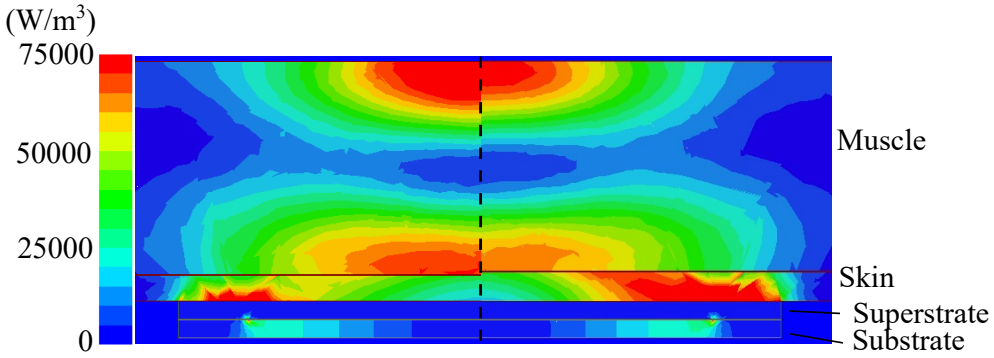


Figure 6.14: Side-by-side comparison of simulated volume loss density when skin properties are varied. Left: skin phantom properties: thickness, h=1.84 mm, ϵ=30.8, and σ=0.756 S/m. The resulting skin weighting factor is 22.7%. Right: skin phantom properties: h=2.16 mm, ϵ=25.2, and σ=0.924 S/m. The resulting skin weighting factor is 33.5%.

In Case 2, the skin properties maximize its weighting factor, with a thickness of $h = 2.16\,\text{mm}$, permittivity $\epsilon = 25.2$, and conductivity $\sigma = 0.924\,\text{S/m}$, respectively. The weighting factors of the phantom layers are $W_{\text{skin}} = 0.335$ and $W_{\text{muscle}} = 0.634$. In contrast to Case 1, the weighting factor of the muscle *decreased* by 4.7 pp compared to the simulation done without the variation. Thus, the muscle weighting factor varies by as much as 10.5 pp depending on the physiological skin tissue properties. Across both cases, the simulated reflection coefficient and radiated power differ by less than 0.4%, indicating that the variation in the weighting factor is not due to the change in the reflection coefficient.

Using the radiometer output voltage data in Chapter 3, and shown in Fig. 5.4, the impact of different skin layer weighting factors on muscle temperature estimation errors was evaluated.

For Case 1, where the skin weighting factor is at its lowest, the average error in muscle temperature estimation rises to 1.14 °C, with a maximum error of 4.04 °C. Meanwhile, for Case 2, where the skin weighting factor is at its highest, the average error increases to 1.58 °C with a maximum error of 4.62 °C. These correspond to increases of 0.37 °C and 0.81 °C increase from the original average error, respectively, compared to the original average error of 0.77 °C observed in simulations without skin property variations.

Accurate knowledge of tissue properties, such as thickness, permittivity, and conductivity, reduces estimation errors by improving the computation of layer weighting factors. However, even without explicit consideration of tissue properties, the average temperature estimation errors remain below 2°C. In real medical applications, where typical temperature swings are approximately 5°C[65], this level of error is expected to have a minimal impact on diagnostic accuracy.

6.6 Conclusion

In conclusion, this chapter presents the demonstration of non-invasive internal temperature measurement using near-field antennas and microwave radiometers in an in-vivo setting. By employing various radiometer designs, including the Dicke MMIC and hybrid radiometer MMIC, this work successfully validates the capability to monitor the temperature of liquid inside the human cheek.

The tests leverage both rectangular and circular near-field antennas, highlighting their performance under real-world conditions.

Key findings include the radiometer's ability to achieve high accuracy, with average errors of 1.17°C for the Dicke radiometer and 0.72°C for the hybrid radiometer. The improved performance of the hybrid radiometer is attributed to its advanced design features, including improved robustness to RFI due to metal-shielded near-field antenna design. Furthermore, repeatability tests demonstrates consistent temperature measurements across different users, while sensitivity analysis quantified the effects of tissue property variations on weighting factors and estimation accuracy.

This work was published in various IEEE publications. The Dicke radiometer with rectangular antenna was published in IEEE MTT 2023 [43]. The hybrid radiometer with circular antenna was presented in IEEE ImBioc 2024 [44].

Chapter 7

Conclusion and Future Work

Contents

7.1 Summary and Contributions **96**

7.2 Future Work **97**

7.2.1 Antenna with Spatial Pattern Diversity 97

7.2.2 Heterodyne Receivers 98

7.2.3 Phantom Manufacture and Characterization 99

7.2.4 Miniaturization of Hardware 100

7.2.5 Interference Mitigation 100

7.2.6 Neural Network for Tissue layer Characterization 101

7.1 Summary and Contributions

This thesis develops and characterizes microwave radiometers for non-invasive internal body temperature measurement, addressing the need for accurate, real-time thermometry. It presents the design, implementation, and validation of advanced radiometer architectures, including Dicke and correlation-Dicke hybrid designs, as well as GaAs MMIC radiometer front-ends featuring LNAs, switches, and couplers to achieve high sensitivity in compact form factors. Near-field antennas are optimized for deep tissue sensing, with performance validated through full EM simulations and two-layer tissue phantoms, achieving temperature resolution errors as low as $0.1^{/}circ$C. In-vivo tests using human cheek tissue confirm the sensor's effectiveness under realistic conditions, demonstrating

repeatability and robustness against variations in tissue properties. This work establishes a comprehensive framework for integrating microwave radiometers into wearable medical devices, offering a foundation for future advancements in continuous health monitoring and diagnostic applications.

The contributions of this thesis include the design and implementation of three novel near-field antennas. This includes the first demonstration of a dual-feed near-field antenna. Additionally, it features the first successful demonstration of on-chip radiometers, achieving a significant reduction in power consumption to approximately 80 mW for MMIC radiometers, compared to over 0.5 W for radiometers designed with off-the-shelf components. These radiometers were successfully applied to measure the temperature of tissue phantoms and water inside the cheek, providing precise temperature estimates for internal tissue layers. These advancements represent a significant leap forward in biomedical sensing and radiometry, showing potential for compact, efficient, and accurate sensors for non-invasive internal temperature monitoring.

7.2 Future Work

There are numerous opportunities to advance the development of a more precise and fully portable radiometer system for internal body thermometry. Future research efforts could focus on improving the accuracy of temperature measurements, further miniaturizing hardware components, and refining algorithms for more robust temperature estimation. This section discusses specific areas for improvement in near-field antennas, radiometer hardware, and temperature estimation algorithms.

7.2.1 Antenna with Spatial Pattern Diversity

Chapter 2 introduces a dual-feed antenna capable of measuring two total temperatures, each with distinct weighted contributions from different tissue layers. While this design shows significant promise, alternative approaches can further enhance temperature differentiation. One approach involves using antenna arrays to improve spatial resolution. For instance, previous studies demonstrate the use of four NFAs positioned around the head[66] to monitor conductivity changes in

a phantom. Antenna arrays allow for the measurement of larger areas, including the brain, and enable temperature measurements using various NFA combinations. For example, a configuration with four antennas generates a distinct field pattern compared to a two-antenna setup, providing additional equations to solve the complex problem of determining temperatures in N unknown layers, as discussed in Chapter 2.5.

Another approach involves designing multi-band NFAs that support various field patterns, each with unique weighting factors, as demonstrated in [41]. This design allows the radiometer to selectively target tissue layers at different depths. Additionally, optimizing the existing dual-feed NFA offers another avenue for improvement. Increasing the difference in weighting factors between the two feeds significantly enhances the precision of layer-specific temperature measurements. As described in the fluctuation analysis in Chapter 5.4, a greater separation in weighting factors reduces sensitivity to fluctuations in the total measured temperature. This results in more robust and reliable temperature retrievals, even under varying environmental conditions.

7.2.2 Heterodyne Receivers

Measuring internal body temperature with a wideband or multi-band NFA, discussed in the previous section, requires a wideband or multi-band radiometer. The radiometer designs in this thesis use narrow-band band-pass filters to reject out-of-band signals. However, wideband radiometers are sensitive to RFI in the outer bands, which introduces noise into temperature measurements. To mitigate RFI, a heterodyne receiver can be employed.

The heterodyne receiver first amplifies the RF signal, similar to a conventional narrow-band radiometer. After amplification, the RF signal is down-converted to an intermediate frequency (IF), where a low-pass filter removes unwanted outer-band signals. The operational frequency is determined by the local oscillator (LO) signal connected to the mixer with the RF signal. The operational bandwidth is defined by the low-pass filter's bandwidth after down-conversion, which is a trade-off of receiver sensitivity and error from RFI. Additionally, tuning the LO frequency allows the sensor to identify and operate at frequencies with minimal RFI. Implementing a heterodyne

receiver on-chip requires designing and integrating a mixer, an oscillator, and a wideband amplifier.

7.2.3 Phantom Manufacture and Characterization

Investigating methods for fabricating realistic tissue phantoms and accurately determining their permittivity is essential for improving tools used to validate radiometer temperature measurements. This thesis employs a commercially available 2 mm skin phantom [37] and saline or Play-Doh to mimic muscle tissue. However, phantoms with controllable thickness and permittivity are required to validate temperature estimation algorithms effectively. Additionally, for long-term usability, these phantoms must be shelf-stable.

Previous research has explored manufacturing multi-layer tissue phantoms [67, 63], where permittivity is measured using a dielectric probe kit. When fabricating phantoms, defining the material's permittivity is crucial for enabling accurate simulations in full EM simulators for calculating weighting factors. Fig. 7.1 illustrates a grounded coplanar waveguide (GCPW) setup with the material under test (MUT) shown in blue. The effective permittivity is derived from measured S-parameters, allowing calculation of the MUT's permittivity.

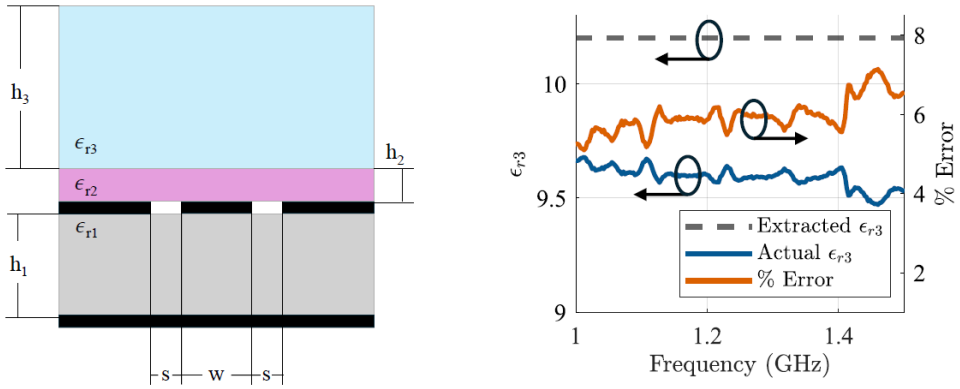


Figure 7.1: (left) Sideview of a GCPW measuring the permittivity of material ϵ_{r3}. ϵ_{r2} is the PET layer and ϵ_{r1} is a known substrate. (right) Extracted permittivity of Rogers 6010. Measurement shows error within 10%

Previous work [68] demonstrates an error margin within 10% for Rogers 6010. By developing more precise methods for measuring permittivity, it becomes possible to validate temperature

measurements for multi-tissue layers and conduct sensitivity analyses using a variety of permittivity variations.

7.2.4 Miniaturization of Hardware

Further miniaturization of the radiometer presents a promising direction for developing highly compact systems suitable for portable or wearable applications. Integrating the radiometer directly behind the NFA would create a highly compact sensor. Components can be mounted on an additional substrate layer added behind the NFA's ground plane.

The smallest NFA developed in this work is a 3.5 cm diameter circular design. An MMIC, including the front-end of a Dicke radiometer, measures just 3m̀m × 1.1m̀m. To further reduce size, the detector, currently implemented on a PCB, can also be integrated into the MMIC.

A critical component for integration is a high-rejection band-pass filter to mitigate outer-band interference. Designing such filters on-chip remains challenging due to the low Q-factor of fabrication processes. Currently, off-the-shelf SAW and cavity filters are used, but cavity filters, while effective, are bulky. Reducing their size while maintaining performance is essential for successful integration into a miniaturized radiometer system.

7.2.5 Interference Mitigation

Enhancing interference mitigation is another critical area of focus. Improved metal shielding can significantly reduce environmental noise and electromagnetic interference, thereby increasing the radiometer's reliability. These improvements can be implemented both in the radiometer's packaging and in the design of the NFA itself.

Advanced interference cancellation techniques, such as adaptive filtering and interference cancellation algorithms, can further enhance the system's robustness in challenging environments. Measurements were conducted in various test settings and locations, and depending on the observed RFI, the radiometer circuitry was placed inside a metal shielding box, as shown in Fig. 7.2.

The current metal box is significantly larger than the radiometer circuitry, but a custom

metal box can be fabricated to fit the circuit precisely while maintaining convenient connections to measurement equipment. Additionally, a 3D-printed platform can be designed to minimize RFI and improve isolation between components on the radiometer, as demonstrated in [69].

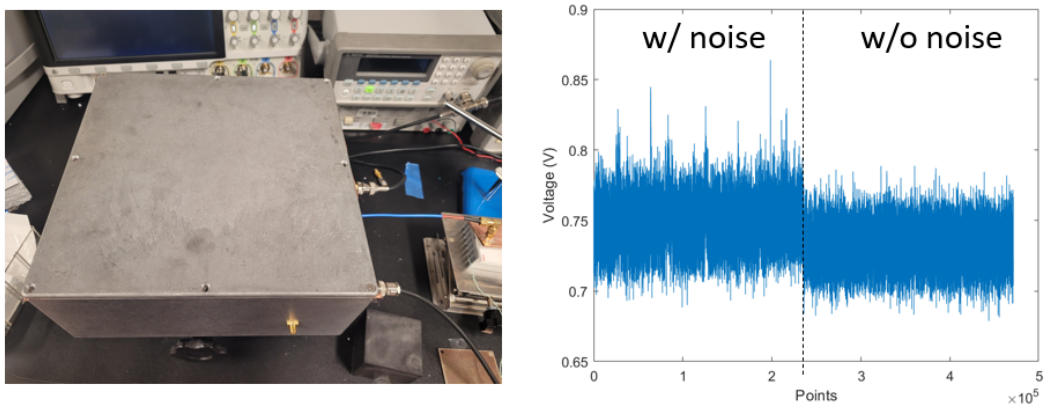


Figure 7.2: A shielded metal box is used to reduce RFI, covering the radiometer circuit to improve measurement accuracy. The right figure shows the time transient of the radiometer's output voltage. When the box is open, RFI introduces instant spikes in the output voltage, leading to temperature measurement errors. With the metal box closed, the spikes are significantly reduced, resulting in more stable output voltage and improved measurement reliability.

However, these metal boxes are heavy and bulky, which conflicts with the goal of creating a wearable device. A simpler and more effective method involves post-processing the output data, as successfully demonstrated in [70]. This approach uses an auxiliary antenna to cancel out interference, isolating the desired thermal noise. Integrating this technique with the radiometer allows stable and accurate measurements across a wide range of conditions by dynamically adjusting to varying noise and interference levels.

7.2.6 Neural Network for Tissue layer Characterization

Integrating machine learning, particularly neural networks, into radiometric sensors offers significant potential for improving temperature estimation, as illustrated in Fig. 7.3. Currently, the thickness and permittivity of tissue layers are generalized and simulated using full EM simulations to derive weighting factors. However, these properties can vary significantly across individuals and across different parts of the body.

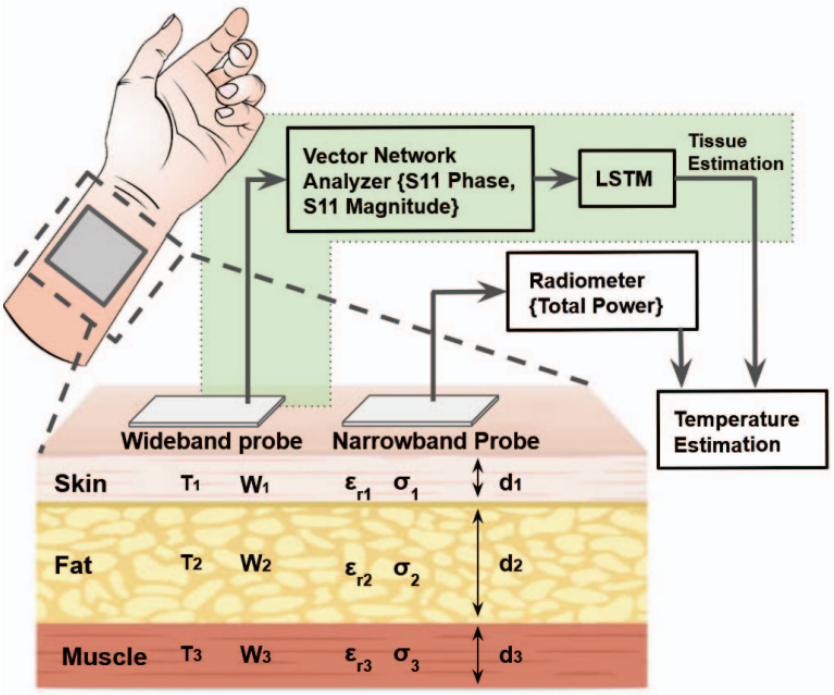


Figure 7.3: Previous work has demonstrated the use of a neural network model to estimate the thickness of tissue layers [9]. Tissue-dependent weighting factors are then applied to estimate the temperatures of individual layers. In this approach, a wideband antenna collects reflectometry data from a VNA operating in the 2 to 13.5 GHz range. The collected data is processed using a long short-term memory (LSTM) algorithm to determine the layer properties.

In the proposed approach, a wideband NFA is placed directly on the tissue layers, and a separate vector network analyzer (VNA) measures the reflection coefficient. This measured coefficient contains valuable information about the thickness and dielectric properties of the tissue layers, as these characteristics directly influence the reflected signal. By training neural networks on these reflection coefficients, the system can learn to estimate the thickness and permittivity of the layers in real-time, dynamically adapting to individual variations. This adaptive capability enables radiometric sensors to deliver personalized and highly accurate temperature measurements.

By addressing these areas, future work can significantly advance radiometric sensing technologies, enabling the development of highly accurate, compact, and robust systems for biomedical applications.

Bibliography

[1] C. Gabriel, "Compilation of the dielectric properties of body tissues at RF and microwave frequencies." King's Coll London (United Kingdom) Dept of Physics, Tech. Rep., 1996.

[2] B. C. Health, "Cardiovascular surgery: Bch," May 2024. [Online]. Available: https://www.bch.org/our-services/cardiology/tests-treatments/cardiovascular-surgery/

[3] U. Health, "Hyperthermia," Oct 2020. [Online]. Available: https://www.ucsfhealth.org/treatments/hyperthermia

[4] L. C. Lack, M. Gradisar, E. J. Van Someren, H. R. Wright, and K. Lushington, "The relationship between insomnia and body temperatures," Sleep Med. Rev., vol. 12, no. 4, pp. 307–317, Aug. 2008.

[5] Maya0851601054, "3D rendering illustration of lymphatic system stock illustration," Jul 2021. [Online]. Available: https://www.dreamstime.com/d-rendering-illustration-lymphatic-system\-orange-lymphatic-system-front-view-image225146687

[6] S. Mizushina, H. Oh-ishi, and Y. Hamamura, "A three-band microwave radiometer for noninvasive temperature measurement," in 1984 IEEE MTT-S Int. Microw. Symp. Dig., May 1984, pp. 145–146.

[7] S. G. Vesnin, M. K. Sedankin, L. M. Ovchinnikov, A. G. Gudkov, V. Y. Leushin, I. A. Sidorov, and I. I. Goryanin, "Portable microwave radiometer for wearable devices," Sens. Actuators A, Phys., vol. 318, p. 112506, Feb. 2021.

[8] I. Kim, W. Jang, H.-S. Hwang, B.-J. Seo, D.-M. Lee, J.-H. Han, J.-W. Shin, Y.-R. Yoon, T. Oh, H.-C. Park et al., "A highly integrated radio frequency receiver rf cmos module for core body temperature thermometer," IEEE Access, 2023.

[9] H. Jethani and Z. Popović, "Neural network model for tissue thickness estimation," in 2024 IEEE First International Conference on Artificial Intelligence for Medicine, Health and Care (AIMHC). IEEE, 2024, pp. 220–227.

[10] F. Biancari, T. Juvonen, and G. Speziale, "Commentary: Cooling the brain for elective aortic hemiarch repair," J. Thoracic Cardiovascular Surg., vol. 165, no. 5, pp. 1774–1775, May 2023.

[11] G. Baronzio, G. Parmar, M. Ballerini, A. Szasz, M. Baronzio, and V. Cassutti, "A brief overview of hyperthermia in cancer treatment," J Integr Oncol, vol. 3, no. 115, p. 2, 2014.

[12] P. Wust, B. Hildebrandt, G. Sreenivasa, B. Rau, J. Gellermann, H. Riess, R. Felix, and P. Schlag, "Hyperthermia in combined treatment of cancer," The lancet oncology, vol. 3, no. 8, pp. 487–497, Aug. 2002.

[13] C. L. Lim, C. Byrne, and J. K. Lee, "Human thermoregulation and measurement of body temperature in exercise and clinical settings," Ann. Acad. Med. Singap., vol. 37, no. 4, pp. 347–353, Apr. 2008.

[14] A. S. Howe and B. P. Boden, "Heat-related illness in athletes," Amer. J. Sports Med., vol. 35, no. 8, pp. 1384–1395, Aug. 2007.

[15] V. M. Ravi, A. K. Sharma, and K. Arunachalam, "Pre-clinical testing of microwave radiometer and a pilot study on the screening inflammation of knee joints," Bioelectromagnetics, vol. 40, no. 6, pp. 402–411, Sep. 2019.

[16] A. Owda, N. Salmon, S. Shylo, and M. Owda, "Assessment of bandaged burn wounds using porcine skin and millimetric radiometry," MDPI Sensors, vol. 19, no. 13, Jul. 2019.

[17] H. Odéen and D. L. Parker, "Magnetic resonance thermometry and its biological applications–physical principles and practical considerations," Progress in nuclear magnetic resonance spectroscopy, vol. 110, pp. 34–61, 2019.

[18] G. Galiana, R. T. Branca, E. R. Jenista, and W. S. Warren, "Accurate temperature imaging based on intermolecular coherences in magnetic resonance," Science, vol. 322, no. 5900, pp. 421–424, 2008.

[19] L. Teunissen, J. Klewer, A. De Haan, J. De Koning, and H. Daanen, "Non-invasive continuous core temperature measurement by zero heat flux," Physiological measurement, vol. 32, no. 5, p. 559, 2011.

[20] S. Mendt, M. A. Maggioni, M. Nordine, M. Steinach, O. Opatz, D. Belavý, D. Felsenberg, J. Koch, P. Shang, H.-C. Gunga, and A. Stahn, "Circadian rhythms in bed rest: Monitoring core body temperature via heat-flux approach is superior to skin surface temperature," Chronobiol. Int., vol. 34, no. 5, pp. 666–676, May 2017. [Online]. Available: https://doi.org/10.1080/07420528.2016.1224241

[21] CORE, "the core sensor technology," Accessed: Jul. 1, 2023. [Online]. Available: https://corebodytemp.com/pages/the-core-body-temperature-sensor-technology

[22] S. Mizushina, M. Matsuda, K. Matsui, Y. Hamamura, and T. Sugiura, "Non-invasive temperature profiling using multi-frequency microwave radiometry in the presence of water-filled bolus," IEICE Trans. on Electronics, vol. 74, no. 5, pp. 1293–1302, 1991.

[23] P. Momenroodaki, W. Haines, M. Fromandi, and Z. Popovic, "Noninvasive internal body temperature tracking with near-field microwave radiometry," IEEE Trans. Microw. Theory Techn., vol. 66, no. 5, pp. 2535–2545, Dec. 2017.

[24] V. Levshinskii, C. Galazis, L. Ovchinnikov, S. Vesnin, A. Losev, and I. Goryanin, "Application of data mining and machine learning in microwave radiometry (mwr)," in Int. Joint Conf. on Biomedical Engineering Systems and Technologies. Springer, 2019, pp. 265–288.

[25] O. Shevelev, M. Petrova, A. Smolensky, B. Osmonov, S. Toimatov, T. Kharybina, S. Karbainov, L. Ovchinnikov, S. Vesnin, A. Tarakanov et al., "Using medical microwave radiometry for brain temperature measurements," Drug discovery today, 2021.

[26] B. Oliver, "Thermal and quantum noise," Proceedings of the IEEE, vol. 53, no. 5, pp. 436–454, 1965.

[27] B. Enander and G. Larson, "Microwave radiometric measurements of the temperature inside a body," Electron. Lett., vol. 15, no. 10, p. 317, 1974.

[28] J. Edrich and P. Hardee, "Thermography at millimeter wavelengths," Proc. IEEE, vol. 62, no. 10, pp. 1391–1392, Oct. 1974.

[29] R. Streeter, G. S. Botello, K. Hall, and Z. Popović, "Correlation radiometry for subcutaneous temperature measurements," IEEE J. Electromagn., RF Microw. Med. Biol., vol. 6, no. 2, pp. 230–237, Nov. 2021.

[30] D. B. Rodrigues, P. R. Stauffer, P. J. Pereira, and P. F. Maccarini, "Microwave radiometry for noninvasive monitoring of brain temperature," in Emerging electromagnetic technologies for brain diseases diagnostics, monitoring and therapy. Springer, 2018, pp. 87–127.

[31] Q. Bonds, J. Gerig, T. M. Weller, and P. Herzig, "Towards core body temperature measurement via close proximity radiometric sensing," IEEE Sensors Journal, vol. 12, no. 3, pp. 519–526, 2011.

[32] I. Kim, D.-M. Lee, Y.-J. Lee, J.-W. Shin, E.-S. Kim, H. Lee, and N.-Y. Kim, "Dual-band on-body near field antenna for measuring deep core temperature with a microwave radiometer," IEEE Access, vol. 10, pp. 63 715–63 722, Jun. 2022.

[33] K. L. Hall, R. Streeter, and Z. Popović, "Near-field antenna for noninvasive human head microwave thermometry," in 2022 IEEE International Symposium on Antennas and Propagation and USNC-URSI Radio Science Meeting (AP-S/URSI). IEEE, 2022, pp. 880–881.

[34] R. P. Scheeler, "A microwave radiometer for internal body temperature measurement," Ph.D. dissertation, University of Colorado at Boulder, 2013.

[35] D. B. Rodrigues, P. F. Maccarini, S. Salahi, T. R. Oliveira, P. J. Pereira, P. Limao-Vieira, B. W. Snow, D. Reudink, and P. R. Stauffer, "Design and optimization of an ultra wideband and compact microwave antenna for radiometric monitoring of brain temperature," IEEE transactions on biomedical engineering, vol. 61, no. 7, pp. 2154–2160, 2014.

[36] P. Momenroodaki, "Radiometric thermometry for wearable deep tissue monitoring," Ph.D. dissertation, University of Colorado at Boulder, 2017.

[37] Spaeg, "Customized generic phantoms," Accessed: Dec. 1, 2022. [Online]. Available: https://speag.swiss/components/phantoms/customized-2/customized-generic-phantoms-2/

[38] D. Andreuccetti, "An internet resource for the calculation of the dielectric properties of body tissues in the frequency range 10 Hz-100 GHz," http://niremf. ifac. cnr. it/tissprop/, 2012.

[39] [Online]. Available: https://www.rogerscorp.com/advanced-electronics-solutions/rt-duroid-laminates/rt-duroid-6006-and-6010-2lm-laminates

[40] H. Zhang, "Electrical properties of foods," Food engineering, vol. 1, pp. 110–119, 2009.

[41] Z. Popovic, P. Momenroodaki, and R. Scheeler, "Toward wearable wireless thermometers for internal body temperature measurements," IEEE Communications Magazine, vol. 52, no. 10, pp. 118–125, 2014.

[42] J. Lee, G. S. Botello, R. Streeter, and Z. Popović, "Noninvasive internal body thermometry with on-chip GaAs Dicke radiometer," IEEE Microw. Wireless Technol. Lett., vol. 33, no. 6, pp. 927–930, Apr. 2023.

[43] J. Lee, G. S. Botello, R. Streeter, and Z. Popović, "A 1.4-GHz GaAs MMIC radiometer for non-invasive internal body thermometry," IEEE Transactions on Microwave Theory and Techniques, 2023.

[44] J. Lee, S. Mvokany, and Z. Popovic, "On-chip radiometer with miniaturized near-field antenna for internal body thermometry," in 2024 IEEE MTT-S International Microwave Biomedical Conference (IMBioC). IEEE, 2024, pp. 140–142.

[45] F. T. Ulaby, D. G. Long, W. J. Blackwell, C. Elachi, A. K. Fung, C. Ruf, K. Sarabandi, H. A. Zebker, and J. Van Zyl, Microwave radar and radiometric remote sensing. University of Michigan Press Ann Arbor, MI, USA, 2014, vol. 4, no. 5.

[46] E. Villa, N. Arteaga-Marrero, G. León, L. Herrán, I. Mateos, and J. Ruiz-Alzola, "A 3.5-GHz pseudo-correlation type radiometer for biomedical applications," AEU - Int. J. Electron. Commun., vol. 130, p. 153558, 2021. [Online]. Available: https://www.sciencedirect.com/science/article/pii/S143484112032762X

[47] J. Lee, G. S. Botello, R. Streeter, K. Hall, and Z. Popović, "A hybrid correlation-Dicke radiometer for internal body thermometry," in Proc. 52nd Eur. Microw. Conf. (EuMC). IEEE, Sep. 2022, pp. 464–467.

[48] A. Kerr, "On the noise properties of balanced amplifiers," IEEE Microw. Guided Wave Lett., vol. 8, no. 11, pp. 390–392, Nov. 1998.

[49] J. Lee and Z. Popović, "A GaAs LNA MMIC for a correlation-Dicke radiometer internal-body temperature sensor," in Proc. IEEE Radio Wireless Symp. (RWS), Jan. 2023, pp. 31–33.

[50] T.-K. Nguyen, C.-H. Kim, G.-J. Ihm, M.-S. Yang, and S.-G. Lee, "Cmos low-noise amplifier design optimization techniques," IEEE Trans. on Microwave Theory and Techniques, vol. 52, no. 5, pp. 1433–1442, 2004.

[51] S. Wang, "A GaAs MMIC LNA design for wideband satellite communication receiver application," in 2014 IEEE Int. Conf. on Comm. Problem-solving. IEEE, Dec. 2014, pp. 631–633.

[52] A. M. Bassal and A. H. Jarndal, "GaN low noise amplifier design for WiMax applications," in 2016 16th Mediterranean Microw. Symp. (MMS). IEEE, Nov. 2016, pp. 1–4.

[53] C.-F. Chou, Y.-C. Chang, H. Wang, and C.-C. Chiong, "High gain fully on-chip lnas with wideband input matching in 0.15-μm gaas phemt for radio astronomical telescope," in 2015 European Microwave Conference (EuMC). IEEE, 2015, pp. 235–238.

[54] W.-C. Huang, C.-C. Chiong, and H. Wang, "A fully-integrated s-band differential lna in 0.15-um gaas phemt for radio astronomical receiver," in 2018 IEEE Int. Symp. on Radio-Frequency Integration Technology (RFIT). IEEE, 2018, pp. 1–3.

[55] O. Memioglu and A. Gundel, "A high linearity broadband gain block/lna mmic with diode predistortion in gaas phemt technology," in 2018 18th Mediterranean Microwave Symp. (MMS). IEEE, 2018, pp. 120–123.

[56] S. Weinreb and J. Shi, "Low noise amplifier with 7-k noise at 1.4 ghz and 25 c," IEEE Trans. on Microwave Theory and Techniques, vol. 69, no. 4, pp. 2345–2351, 2021.

[57] Mini-Circuits, "Cbp-1400e+ ceramic resonator band pass filter," Accessed: Jun. 1, 2023. [Online]. Available: https://www.minicircuits.com/WebStore/dashboard.html?model=CBP-1400E%2B

[58] TAI-SAW, "Saw filter 1412 mhz smd," Accessed: Jun. 1, 2023. [Online]. Available: https://www.taisaw.com/upload/product/TA2313A%20_Rev.1.0_.pdf

[59] J. Lee and Z. Popović, "A gaas lna mmic for a correlation-dicke radiometer internal-body temperature sensor," in 2023 IEEE Radio and Wireless Symposium (RWS). IEEE, 2023, pp. 31–33.

[60] M. M. Elsbury, P. D. Dresselhaus, N. F. Bergren, C. J. Burroughs, S. P. Benz, and Z. Popovic, "Broadband lumped-element integrated n-way power dividers for voltage standards," IEEE transactions on microwave theory and techniques, vol. 57, no. 8, pp. 2055–2063, 2009.

[61] J. Boparai and M. Popović, "Development and characterization of skin phantoms at microwave frequencies," IEEE Journal of Electromagnetics, RF and Microwaves in Medicine and Biology, vol. 6, no. 3, pp. 296–304, 2022.

[62] J. Garrett and E. Fear, "Stable and flexible materials to mimic the dielectric properties of human soft tissues," IEEE Antennas and Wireless Propagation Letters, vol. 13, pp. 599–602, 2014.

[63] S. Di Meo, G. Matrone, G. Magenes, and M. Pasian, "On the low-cost production of tissue-mimicking skin phantoms up to 40 ghz," IEEE Journal of Electromagnetics, RF and Microwaves in Medicine and Biology, 2024.

[64] K. Tisdale, A. Bringer, and A. Kiourti, "Development of a coherent model for radiometric core body temperature sensing," IEEE J. Electromagn., RF Microw. Med. Biol., vol. 6, no. 3, pp. 355–363, Mar. 2022.

[65] J. E. Hall and M. E. Hall, "ch. 74: Body temperature regulation and fever," in Guyton and Hall Textbook of Medical Physiology, 14th ed, 2021, pp. 901–902.

[66] E. Groumpas, M. Koutsoupidou, I. S. Karanasiou, C. Papageorgiou, and N. Uzunoglu, "Real-time passive brain monitoring system using near-field microwave radiometry," IEEE Transactions on Biomedical Engineering, vol. 67, no. 1, pp. 158–165, 2019.

[67] S. Di Meo, A. Cannatà, C. Blanco-Angulo, G. Matrone, A. Martínez-Lozano, J. Arias-Rodríguez, J. M. Sabater-Navarro, R. Gutiérrez-Mazón, H. García-Martínez, E. Ávila-Navarro et al., "Multi-layer tissue-mimicking breast phantoms for microwave-based imaging systems," IEEE Journal of Electromagnetics, RF and Microwaves in Medicine and Biology, 2024.

[68] A. Ikelheimer, L. Egaas, J. Dunbar, and Z. Popović, "Grounded coplanar waveguides for material characterization," in 2025 United States National Committee of URSI National Radio Science Meeting (USNC-URSI NRSM). IEEE, 2025.

[69] H. Pienaar, J. Andriambeloson, and D. Davidson, "Rf shielding for multi-copter based electromagnetic metrology platforms," in 2016 IEEE Conference on Antenna Measurements & Applications (CAMA). IEEE, 2016, pp. 1–4.

[70] J. Dunbar, G. Santamaría-Botello, and Z. Popović, "Rf interference cancellation for microwave thermometry," in 2024 IEEE/MTT-S International Microwave Symposium - IMS 2024, 2024, pp. 1015–1018.

ProQuest Number: 31940018

INFORMATION TO ALL USERS
The quality and completeness of this reproduction is dependent on the quality
and completeness of the copy made available to ProQuest.



Distributed by
ProQuest LLC a part of Clarivate (2025).
Copyright of the Dissertation is held by the Author unless otherwise noted.

This work is protected against unauthorized copying under Title 17,
United States Code and other applicable copyright laws.

This work may be used in accordance with the terms of the Creative Commons license
or other rights statement, as indicated in the copyright statement or in the metadata
associated with this work. Unless otherwise specified in the copyright statement
or the metadata, all rights are reserved by the copyright holder.

ProQuest LLC
789 East Eisenhower Parkway
Ann Arbor, MI 48108 USA